Electronic Supplementary Material (ESI) for Journal of Materials Chemistry A.

Electronic Supplementary Information

A Highly Emissive Fluorescent Zn-MOF: Molecular Decoding Strategies for Solvents and Trace Detection of Dunnite in Water

*Prasenjit Das and Sanjay K Mandal**

Department of Chemical Sciences, Indian Institute of Science Education and Research Mohali, Sector 81, Manauli PO, S.A.S. Nagar, Mohali, Punjab 140306, India

Corresponding Author

*E-mail: sanjaymandal@iisermohali.ac.in

Contents

Section S-1: General Information

Experimental section

Caution! Dunnite and TNT, TNP are highly explosive and should be carefully handled. The explosives were handled as dilute solutions and with safety measures to avoid explosion.

Materials. All chemicals and solvents used for synthesis of MOF, and sensing experiment were obtained from commercial sources and were used as received, without further purification.

Physical measurements

FTIR spectra were measured on a Perkin-Elmer Spectrum I spectrometer with samples prepared as KBr pellets in the 4000-400 cm^{-1} range.

Melting points were determined by a Büchi M-565 instrument with the heating rate of 10 ^{o}C per minute.

High resolution mass spectrometry (HRMS) data were measured by Thermo Scientific LTQ XL LC-MS instrument for the 50-2000 amu range with ESI ion source. Atmospheric Pressure Chemical Ionization (APCI) has been used for solid state mass spectrometry.

The **^{1}H and ^{13}C NMR** spectra of the ligands were obtained in sodium salt of D_2O solution at 25 ◦C on a Bruker ARX-400 spectrometer.

Elemental analysis (C, H, N) was carried out using a Leco TruSpec Micro analyzer.

Thermogravimetric analysis was carried out from 25 to 600 ◦C (at a heating rate of 10 ◦C/min) under dinitrogen atmosphere on a Shimadzu DTG-60H instrument.

UV-Vis-NIR and **Solid state reflectance** spectra were recorded using Cary 5000 by Agilent Technology.

Single crystal X-ray data collection and refinements. Crystals of the compound were transferred from mother liquor to mineral oil for manipulation, selection and mounting. One appropriate block shaped crystal was selected by monitoring under an optical microscope and then put inside the nylon loop attached to a goniometer head. It was then

placed under a cold stream of nitrogen gas for slow cooling to 100 K temperature. Bruker Kappa APEX II diffractometer equipped with a CCD detector (with the crystal-to-detector distance fixed at 60 mm) and sealed-tube monochromated MoKα radiation was used to perform initial crystal evaluation and data collection. The diffractometer was interfaced to a PC with APEX2[S1] program installed in it that controlled the crystal centering, unit cell determination, refinement of the cell parameters and data collection. The program SAINT[1] was used for data integration, fitting of reflection profiles, and values of F^2 and $\sigma(F^2)$ for each reflection were obtained. Data were also corrected for Lorentz and polarization effects. The subroutine XPREP[S1] was used for the processing of data that included determination of space group, application of an absorption correction (SADABS),[S1] merging of data and generation of files necessary for solution and refinement. The crystal structures were solved and refined by using SHELXL 2014.[S2] Several full-matrix least-squares/difference Fourier cycles were performed, locating the remainder of the non-hydrogen atoms and to have reasonable thermal parameters and converged refinement resulting in the lowest residual factors and optimum goodness of fit. The crystallographic figures were drawn using Mercury V 3.0, Diamond V 3.2, ViewerLite and TOPOS Pro softwares.

(S1) APEX2, SADABS, and SAINT; Bruker AXS inc: Madison, WI, USA, 2008.

(S2) G. M. Sheldrick, *SHELXTL* Version 2014/7. *https://shelx.uniac.gwdg.de/SHELX/index.php.*

Crystal data for **1** (formula/MW: $C_{26}H_{29}N_7O_{13}Zn_2$/MW 778.33) that were collected with the use of a Bruker Kappa APEX II diffractometer equipped with a CCD detector and sealed-tube monochromated MoKα radiation (λ = 0.071073 Å) are as follows at 100 K: monoclinic, space group $P2_1/c$ (No. 14), a = 14.7622(12) Å, b = 14.6228(12) Å, c = 14.8907(13) Å, α = 90°, β = 103.074 (5)°, γ = 90° , V = 3131.1(5) Å^3, Z = 4, D_c = 1.65 mg/cm^3, μ = 1.609 mm^{-1}, 23697 reflections collected. Refinement of 5586 reflections (414 parameters) with $I > 2\sigma(I)$ converged at a final R_1 = 0.0746, wR_2 = 0.2208, GOF = 1.011. Crystallographic data for **1** has been deposited with the Cambridge Crystallographic Data Centre as supplementary material (CCDC 1860161).

Power X-ray diffraction (PXRD) measurements were recorded on a Rigaku Ultima IV diffractometer equipped with a 3 KW sealed tube Cu Kα X-ray radiation (generator power settings: 40 kV and 40 mA) and a DTex Ultra detector using Bragg-Brentano geometry (2.5° primary and secondary solar slits, 0.5° divergence slit with 10 mm height limit slit) over an angle range 5° to 50° with a scanning speed of 1° per minute with 0.02° step with XRF reduction for the metals.

Sorption studies. Data were recorded on a BELSORP MAX instrument for pressures in the range 0–1.2 bar by the volumetric method. Each solid sample was transferred to a pre-weighed analysis tube, which was capped with transeals and evacuated by heating at 120 °C (based on the thermal profile obtained from TGA) under dynamic vacuum until an outgas rate of less than 2 mTorr min^{-1} (0.27 Pa min^{-1}) was achieved (12–24 h). The evacuated analysis tube containing the degassed samples was then carefully transferred to an electronic balance and weighed again to determine the mass of sample. The tube was then placed back on the analysis port of the gas adsorption instrument. The outgas rate was again confirmed to be less than 2 mTorr min^{-1} (0.27 Pa min^{-1}). For all isotherms, warm and cold free-space (dead volume) correction measurements were performed using ultra-high-purity He gas (UHP grade 5.0, 99.999% purity). The change of the pressure was monitored and the degree of adsorption was determined by the decrease in pressure at the equilibrium state via computer controlled automatic operations that were set up at the start of each measurement. Oil-free vacuum pumps and oil-free pressure regulators were used for all measurements to prevent contamination of the samples during the evacuation process or of the feed gases during the isotherm measurements.

Field emission scanning electron microscopy (FESEM) was utilized to record surface morphology on JEOL instrument; samples were well dispersed in MeOH, drop casted in a silicon wafer, dried and coated with gold using a working distance of 4.5 to 15 mm and voltage 10 to 15 kV.

High resolution transmission electron microscopy (HRTEM) was performed on FEI Tecnai G2 F20 equipped with a field emission gun operated at 200 Kv with 1 mg sample well dispersed in ethanol (10 mL) using a sonicator for 20 minutes and then put on the copper grid, which was allowed to dry using a lamp for 30 minutes.

Fluorescence microscopy experiment performed using Zeiss AXIO series, Scope.A1 with an optimos camera and excited the compound in DAPI (λ_{exc}: 405 nm), FITC (λ_{exc}: 510 nm) and rhodamine B (λ_{exc}: 570 nm) region.

Confocal microscopy experiment performed using OLYMPUS inspector series and excited the compound in DAPI (λ_{exc}: 405 nm), FITC (λ_{exc}: 510 nm) and rhodamine B (λ_{exc}: 570 nm) region.

Photoluminescence experiments were performed using Horiba Scientific Fluorolog Spectrofluorometer 3.

Optical imaging were performed using benchtop 3UV trans-illuminator upon excitation from 254-365 nm.

DFT calculations were carried out with Gaussian 09 suite of packages.[S3] The structure was optimized by hybrid functional, Becke's three parameter exchange and the Lee−Yang−Parr Correlation Functional (B3LYP) at a split valance basis set 6-31G (d,p).

(S3) M. J. Frisch, G. W. Trucks, H. B. Schlegel, G. E. Scuseria, M. A. Robb, J. R. Cheeseman, G. Scalmani, V. Barone, B. Mennucci, G. A. Petersson, H. Nakatsuji, M. Caricato, X. Li, H. P. Hratchian, A. F. Izmaylov, J. Bloino, G. Zheng, J. L. Sonnenberg, M. Hada, M. Ehara, K. Toyota, R. Fukuda, J. Hasegawa, M. Ishida, T. Nakajima, Y. Honda, O. Kitao, H. Nakai, T. Vreven, J. A., Jr. Montgomery, J. E. Peralta, F. Ogliaro, M. Bearpark, J. J. Heyd, E. Brothers, K. N. Kudin, V. N. Staroverov, T. Keith, R. Kobayashi, J. Normand, K. Raghavachari, A. Rendell, J. C. Burant, S. S. Iyengar, J. Tomasi, M. Cossi, N. Rega, J. M. Millam, M. Klene, J. E. Knox, J. B. Cross, V. Bakken, C. Adamo, J. Jaramillo, R. Gomperts, R. E. Stratmann, O. Yazyev, A. J. Austin, R. Cammi, C. Pomelli, J. W. Ochterski, R. L. Martin, K. Morokuma, V. G. Zakrzewski, G. A. Voth, P. Salvador, J. J. Dannenberg, S. Dapprich, A. D. Daniels, O. Farkas, J. B. Foresman, J. V. Ortiz, J. Cioslowski, D. J. Fox, Gaussian 09; Gaussian, Inc: Wallingford, CT, 2013.

Section 2: Synthesis of H_4MTAIA and Zn-MOF (1)

Synthesis of 2,4-dichloro-6-methoxy-1,3,5-triazine (A): It was prepared following the literature procedure.[S4] In a 5 mL round bottom flask, 1 mL of methanol were taken and cooled to 0 ^oC in an ice bath. 45 mg of $NaHCO_3$ (0.54 mmol) was added portion wise with stirring. Then, 100 mg of cyanuric chloride (0.54 mmol) was added with stirring at 0 ^oC for 10 min. The reaction mixture was further stirred at room temperature for 20 min (till the evolution of the gas stopped). After adding water to the resulting mixture, it was filtered, washed with water and air dried to obtain a white solid product. Recrystallization of the solid in CH_2Cl_2/petroleum ether provided 78 mg of pure **A** (80%) as white solid: M. P.: 85 - 87 °C (lit: 86 - 87 ^oC). Selected FTIR peaks (KBr pellet, cm^{-1}): 1546(s), 1509(vs), 1486(vs), 1390(s), 1305(s), 1262(s), 1167(s), 1054(s), 977(m), 847(s), 807(s), 541(m).

(S4) T. Tanaka, M. Noguchi, Z. Watanabe, T. Misawa, M. Ishihara, A. Kobayashi, S. Shoda, *Org. Biomol. Chem.*, 2010, **8**, 5126–5132.

Synthesis of 5, 5'-((6-methoxy-1,3,5-triazine-2,4-diyl)bis(azanediyl))diisophthalic acid (H_4MTAIA): In a 10 mL RBF, 5-aminoisophthalic acid (125 mg, 0.69 mmol), NaOH (45 mg, 1.1 mmol) and $NaHCO_3$ (65 mg, 0.77 mmol) were dissolved in 2 mL H_2O. The mixture was further stirred at room temperature for 30 min, followed by dropwise addition of 60 mg **A** (0.33 mmol) in 1,4-dioxane (2 mL) using dropping funnel over a period of 10 min. The resulting mixture was then heated at 70 ^oC for 12 h. Upon adjusting the pH of the reaction mixture between 2 and 3 using dilute HCl, an off white solid obtained was filtered, washed several times with distilled water, and dried to give 136 mg of H_4MTAIA (yield: 84%). It was not soluble in common organic and inorganic solvents. M.P. 320 -324 ^oC. HRMS (ESI) m/z: calculated for $[M+H]^+$, 470.0903, found 470.0890. Since it was not soluble in common organic and inorganic solvents, its sodium salt (prepared with 4 eqv. NaOH) was used for NMR experiments in D_2O. ^1H NMR (D_2O, 400 MHz): δ 3.04 (s, 3H), 7.92 (s, 2H), 8.08 (s, 4H) ppm. ^{13}C NMR 400 MHz (D_2O): δ 54.76, 123.96, 124.54, 137, 137.96, 171.13, 174.58 ppm. Selected FTIR peaks (KBr pellet, cm^{-1}) : 3452(br), 3298(s), 3113(m), 1704(s), 1628(s), 1580(vs), 1524(s), 1490(m), 1462(m), 1385(S), 1291(m), 1247(m), 903(w), 798(w), 759(w), 676(w), 622(w). λ_{max} (solid state, reflectance): 227 and 274 nm.

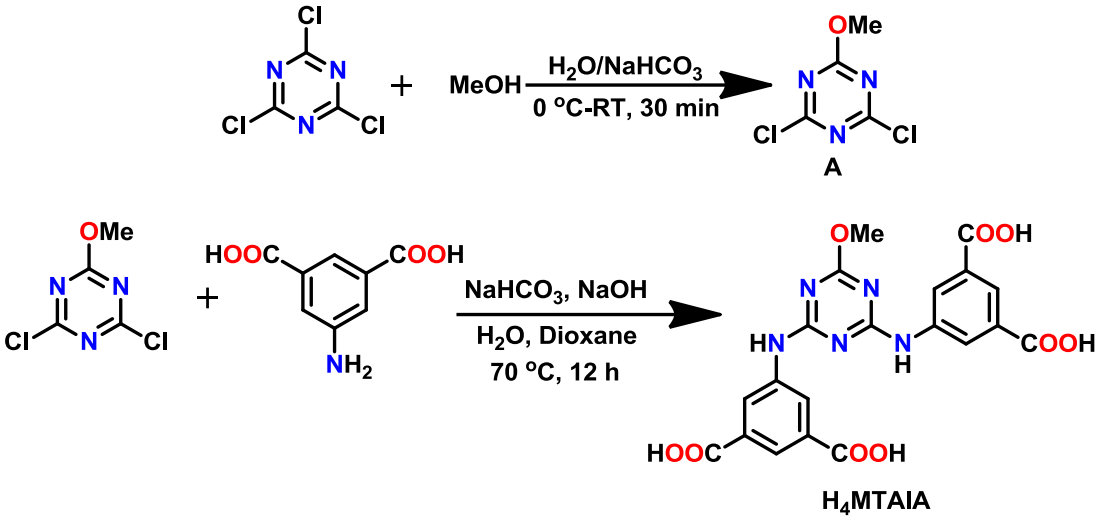

Scheme 1 Synthesis of H_4MTAIA ligand.

Synthesis of {[Zn_2(MTAIA)(DMF)$_2$(H_2O)]·H_2O}$_n$ (1). A mixture of H_4MTAIA (100 mg, 0.213 mmol) and $Zn(OAc)_2 \cdot 2H_2O$ (128 mg, 0.213 mmol) in 3 mL DMF/H_2O (1 : 0.5) were sealed in a 10 mL Teflon lined stainless steel vessel and heated under autogenous pressure at 120 °C for 48 h and then was cooled to room temperature in 24 h. The colourless crystals were filtered, washed with DMF-H_2O which were suitable for SCXRD. The compound was insoluble in water and common organic solvents such as MeOH, MeCN, toluene, DMF and DMSO. Yield: 90 mg (76%). Selected FTIR peaks (KBr pellet, cm^{-1}): 3352(m), 3132(m), 3094(m), 2964(m), 2860(m), 1662(m), 1627(s), 1593(s), 1577(vs), 1569(s), 1529(s), 1501(s), 1474(m), 1447(m), 1373(vs), 1363(vs), 1194(w), 1151(w), 1105(w), 893(w), 802(m), 777(m), 724(m), 643(w), 466(w). Anal. Calcd for $C_{26}H_{29}N_7Zn_2O_{13}$ (MW 775.0406): C, 40.12; H, 3.76; N, 12.60. Found: C, 39.73; H, 4.003; N, 12.06. λ_{max} (solid state, reflectance): 242 and 328 nm. The TGA curve of compound **1** shows a weight loss of 14.15% (calc. 14.02%) in the 34-220 °C range, attributed to the loss of one H_2O (lattice), one H_2O and DMF (coordinated) molecules, 9.35% (calc. 9.32%) in the 221-360 °C range attributed to the loss of one DMF (coordinated) molecules, then the decomposition of compound started.

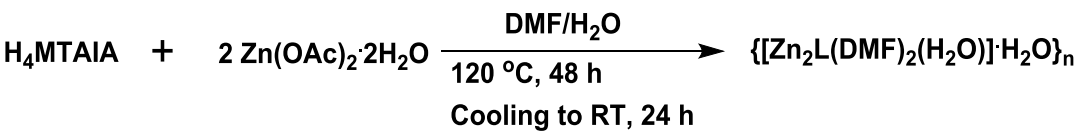

Scheme 2 Synthesis of **1**.

Section 3: Characterization of H_4MTAIA

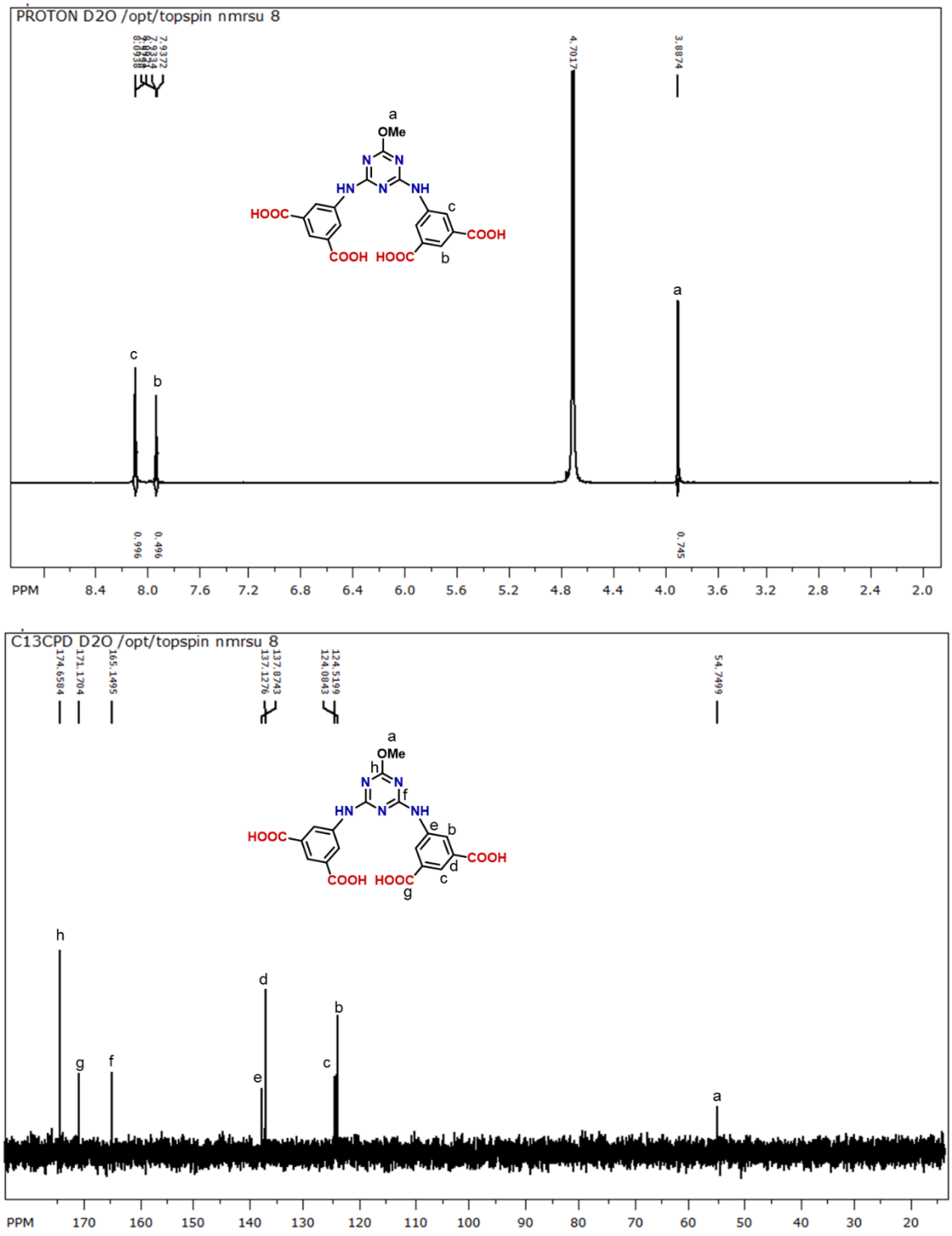

Fig. S1 ^{1}H (top) and ^{13}C NMR (bottom) spectra of H_4MTAIA (sodium salt) in D_2O.

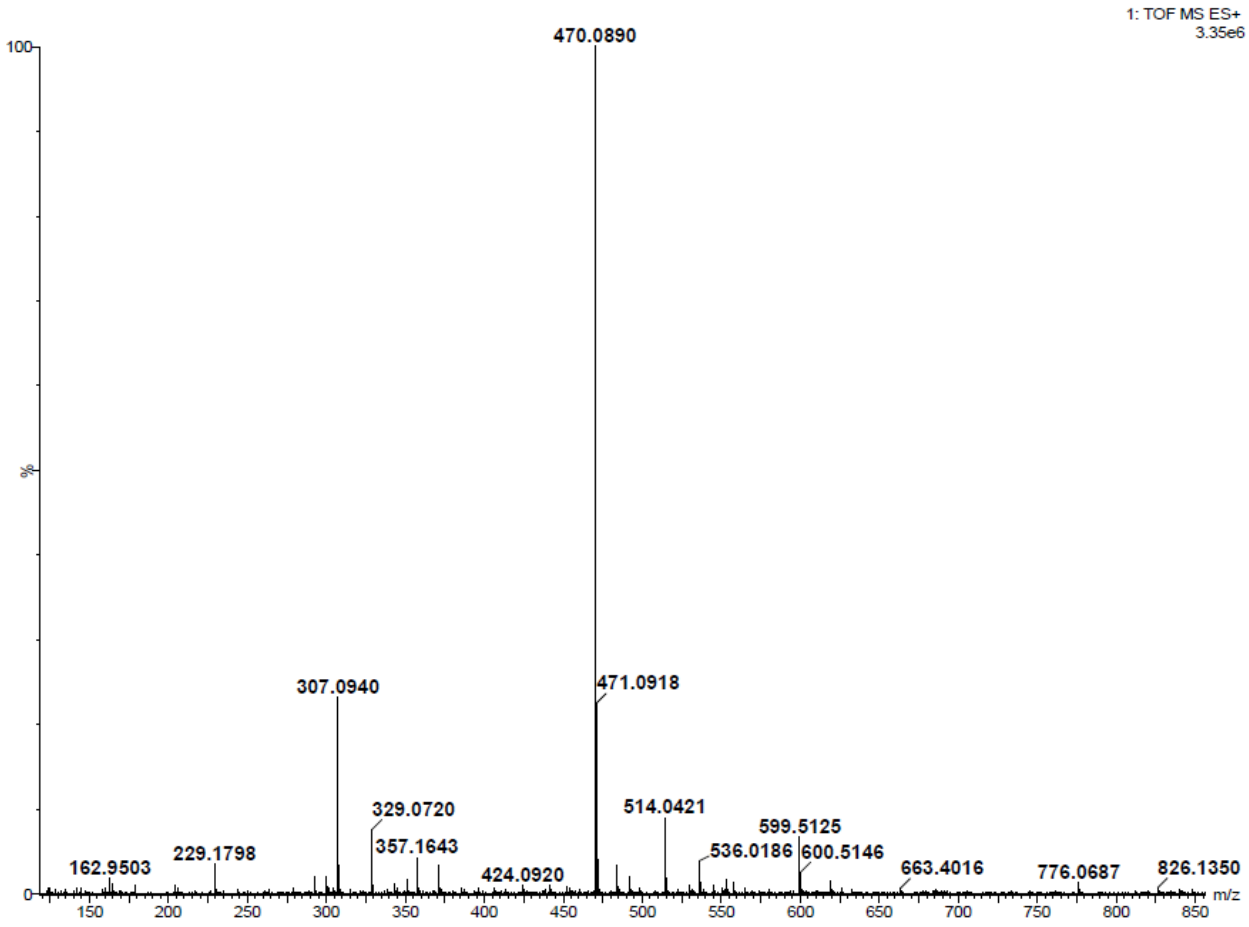

Fig. S2 HRMS spectrum of H_4MTAIA (ESI mode).

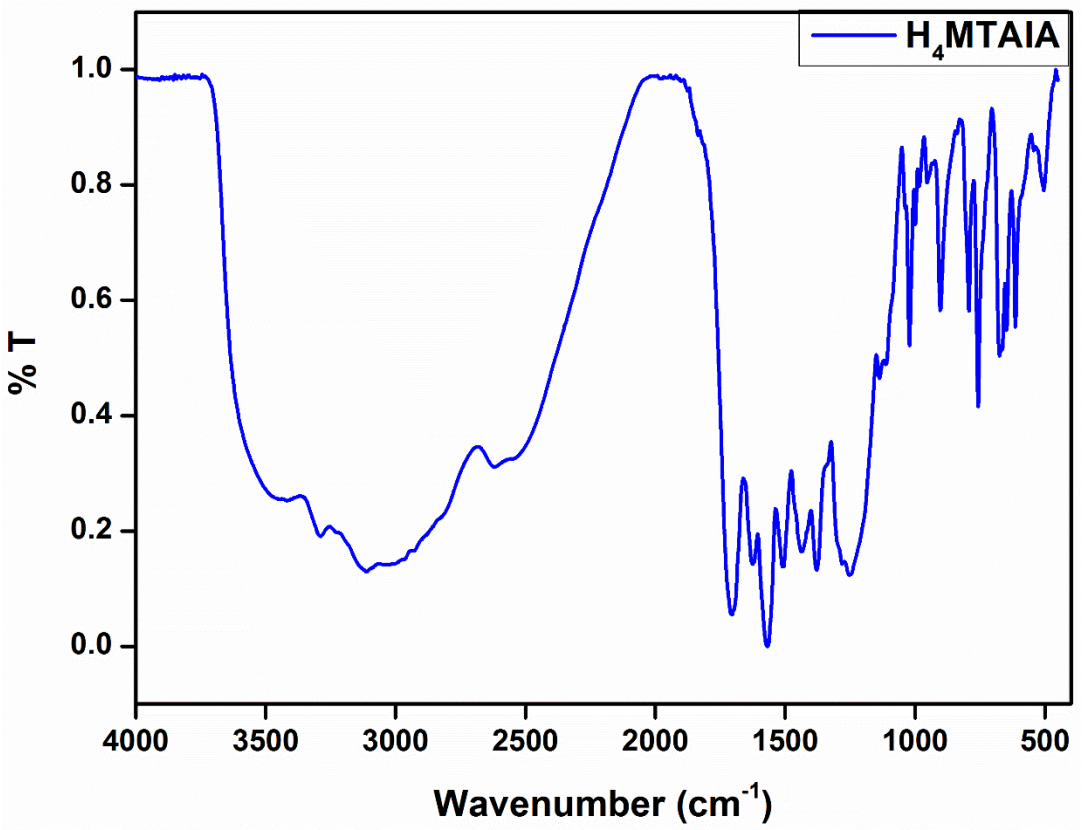

Fig. S3 FTIR spectrum of H_4MTAIA.

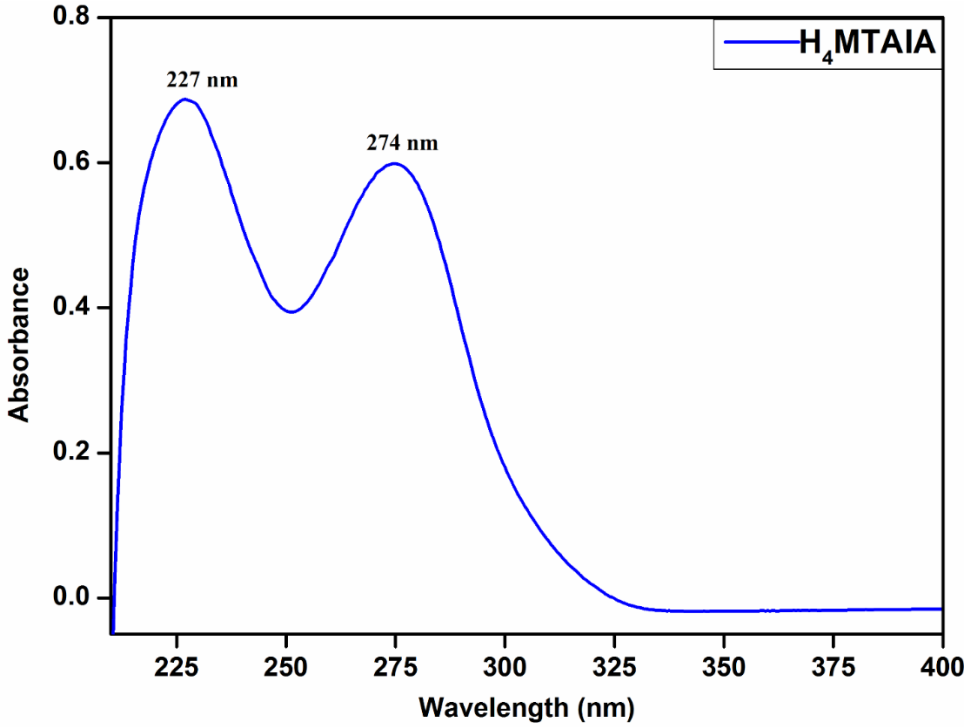

Fig. S4 UV-Vis spectra of H_4MTAIA.

Section 4: Characterization of Zn-MOF (1)

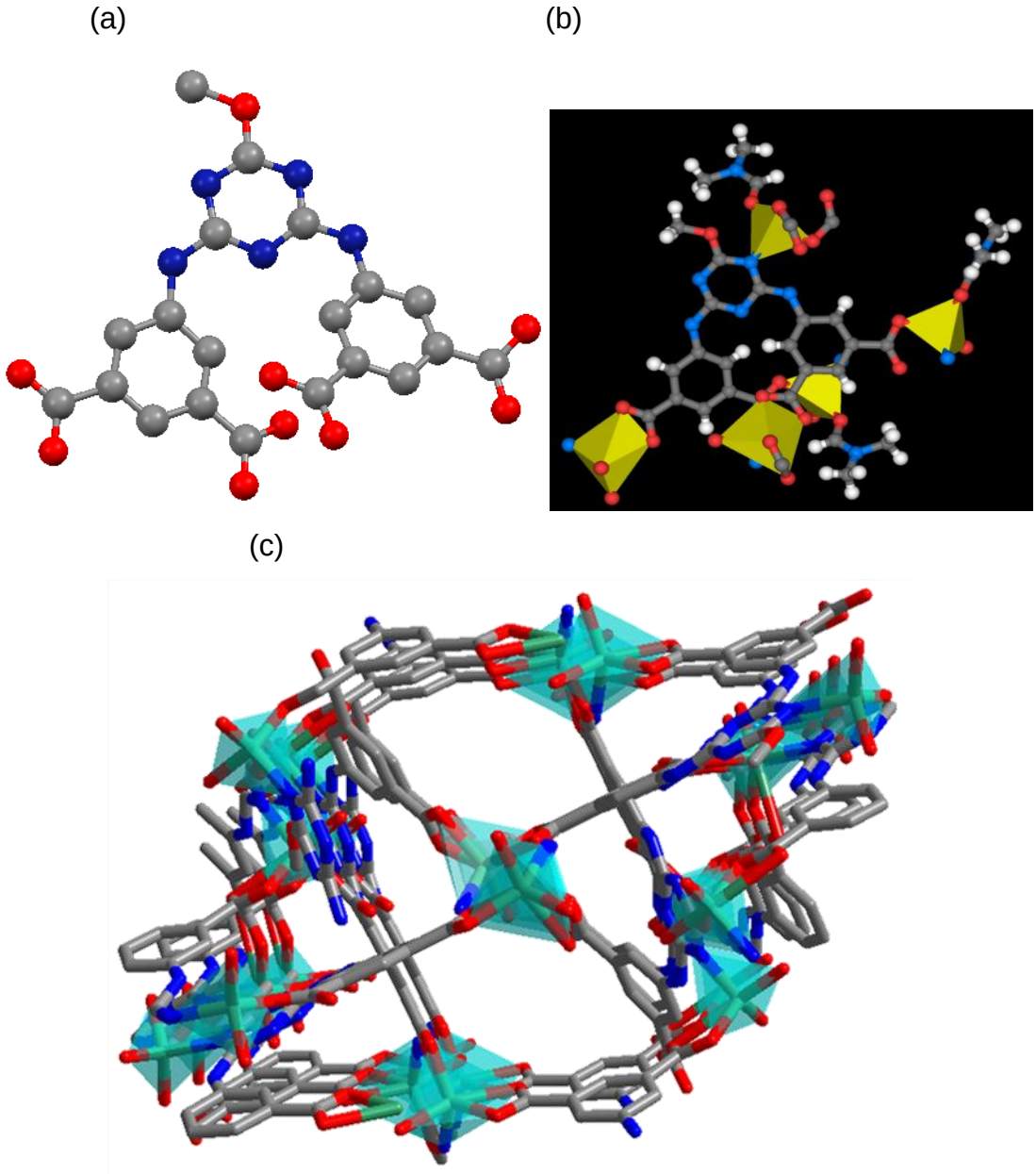

Fig. S5 (a) Syn-configuration of ligand in **Zn-MOF**. (b) Schematic representation showing coordination environment around Zn(II) centers in **Zn-MOF**. (c) Perspective view of **Zn-MOF** viewed down *b*-axis (free guests and hydrogen have been omitted for clarity) (Color code; carbon: grey, oxygen: red, nitrogen: blue, Zinc: green).

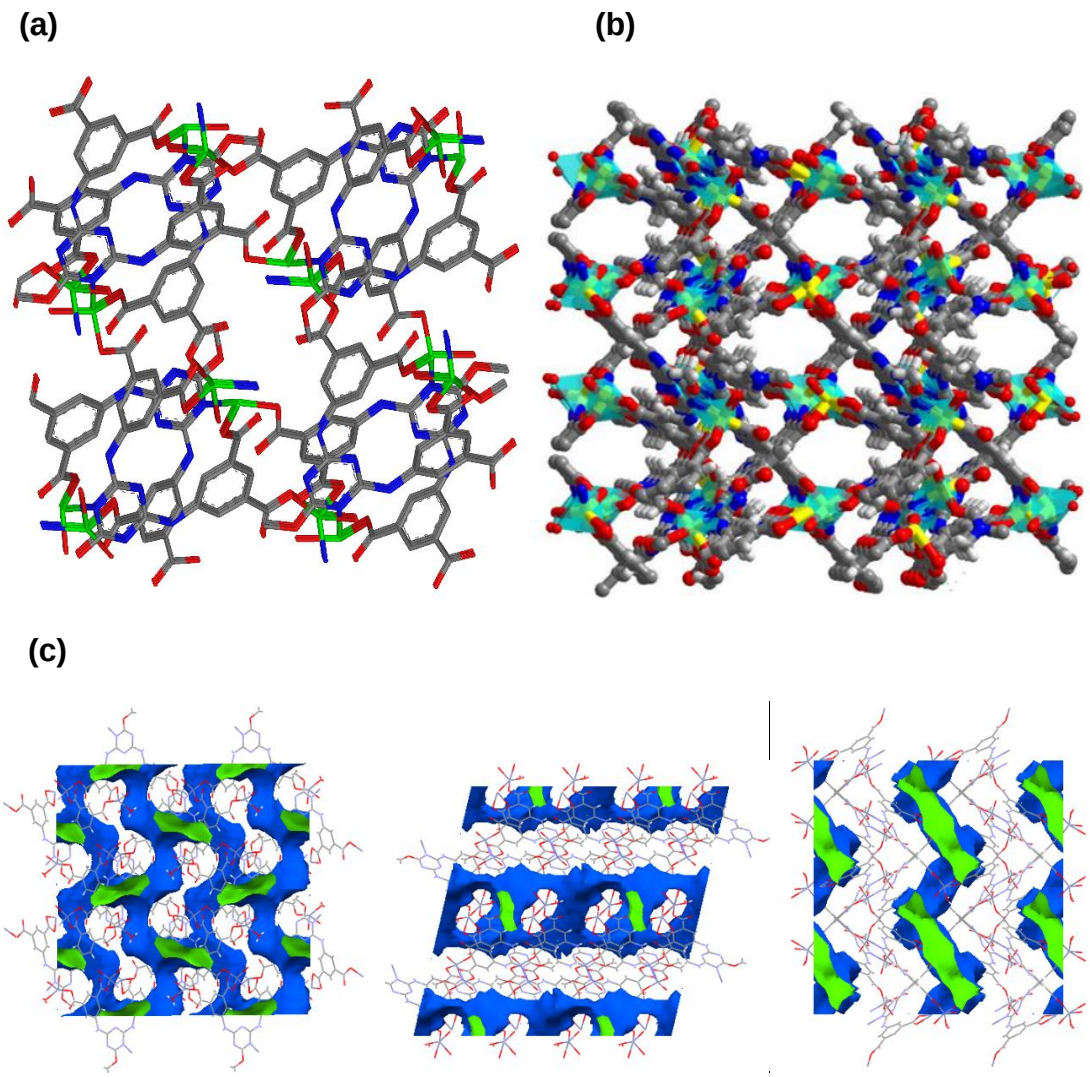

Fig. S6 (a) Perspective view of packing in **Zn-MOF** along a-axis (free guests and hydrogen have been omitted for clarity). (b) Perspective view of packing in **Zn-MOF** along c-axis (free guests have been omitted for clarity). (Color code; carbon: grey, oxygen: red, nitrogen: blue, Zinc: green). (c) Solvent accessible void space along *a*, *b*, *c*-axis (blue: outer site of the pore and green: inner site of the pore) of **Zn-MOF**, respectively.

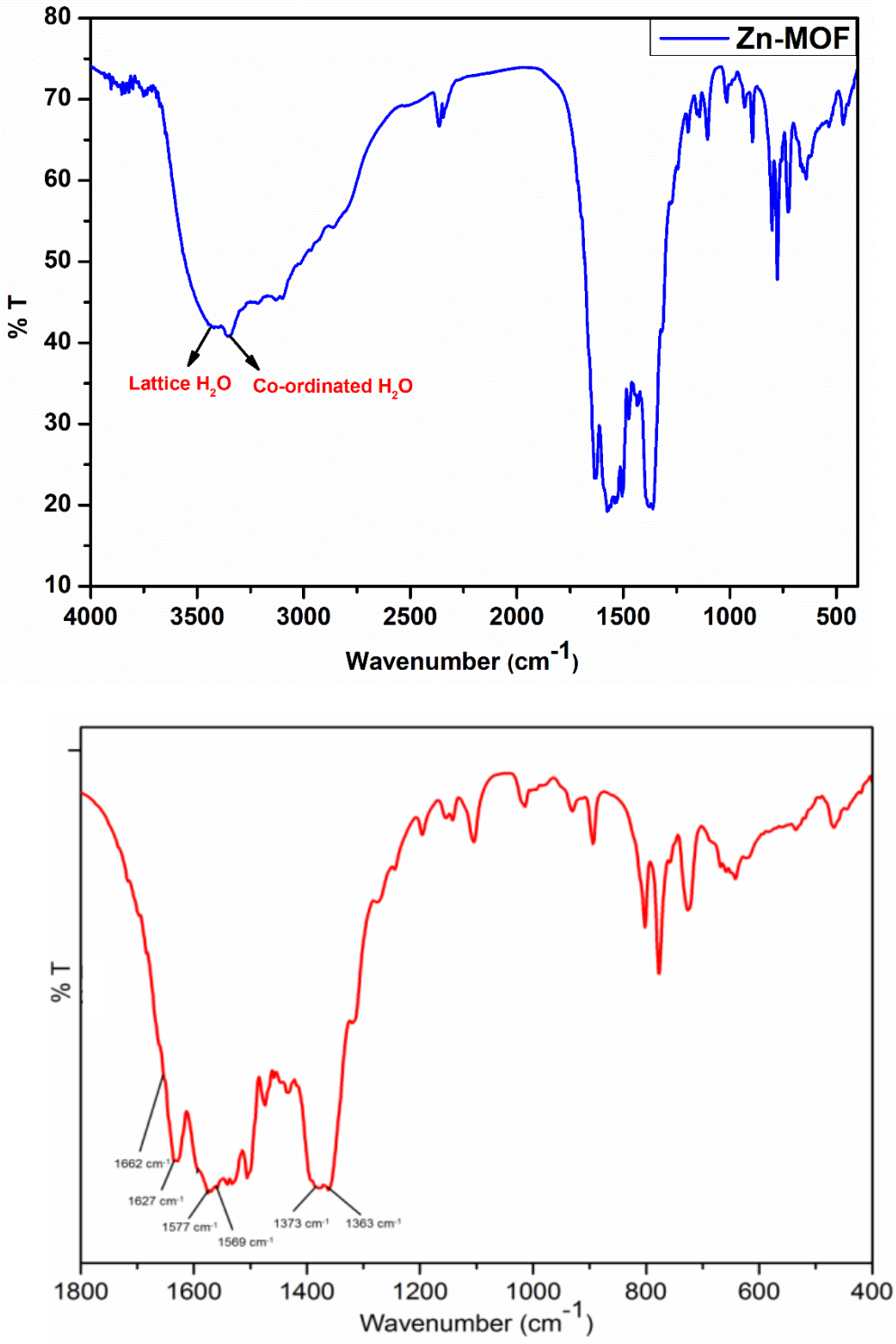

Fig. S7 FTIR spectrum of **Zn-MOF**.

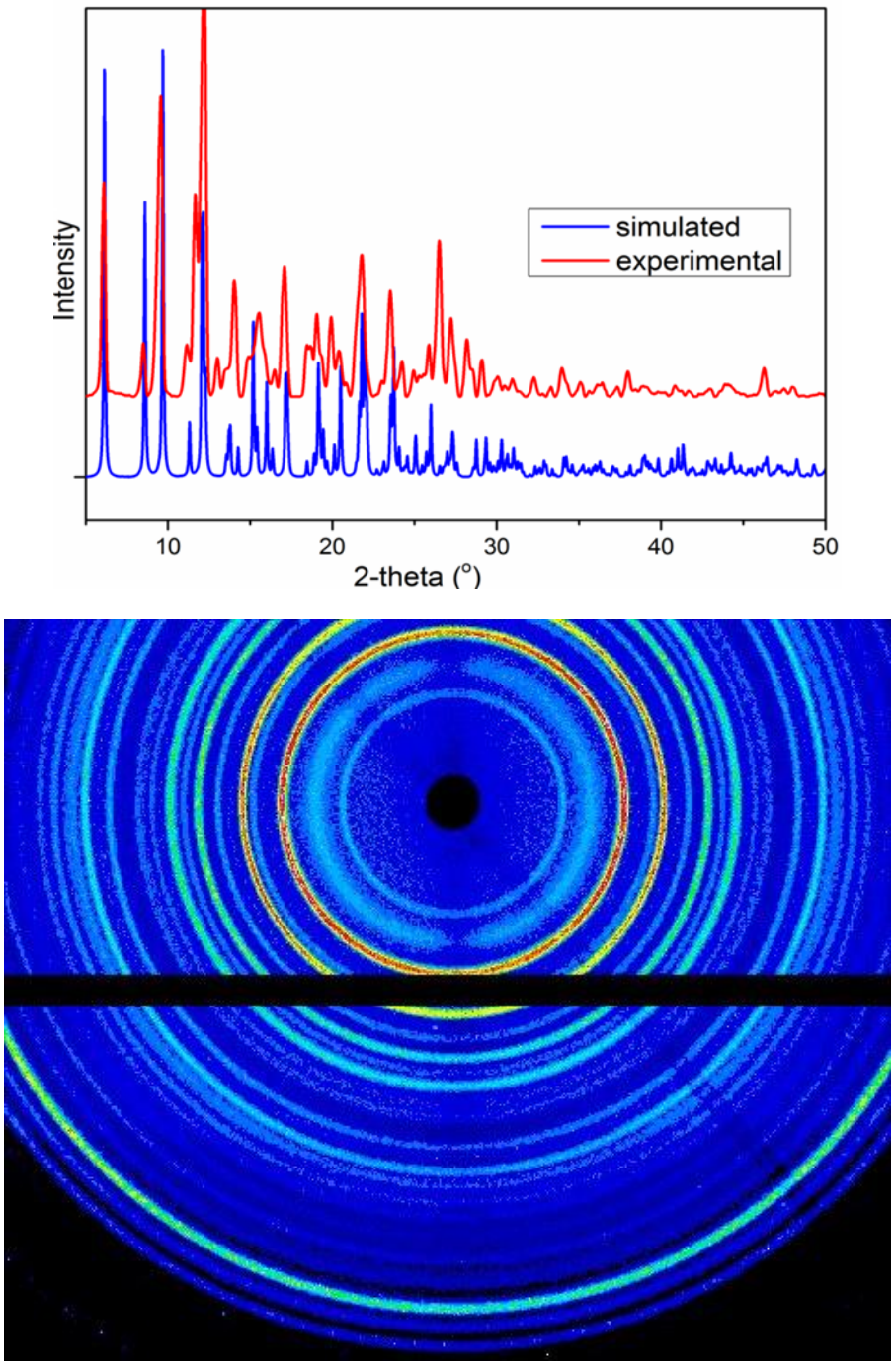

Fig. S8 (Top) PXRD patterns of **Zn-MOF**; (bottom) 2D WAX map.

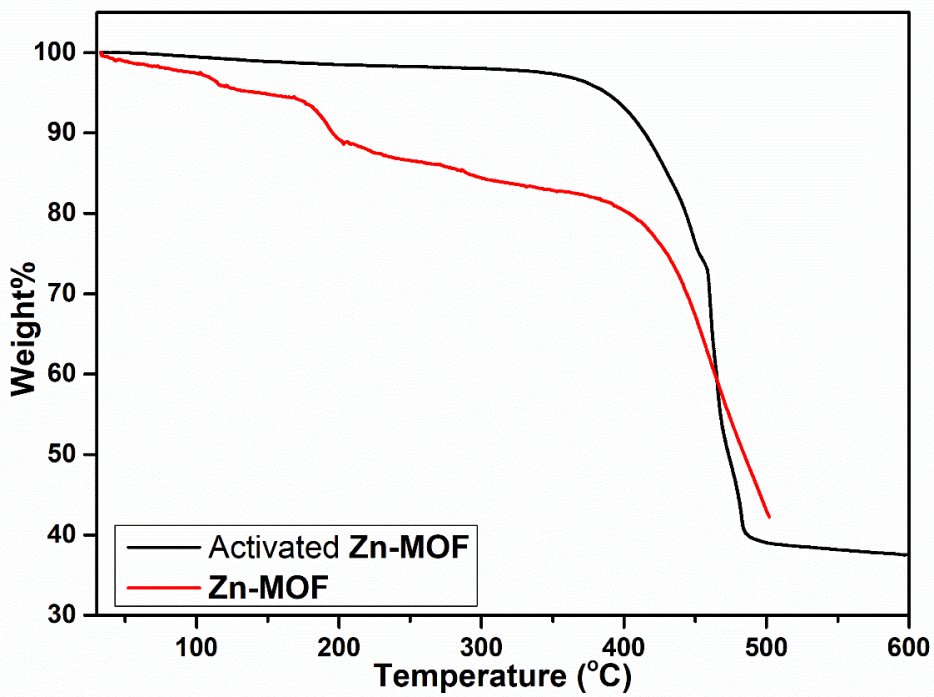

Fig. S9 TGA profiles of **Zn-MOF** and activated **Zn-MOF**.

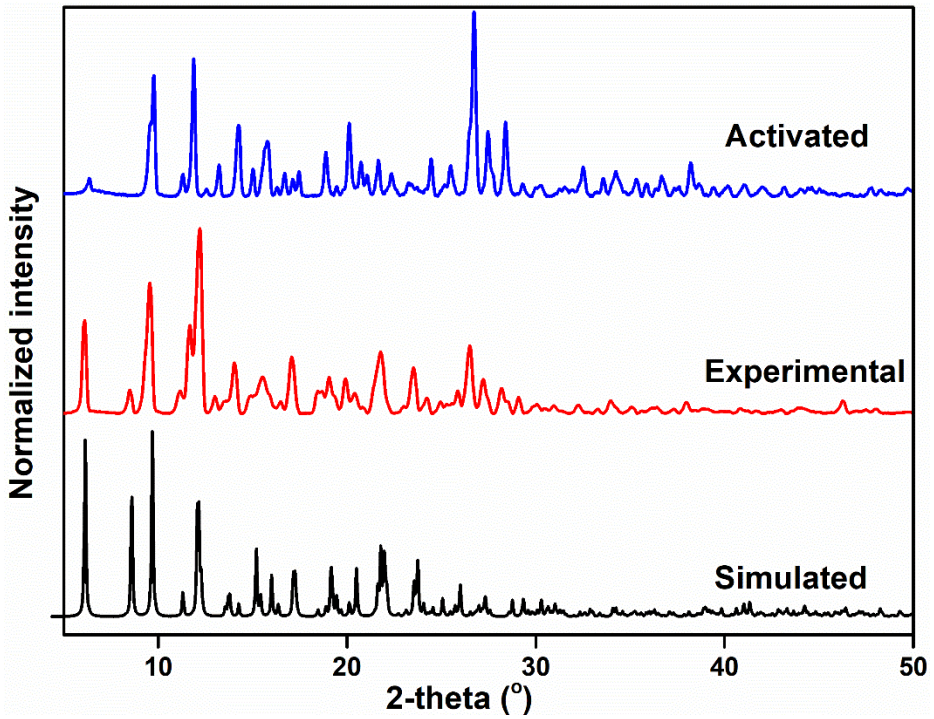

Fig. S10 PXRD patterns of **Zn-MOF** and activated **Zn-MOF**.

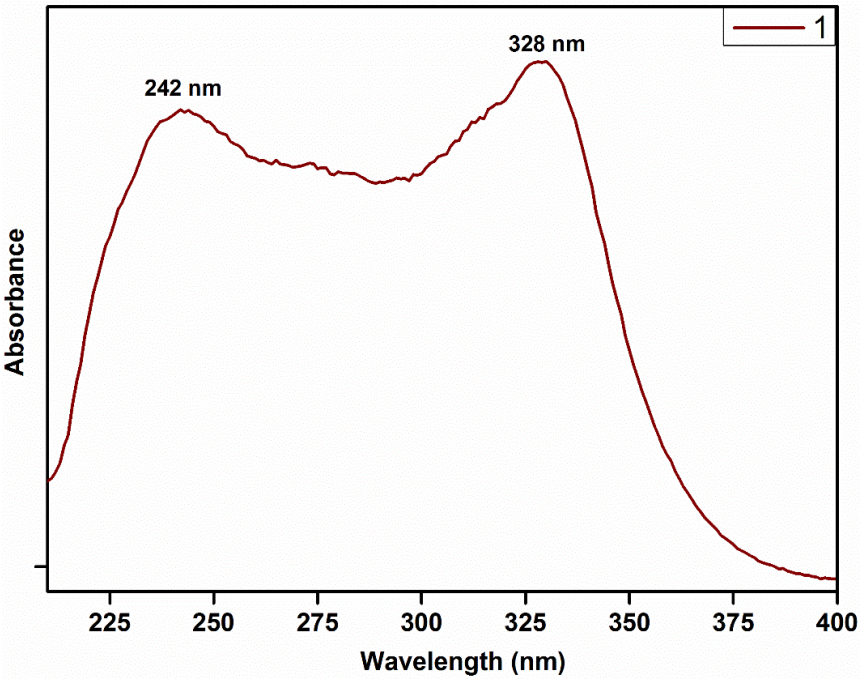

Fig. S11 Solid-state absorption spectrum of **1**.

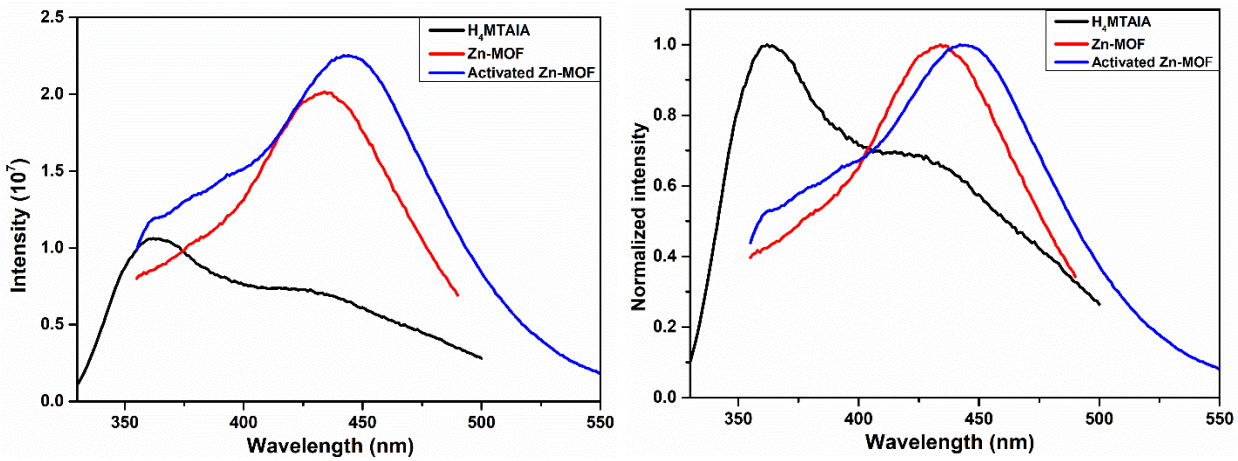

Fig. S12 Fluorescence spectra of H_2ATAIA, **Zn-MOF** and activated **Zn-MOF** in water suspension.

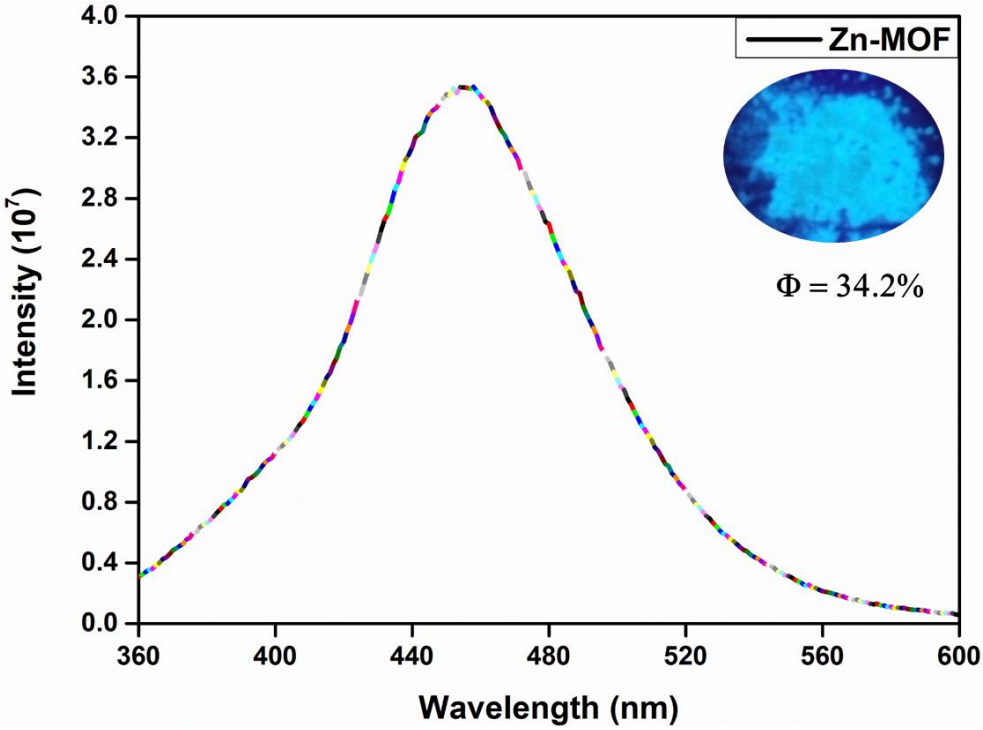

Fig. S13 Solid-state fluorescence spectrum of **1**.

Section 5: Gas/vapor sorption of 1

BET Surface Area Analysis. For this analysis, the BET equation is considered:

$$\nu = c\nu_m x / (1-x)[1 + (c-1)x]$$

where, $x = p/p_0$, ν is the volume of nitrogen adsorbed per gram of MOF at STP, ν_m is the monolayer capacity, and c is related to the heat of adsorption. It is noted that the line is fit to the low pressure isotherm data with range $0.05 < x < 0.3$.

The surface area is then calculated from: $A = \nu_m \sigma_0 N_{a\nu}$

where, σ_0 is the cross-sectional area of nitrogen at liquid density (16.2 Å) and $N_{a\nu}$ is Avogadro's number.

These calculations are done through the "BET analysis" and "Langmuir analysis" function embedded in the Belsorp Adsorption/Desorption Data Analysis software version 6.3.1.0.

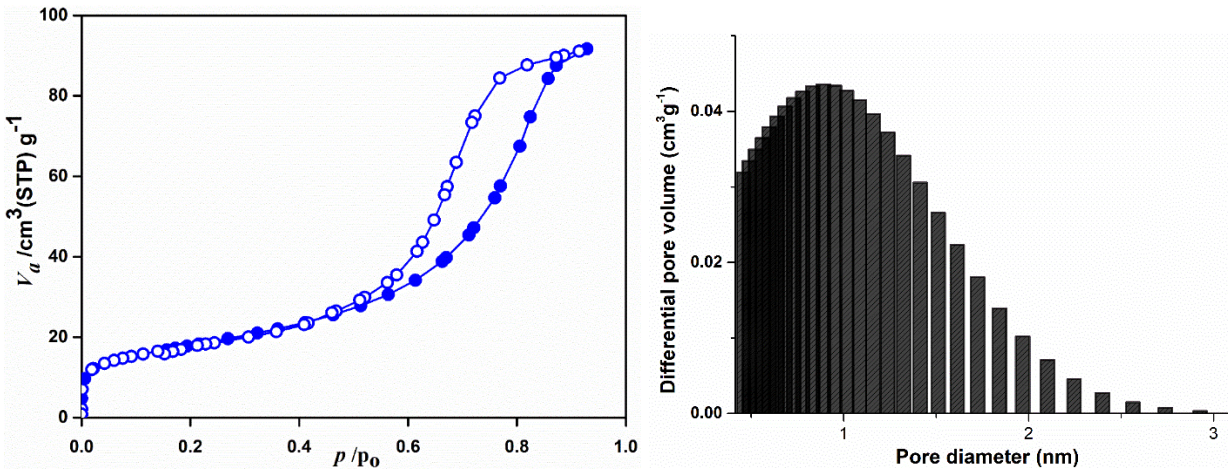

Fig. S14 N_2 sorption isotherm of **1**. Filled and open symbols denote adsorption and desorption, respectively. Pore size distribution using NDLS method.

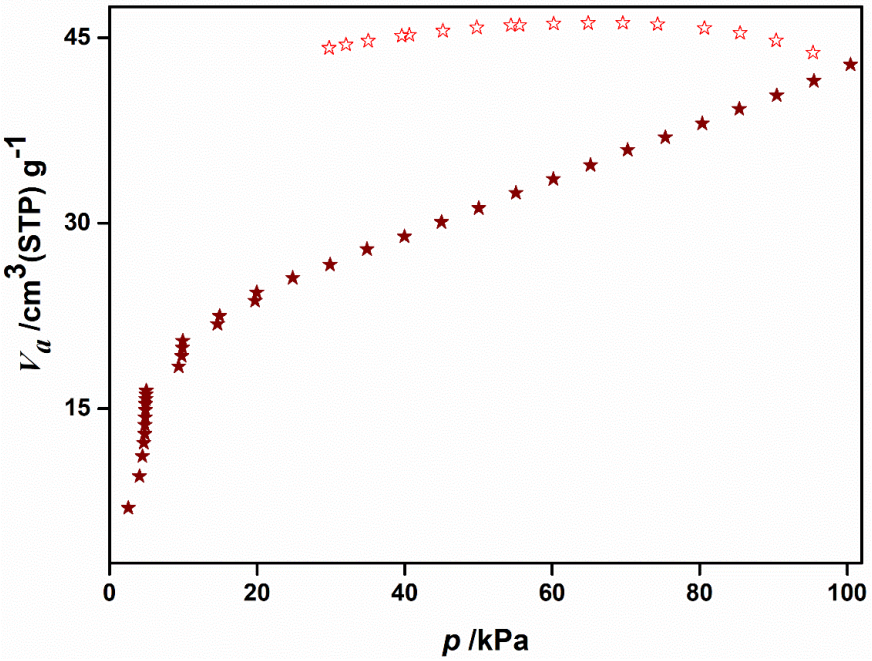

Fig. S15 H_2 sorption isotherm of **1**. Filled and open symbols denote adsorption and desorption, respectively.

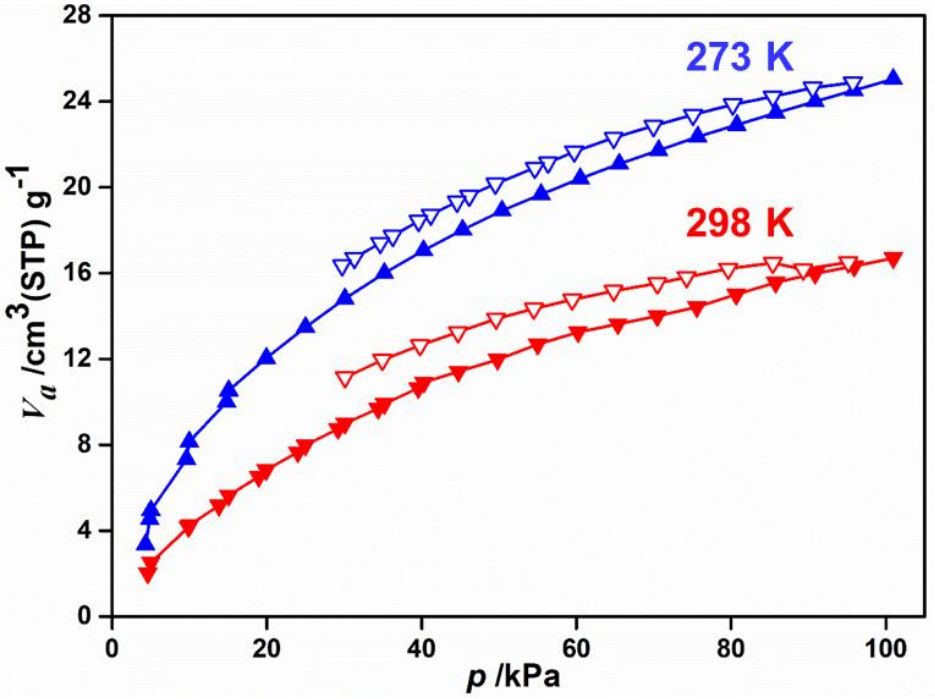

Fig. S16 CO_2 sorption isotherms of **1** at 298 K and 273 K. Filled and open symbols denote adsorption and desorption, respectively.

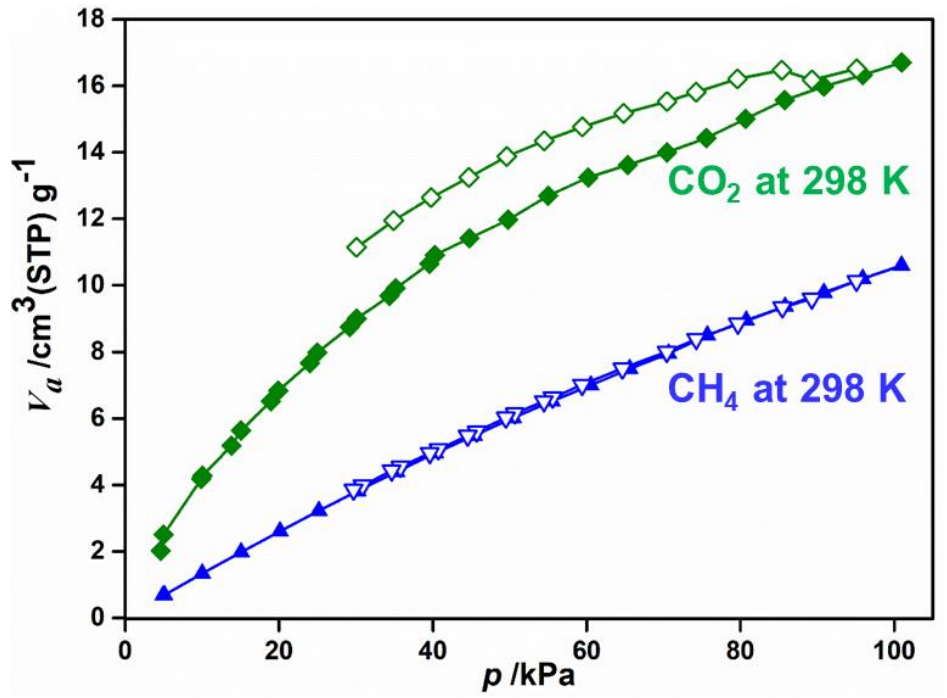

Fig. S17 CO_2 and CH_4 sorption isotherms of **1** at 298 K. Filled and open symbols denote adsorption and desorption, respectively.

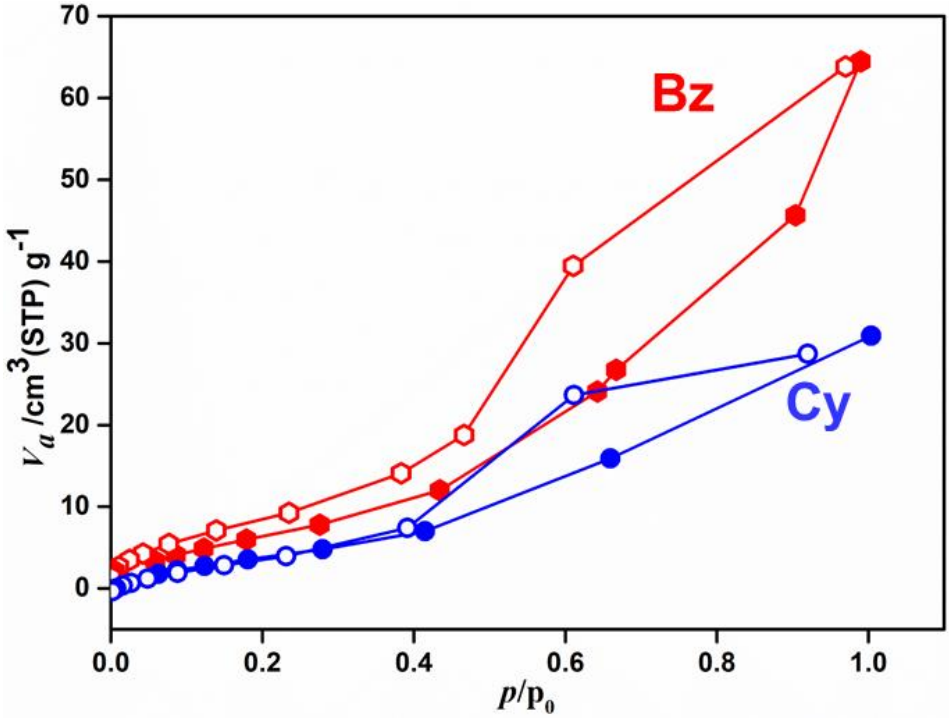

Fig. S18 Benzene (Bz) and cyclohexane (Cy) sorption isotherms of **1** at 298 K. Filled and open symbols denote adsorption and desorption, respectively.

Section 6: Details of fluorescence experiments and calculations

Fluorescence study. In a typical experimental setup, 1 mg of finely ground activated **Zn-MOF** (**1**) is weighed and added to quartz cuvette (path length of 1 cm) containing 2 mL of different solvents under stirring to form a uniform suspension for the molecular decoding experiment. The dispersible nature of **1** will facilitate vicinal contact between the host framework and different solvents. The fluorescence spectra were recorded upon excitation at 320 nm. The fluorescence response in 350-520 nm range upon excitation at 320 nm was measured *in-situ* after incremental addition of freshly prepared aqueous nitro-analyte solutions (1 mM) and corresponding fluorescence intensity was monitored at 443 nm for **1** in water. The solution was stirred at constant rate in fluorescence instrument with stirring attachment during experiment to maintain well dispersed of solution. All the experiments were performed three times and consistent results were reported.

Time-resolved emission studies. Lifetime measurements of **1** excited at 320 nm were carried out using a picosecond time-correlated single photon counting system (TCSPC, model Horiba JobinYvon) equipped with a pulse diode laser. The repetition rate was kept constant at 1 MHz and time to amplitude converter was fixed in the range of 200 ns (0.54 ns per channel). The lifetime decay profiles of **1** were analysed and fitted with a tri-exponential term based on χ^2 (1 ± 0.2) statistics by using the DAS 6.3 fluorescence decay analysis software. The average lifetime, $\tau_{(avg)}$, was evaluated using the following equation:
The average lifetime was evaluated using the following equation

$$\tau_{(avg)} = \frac{\alpha_1\tau_1^2 + \alpha_2\tau_2^2 + \alpha_3\tau_3^2}{\alpha_1\tau_1 + \alpha_2\tau_2 + \alpha_3\tau_3}$$

where, τ is the average lifetime and α is the pre-exponential factor with subscripts 1, 2 and 3 representing various species. The compound was well suspended in water and the fluorescence decay for the probe and after addition of analyte were collected at different concentration with different time interval.

The abatement in fluorescence lifetime of luminescent material attributing that quenching process is dynamic. It is due to the additional relaxation of the excited lifetime from

collision with the quencher. Otherwise, the unchanged fluorescence lifetime of luminescent material attributing that quenching process is static in nature.

Quantum yield measurement. The relative quantum yield was calculated for the compound using 0.1 M quinine sulfate (φ_r = 0.546) as the reference. For the optical density of both the compound and reference was made close to 0.1 by keeping the slit width equal to one. The emission spectra were also recorded for both the compound and reference at the same slit width. The quantum yield of the probes can be determined by using following equation:

$$\varphi_s = \varphi_r \, (OD_r/OD_s) \, (I_s/I_r) \, (n_s^2/n_r^2)$$

Where φ_s and φ_r are quantum yields of the probe and the reference, respectively, OD is the optical density, *I* is the area under the curve for the emission spectra and *n* is the refractive index of the medium. For this study quinine sulfate was used as a reference.

Detection limit calculation. For calculating detection limit, nitro-explosives (stock solution) was added to probe (guest-free) (1 mg in 2 mL water/EtOH/DMF) and fluorescent intensity were recorded. By plotting fluorescence intensity with increasing concentration of nitro-explosives, slope (*m*) was calculated from graph. Standard deviation (σ*)* was calculated from four blank measurements of probe. Detection limit is calculated based on the formula: (3σ/*m*).

Spectral overlap calculation. The spectral overlap between the emission spectra of **1'** and absorbance spectra of different NEs were recorded. The effective spectral overlap enhances the resonance energy transfer from the fluorophore of the probe to the non-emissive analytes. Higher the energy transfer, greater the fluorescence quenching efficiency of the analyte. The extent of energy transfer was evaluated by calculating the integral of overlap $J(\lambda)$ values using the equation below[S5]

$$J(\lambda) = \int_0^\infty F_D(\lambda) \, \varepsilon_A(\lambda) \, \lambda^4 \, d\lambda$$

Where, $F_D(\lambda)$ is the corrected fluorescence intensity of donor of the range of λ to $\lambda+d\lambda$ with the total intensity normalized to unity, and ε_A is the extinction coefficient of the NACs at λ in $M^{-1}cm^{-1}$.

(S5) J. R. Lakowicz, *Principles of Fluorescence Spectroscopy*, 3rd ed. Springer, Singapore, 2010.

Exploitation of fluorescence of small solvent molecules by activated 1

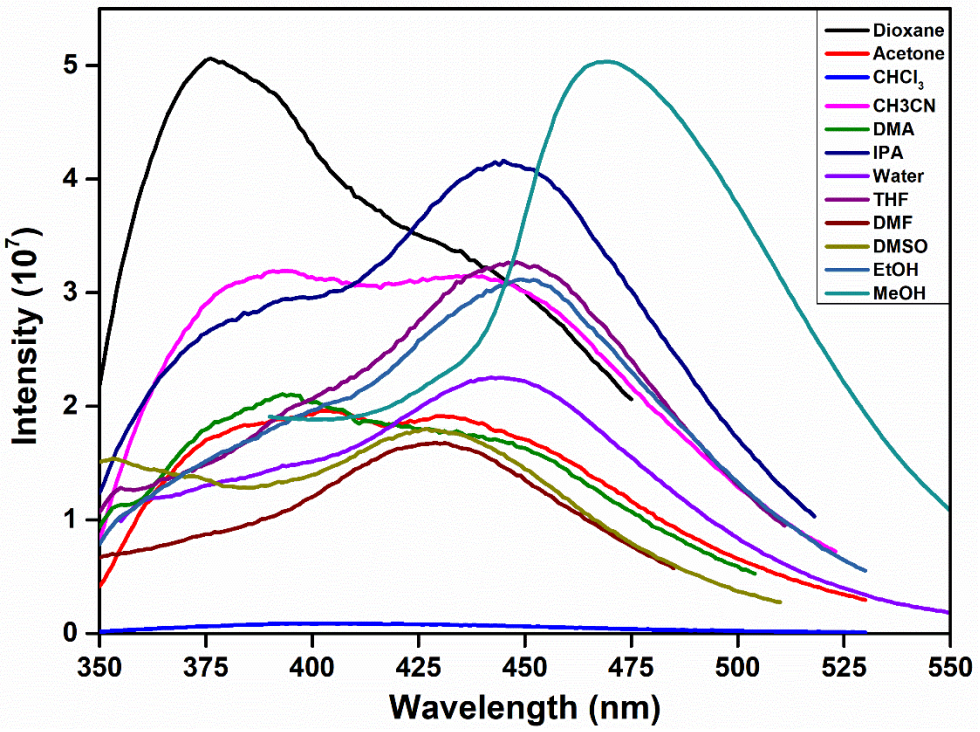

Fig. S19 Fluorescence spectra (bottom) of activated **1** in different solvents.

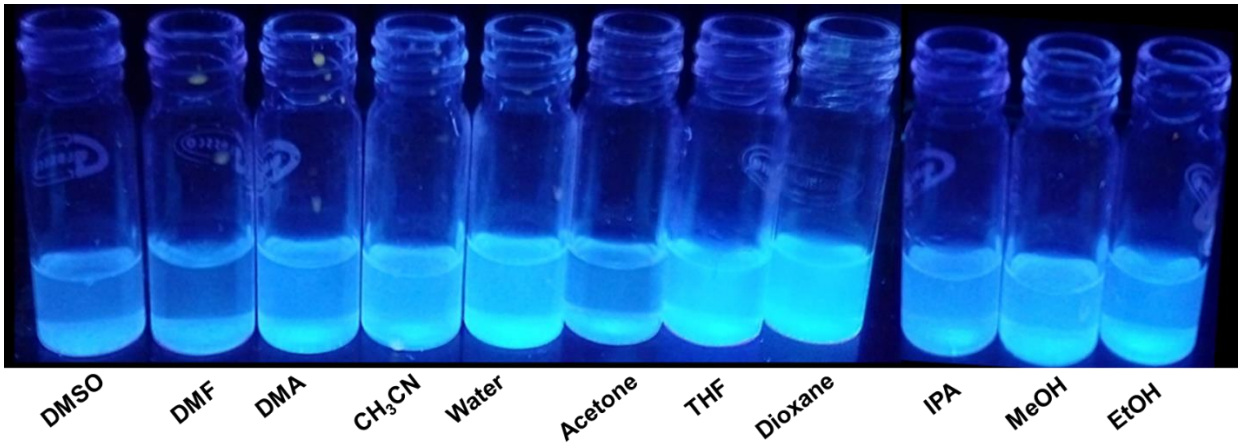

Fig. S20 UV illumination of different solvents in activated **1** (λ = 365 nm).

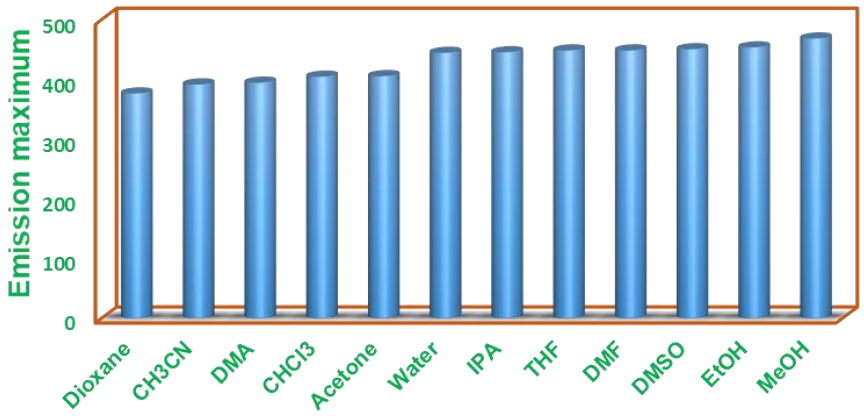

Fig. S21 Shift of emission maximum of activated **1** in different solvents.

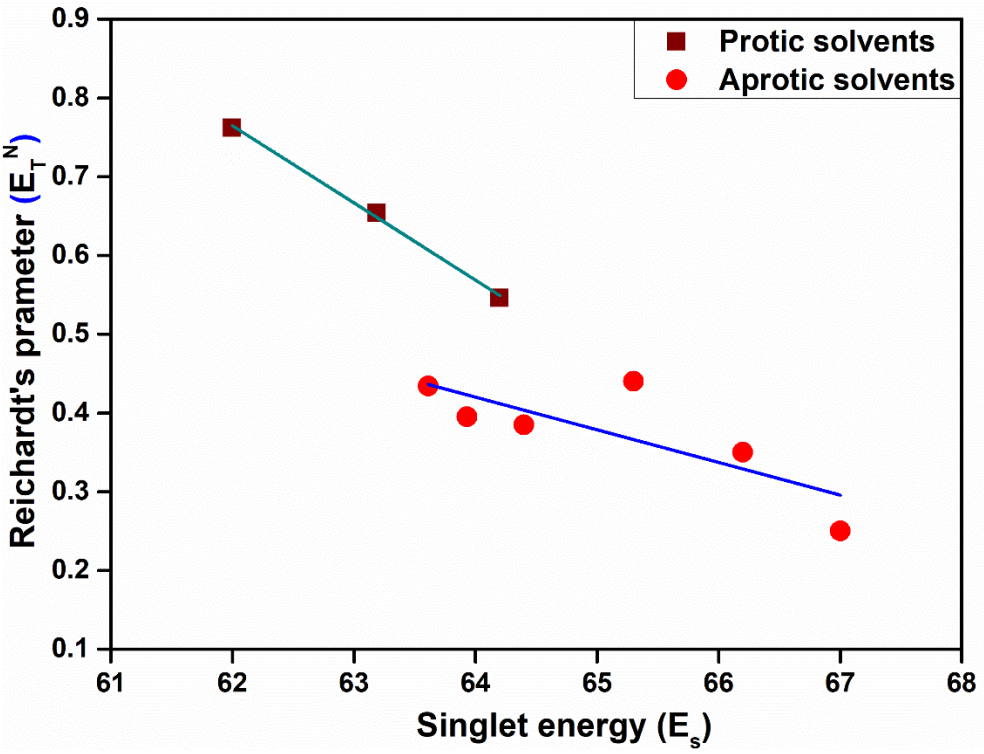

Fig. S22 Correlation of singlet energies (Es) and Reichardt's parameters in various solvents.

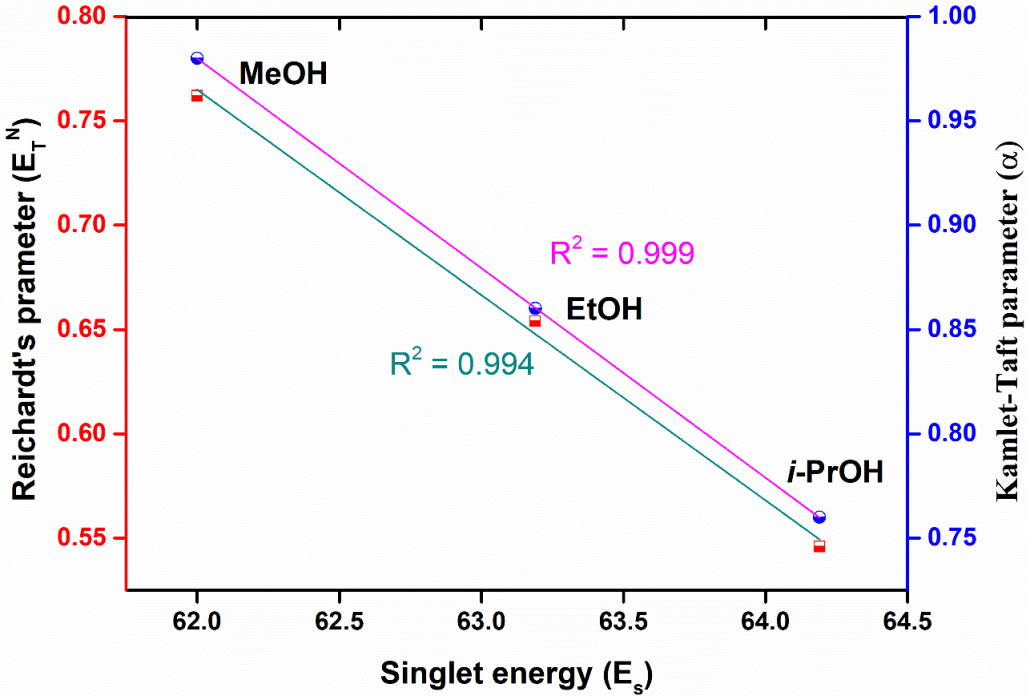

Fig. S23 Correlation of alcoholic solvents with Reichardt's and Kamlet-Taft parameters.

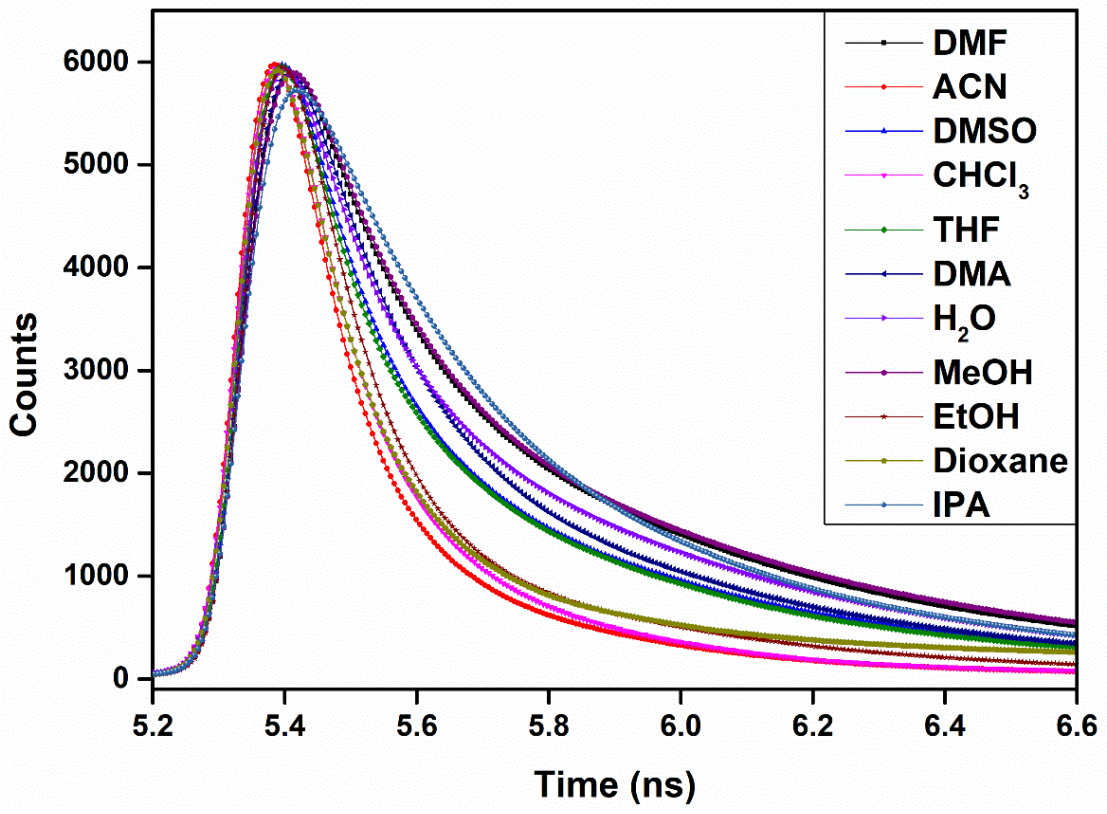

Fig. S24 Lifetime measurements of activated **1** in different solvents.

Section 8: Selective detection of Dunnite

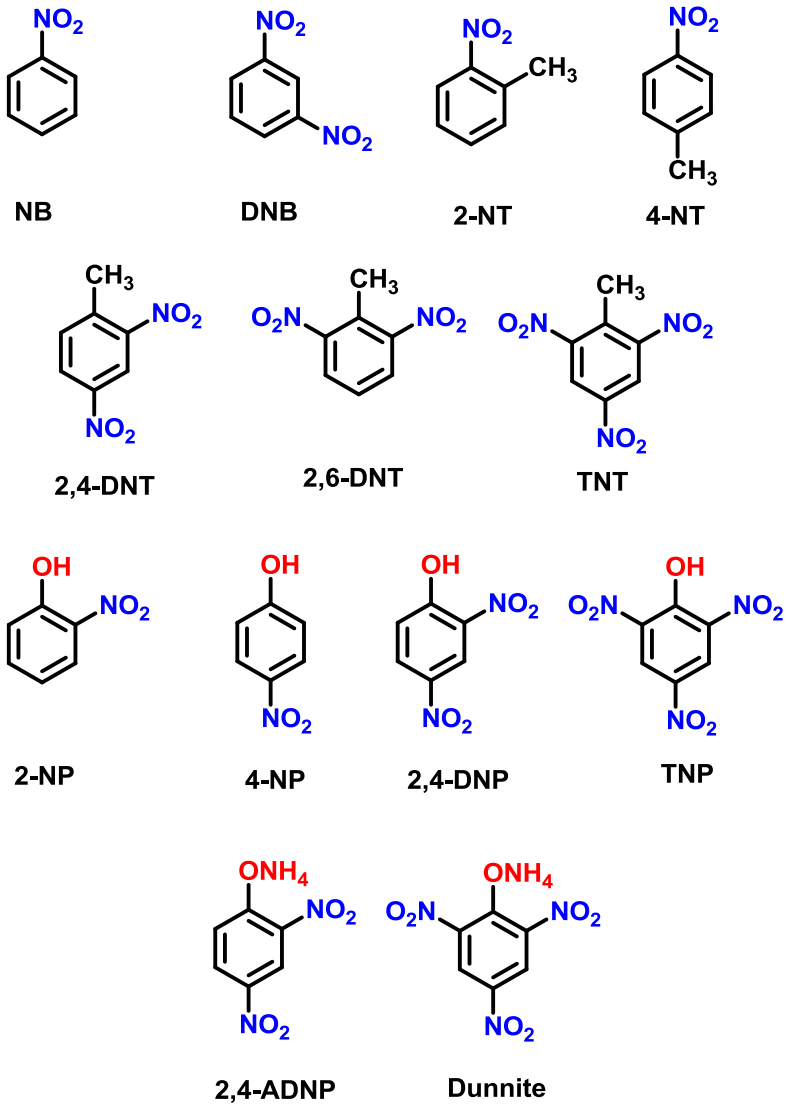

Scheme 3 Structure of different nitro-explosives.

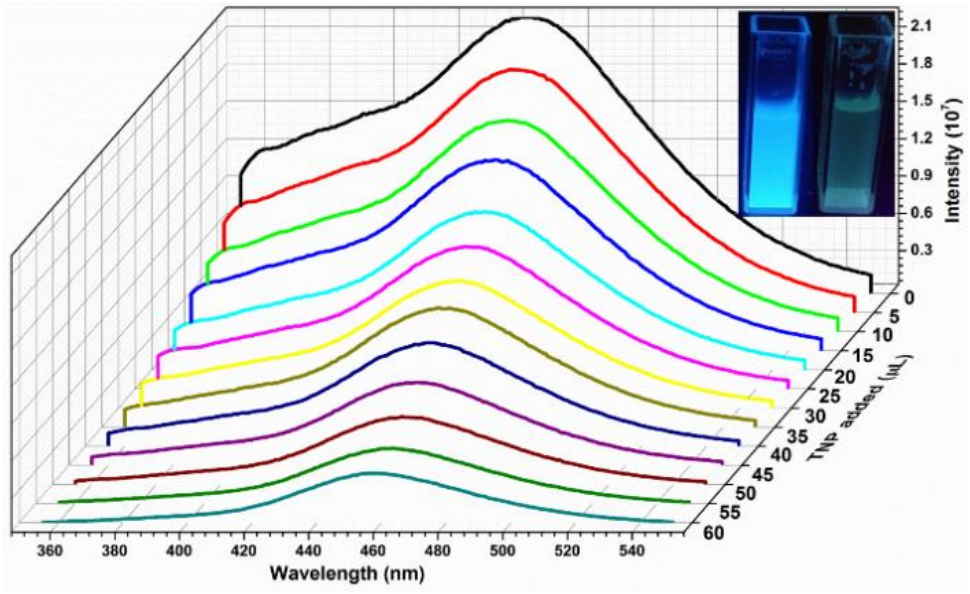

Fig. S25 Emission spectra of activated **1** dispersed in water upon incremental addition of TNP solution (1 mM).

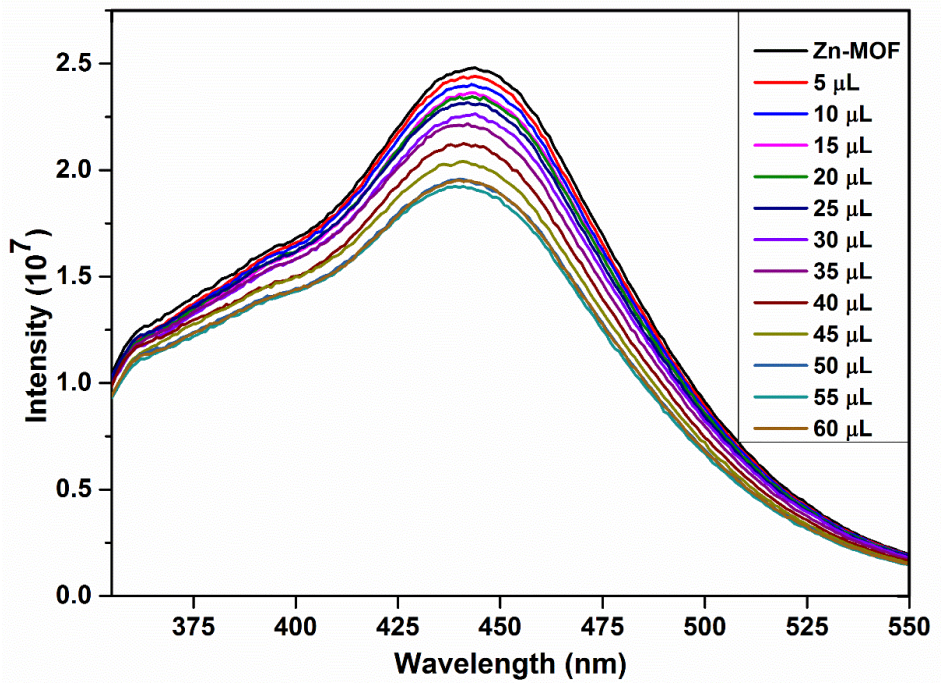

Fig. S26 Emission spectra of activated **1** dispersed in water upon incremental addition of TNT solution (1 mM).

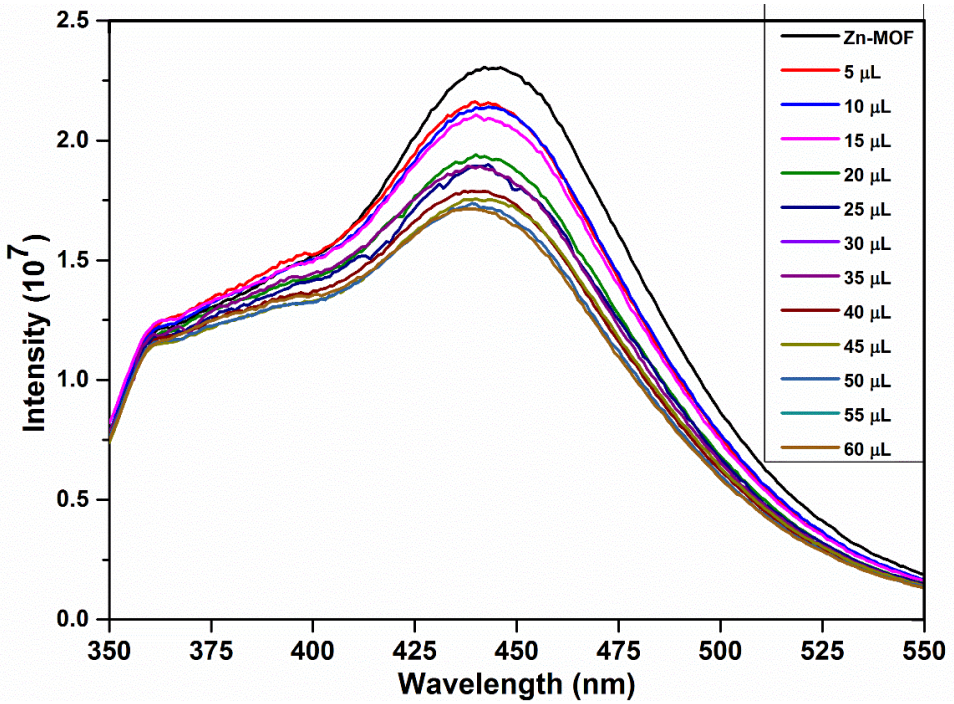

Fig. S27 Emission spectra of activated **1** dispersed in water upon incremental addition of 2,4-DNT solution (1 mM).

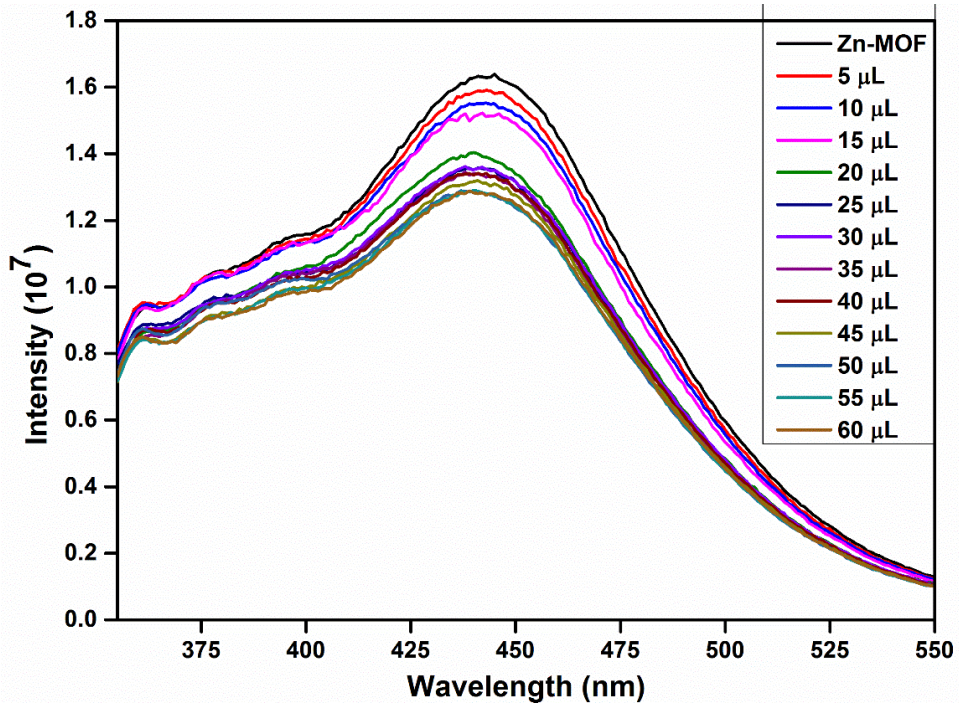

Fig. S28 Emission spectra of activated **1** dispersed in water upon incremental addition of 2,6-DNT solution (1 mM).

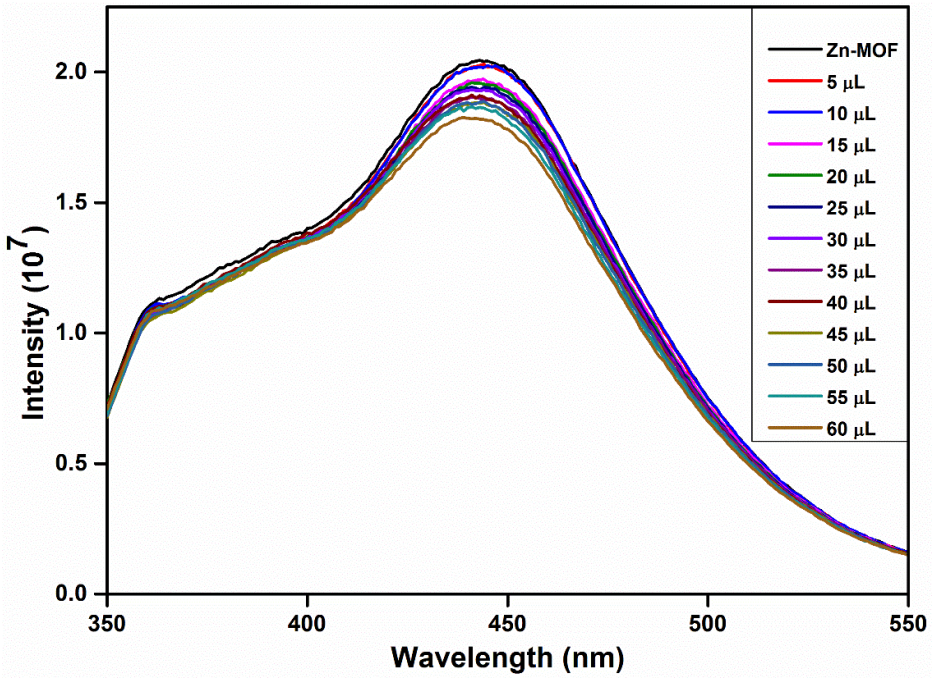

Fig. S29 Emission spectra of activated **1** dispersed in water upon incremental addition of 4-NT solution (1 mM).

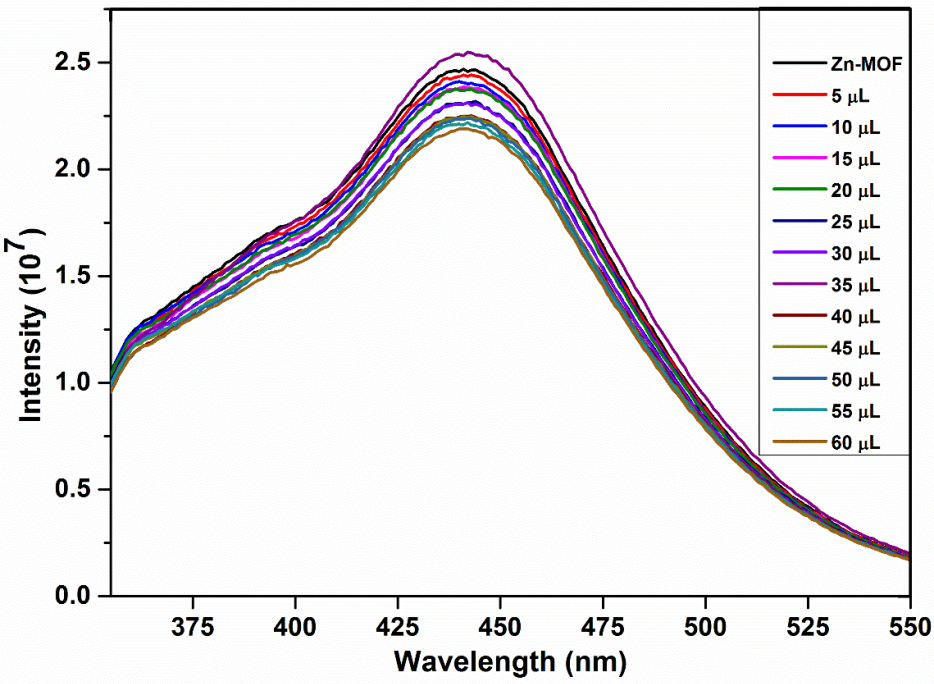

Fig. S30 Emission spectra of activated **1** dispersed in water upon incremental addition of 2-NT solution (1 mM).

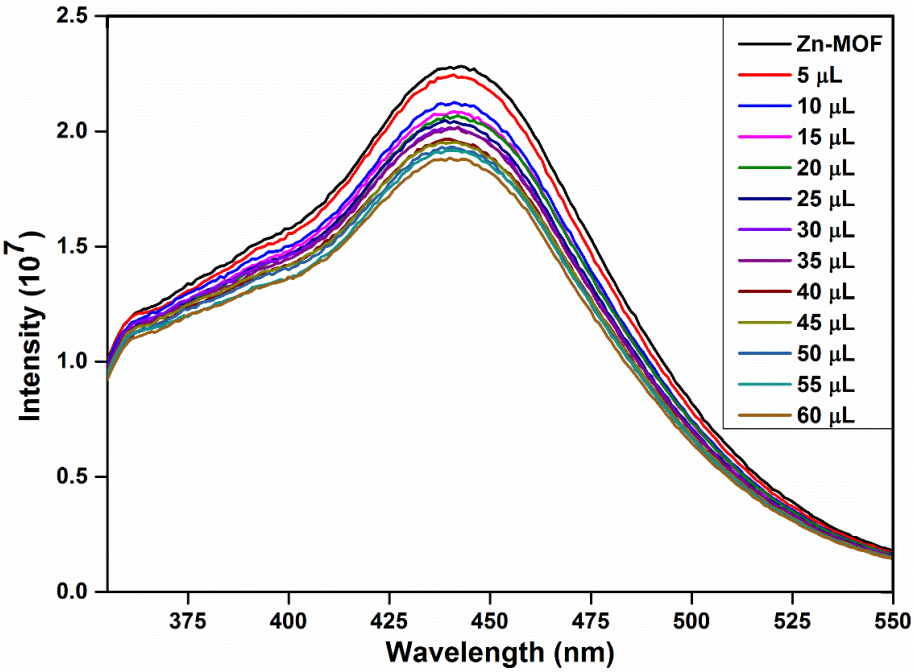

Fig. S31 Emission spectra of activated **1** dispersed in water upon incremental addition of DNB solution (1 mM).

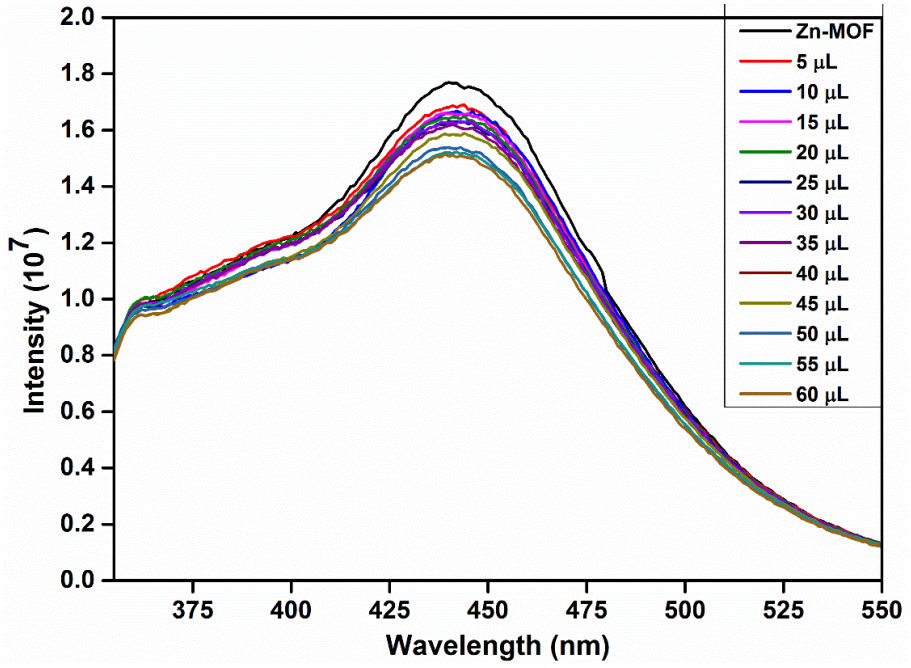

Fig. S32 Emission spectra of activated **1** dispersed in water upon incremental addition of NB solution (1 mM).

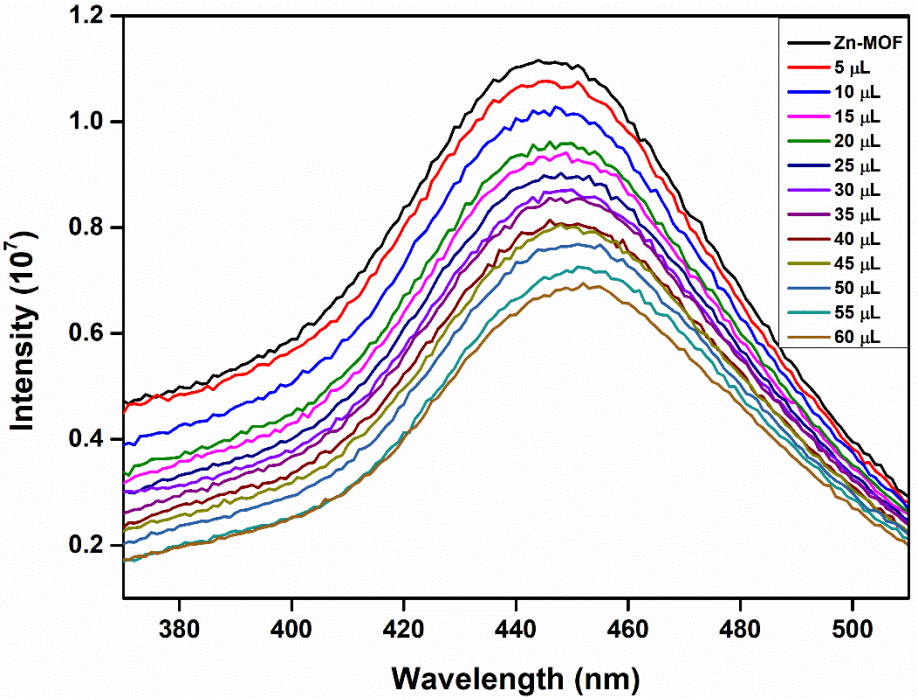

Fig. S33 Emission spectra of activated **1** dispersed in water upon incremental addition of 2,4-ADNP solution (1 mM).

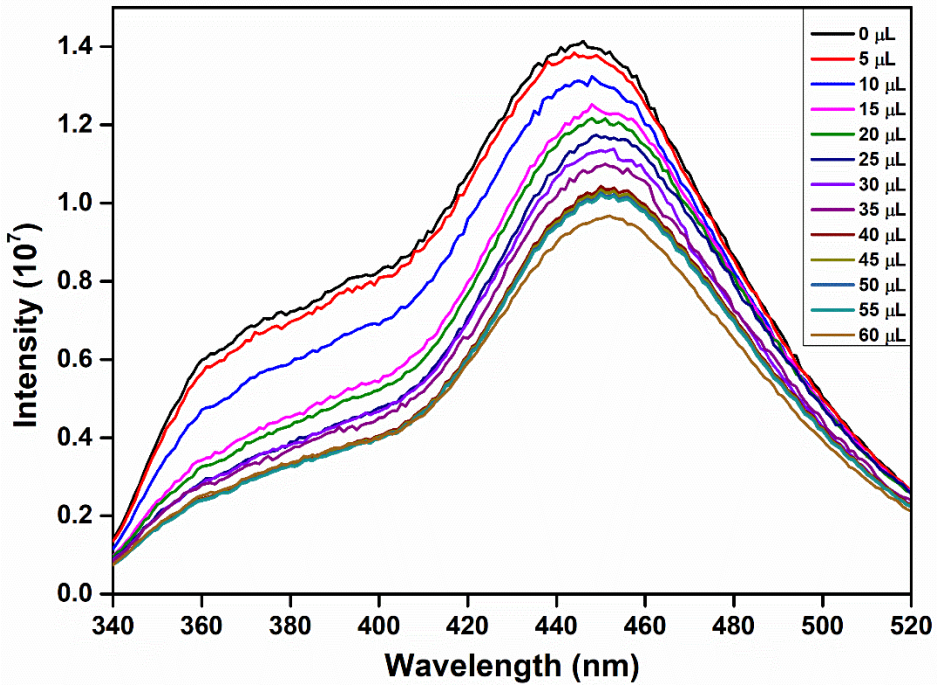

Fig. S34 Emission spectra of activated **1** dispersed in water upon incremental addition of 2,4-DNP solution (1 mM).

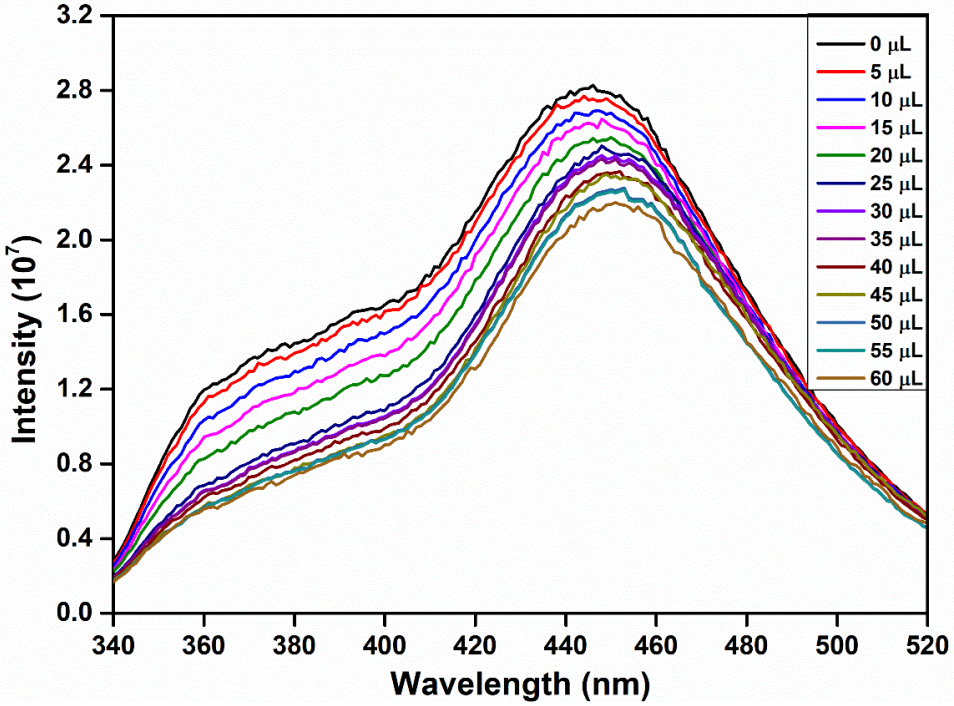

Fig. S35 Emission spectra of activated **1** dispersed in water upon incremental addition of 4-NP solution (1 mM).

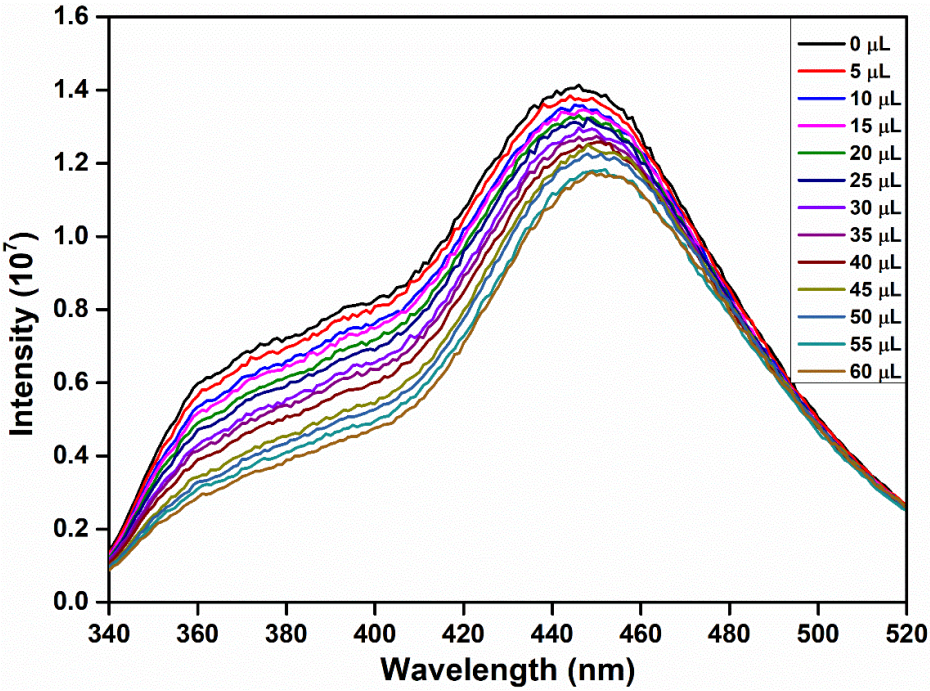

Fig. S36 Emission spectra of activated **1** dispersed in water upon incremental addition of 2-NP solution (1 mM).

Section 9: Stern-Volmer plots

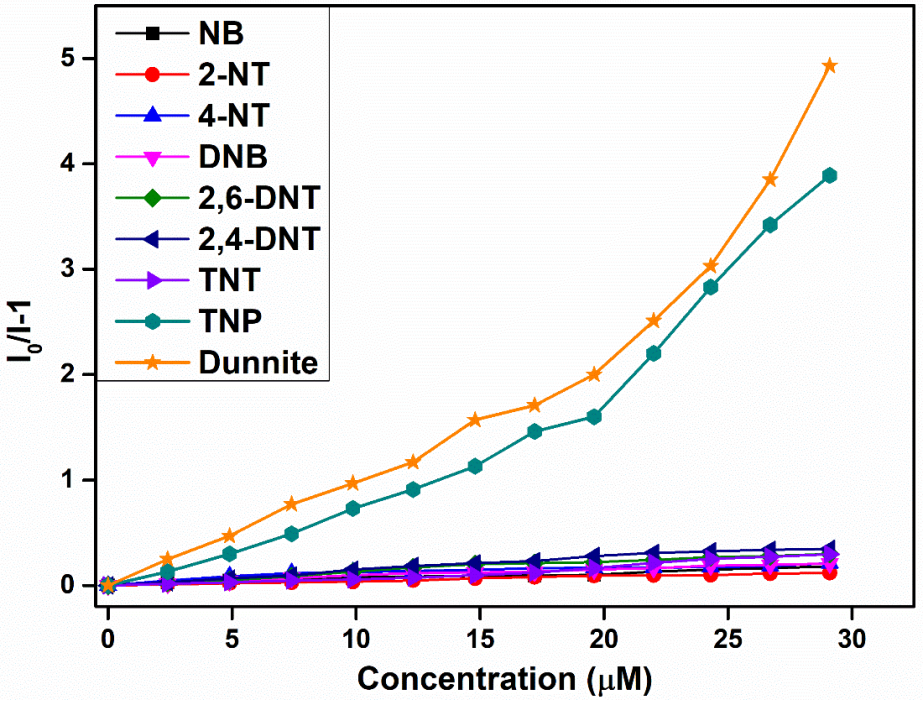

Fig. S37 Stern-Volmer plots of different nitro-analytes for activated **1**.

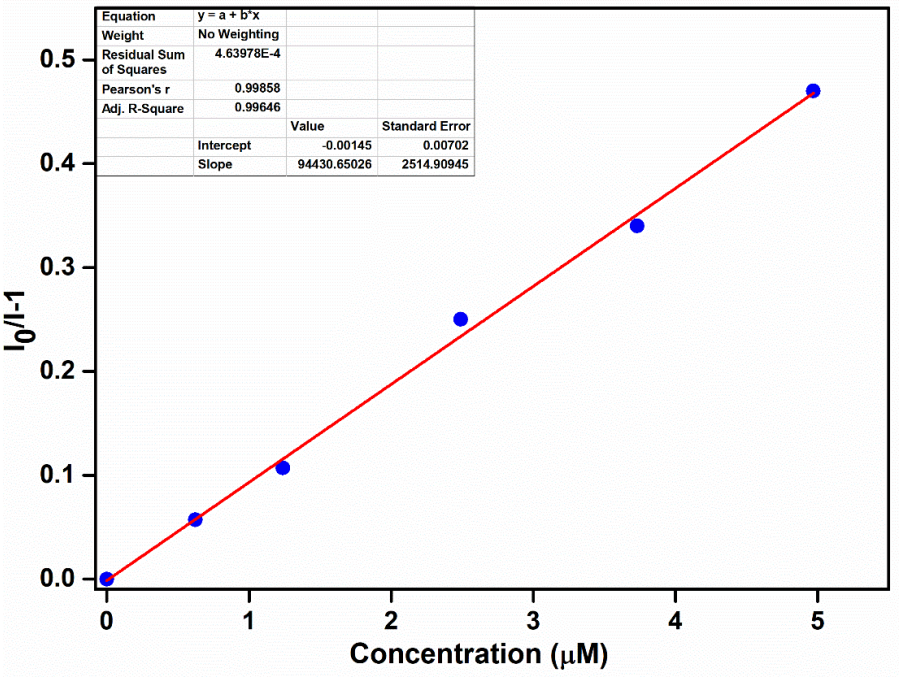

Fig. S38 Stern-Volmer plot for Dunnite. The relative fluorescence intensity is linear with Dunnite concentration in the range of 0–5 μM, $I_0/I = 1 + 9.44 \times 10^4$ [Dunnite] ($R^2 = 0.995$).

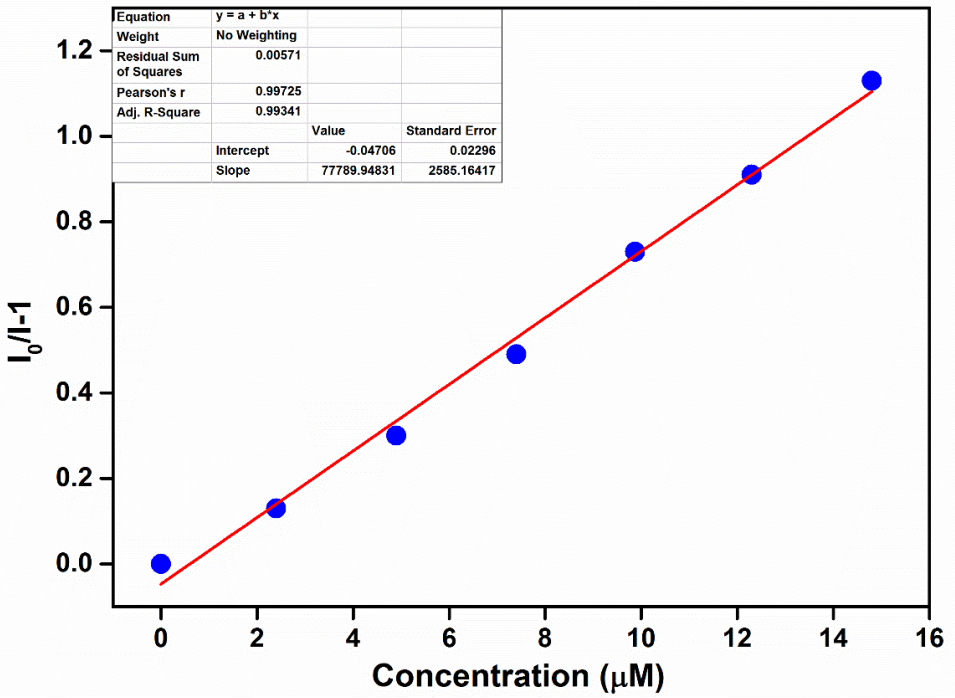

Fig. S39 Stern-Volmer plot for TNP. The relative fluorescence intensity is linear with TNP concentration in the range of 0–15 μM, $I_0/I = 1 + 7.77 \times 10^4$ [TNP] ($R^2 = 0.993$).

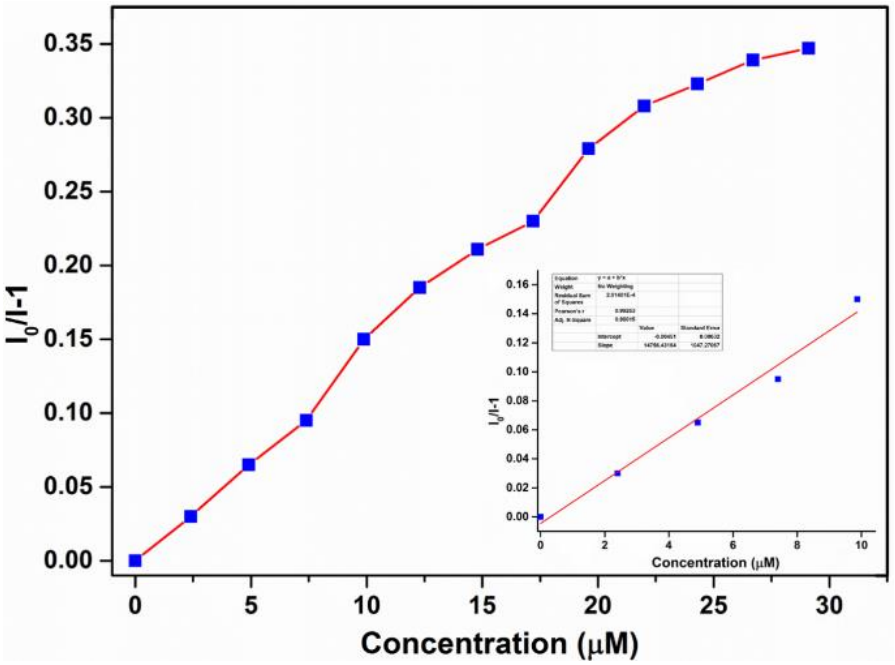

Fig. S40 Stern-Volmer plot for TNT. The relative fluorescence intensity is linear with TNT concentration, $I_0/I = 1 + 1.47 \times 10^4$ [TNT] ($R^2 = 0.98$).

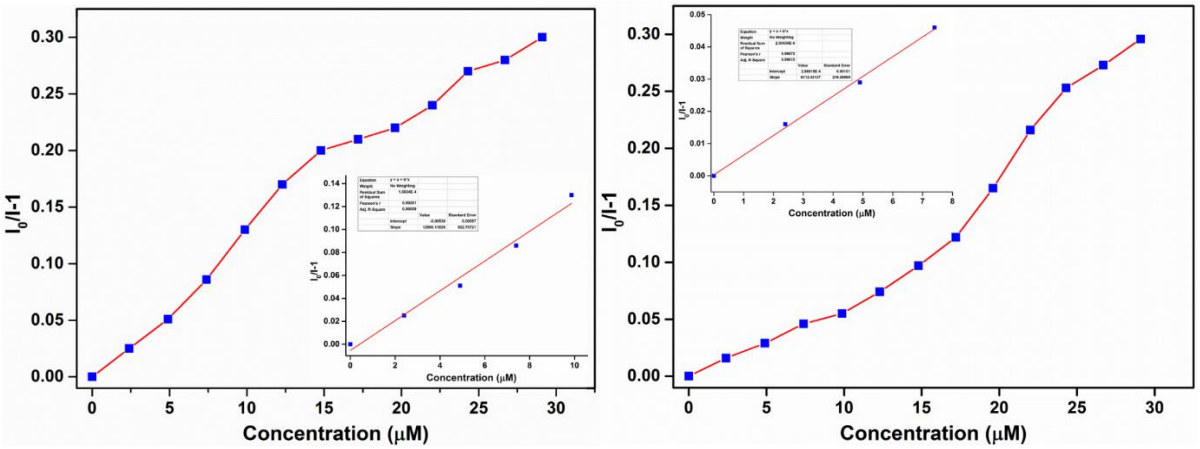

Fig. S41 Stern-Volmer plots for 2,4-DNT (left) and 2,6-DNT (right). The relative fluorescence intensity is linear with 2,4-DNT and 2,6-DNT concentration. Where, $I_0/I = 1 + 1.29 \times 10^4$ [2,4-DNT] ($R^2 = 0.997$) and $I_0/I = 1 + 6112.4$ [2,6-DNT] ($R^2 = 0.999$).

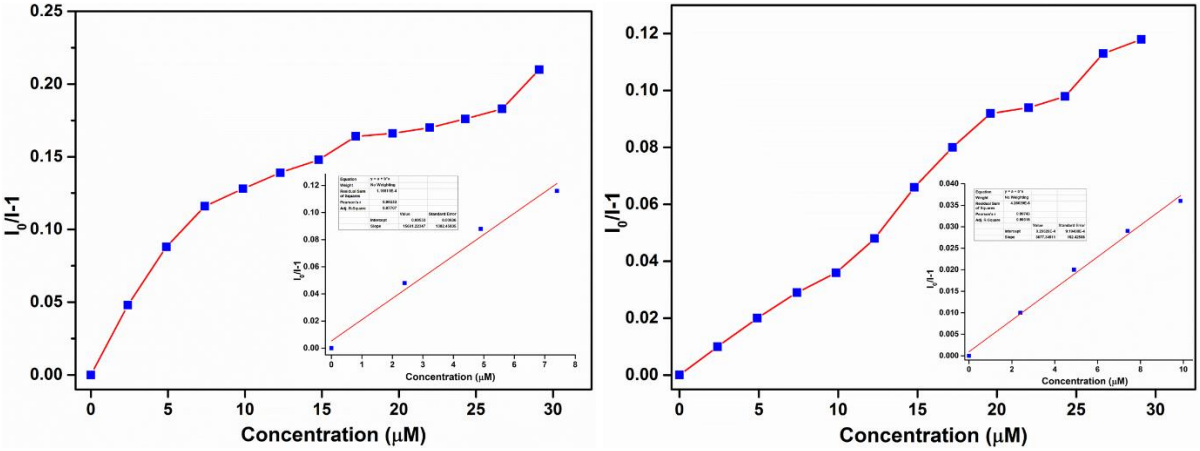

Fig. S42 Stern-Volmer plots for 4-NT (left) and 2-NT (right). The relative fluorescence intensity is linear with 4-NT and 2-NT concentration. Where, $I_0/I = 1 + 1.06 \times 10^4$ [4-NT] ($R^2 = 0.994$) and $I_0/I = 1 + 3.67 \times 10^3$ [2-NT] ($R^2 = 0.995$).

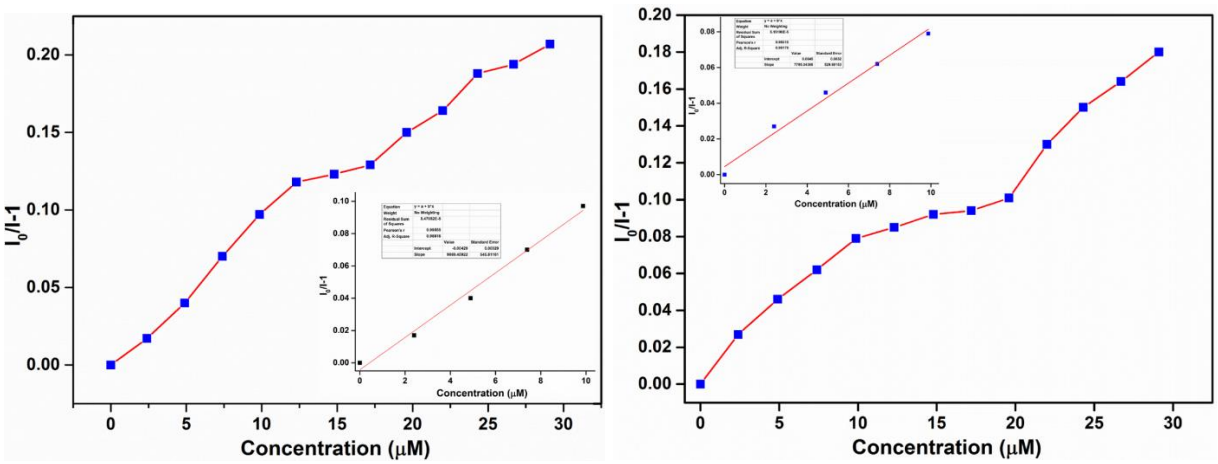

Fig. S43 Stern-Volmer plots for DNB (left) and NB (right). The relative fluorescence intensity is linear with DNB and NB concentration. Where, $I_0/I = 1 + 9989.2$ ([DNB]) ($R^2 = 0.998$) and $I_0/I = 1 + 7.93 \times 10^3$ ([NB]) ($R^2 = 0.9941$).

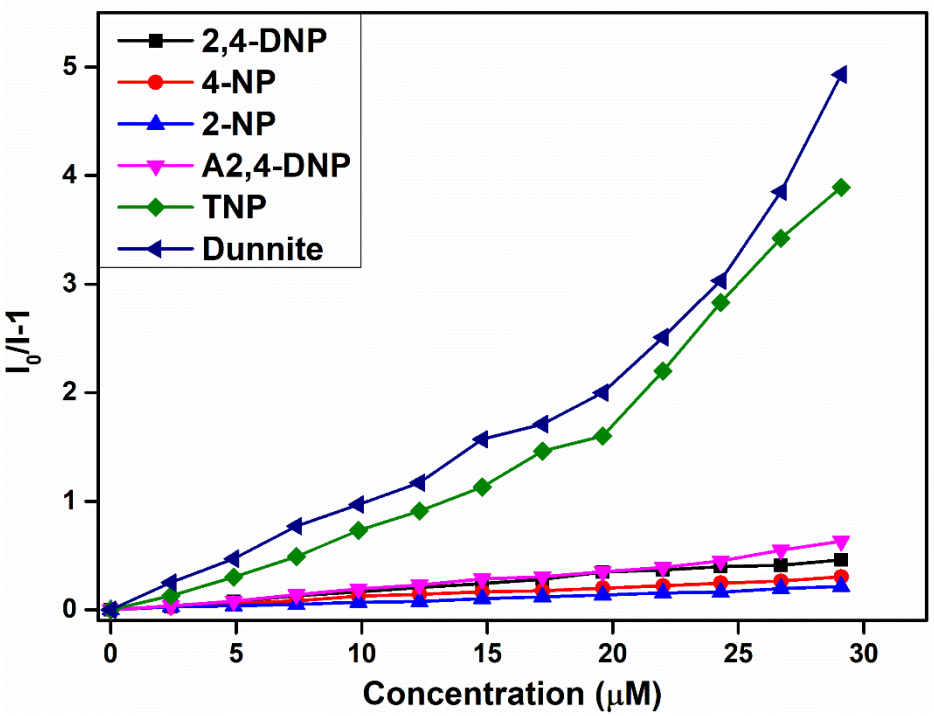

Fig. S44 Stern-Volmer plots for different nitro-phenols, 2,4-ADNP and Dunnite in water.

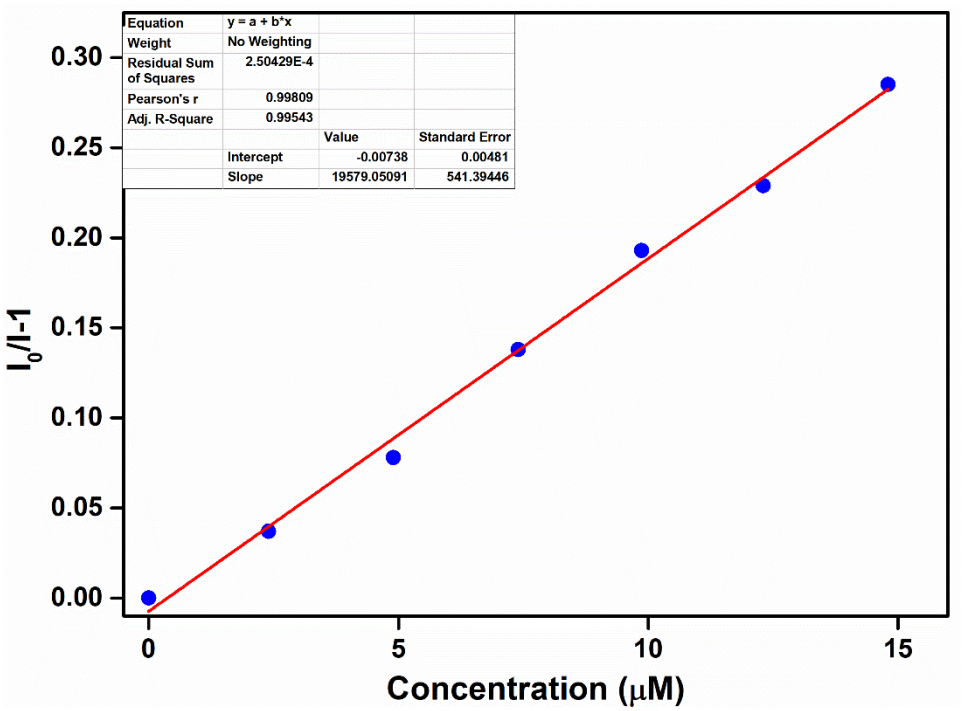

Fig. S45 The relative fluorescence intensity is linear with 2,4-ADNP concentration in the range of 0–15 μM, $I_0/I = 1 + 1.95 \times 10^4$ [2,4-ADNP] ($R^2 = 0.995$).

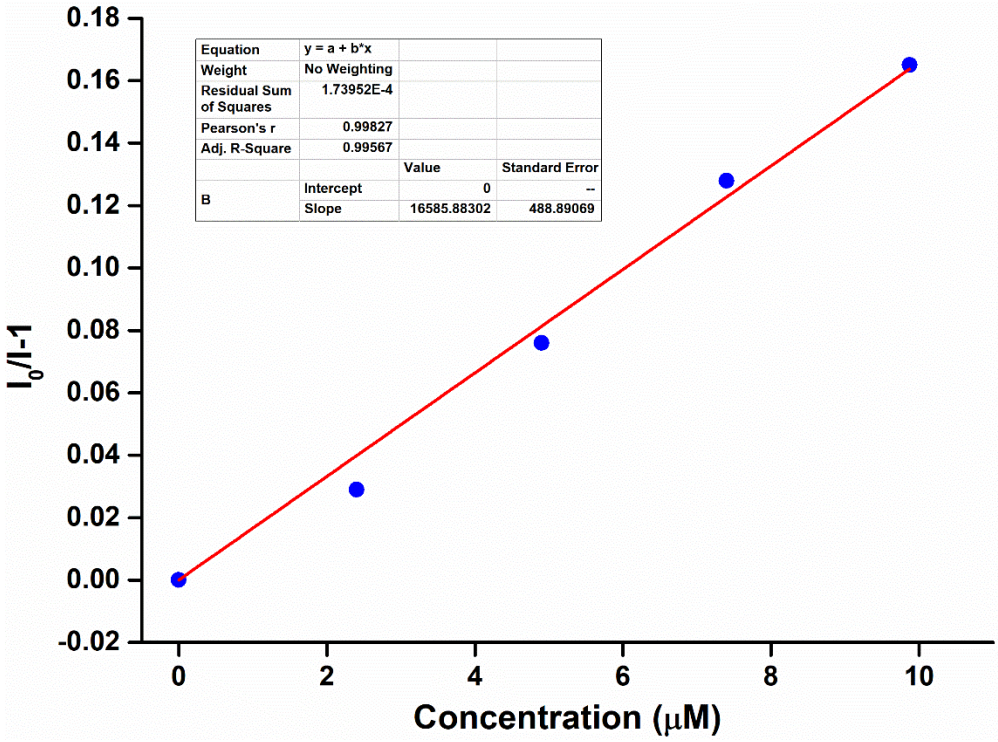

Fig. S46 The relative fluorescence intensity is linear with 2,4-DNP concentration in the range of 0–10 μM, $I_0/I = 1 + 1.65 \times 10^4$ [2,4-DNP] ($R^2 = 0.995$).

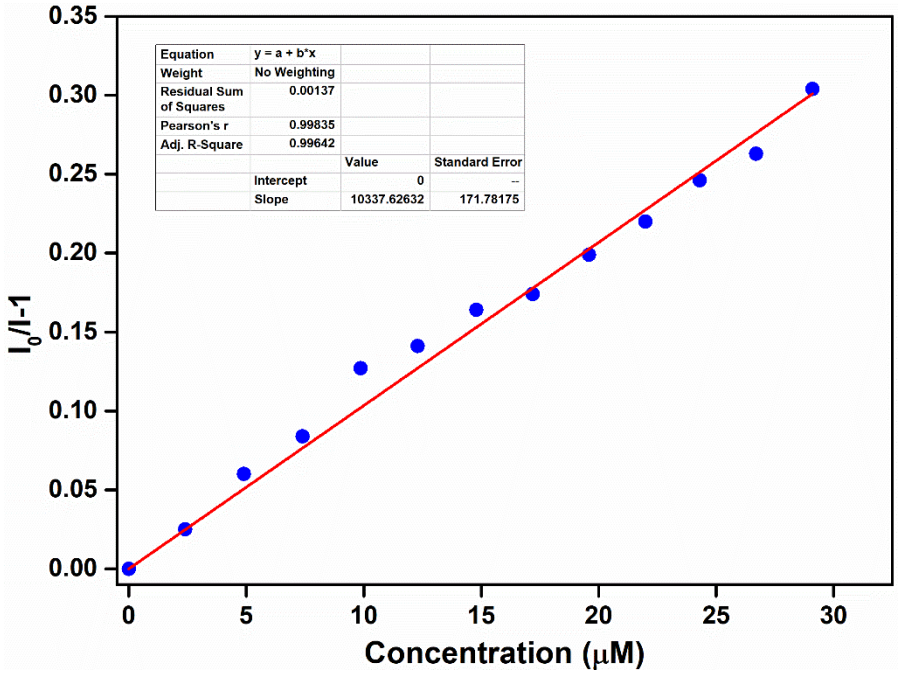

Fig. S47 The relative fluorescence intensity is linear with 4-NP concentration in the range of 0–30 μM, $I_0/I = 1 + 1.033 \times 10^4$ [4-NP] ($R^2 = 0.996$).

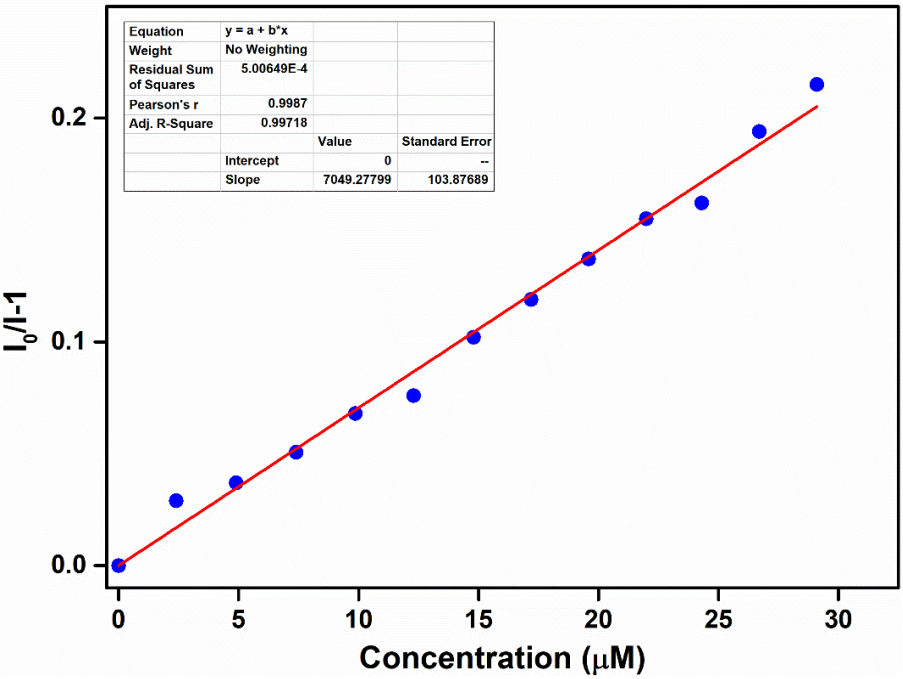

Fig. S48 The relative fluorescence intensity is linear with 2-NP concentration in the range of 0–30 μM, $I_0/I = 1 + 7.049 \times 10^3$ [2-NP] ($R^2 = 0.997$).

Section 10: Ammonium nitrate (AN) detection in water

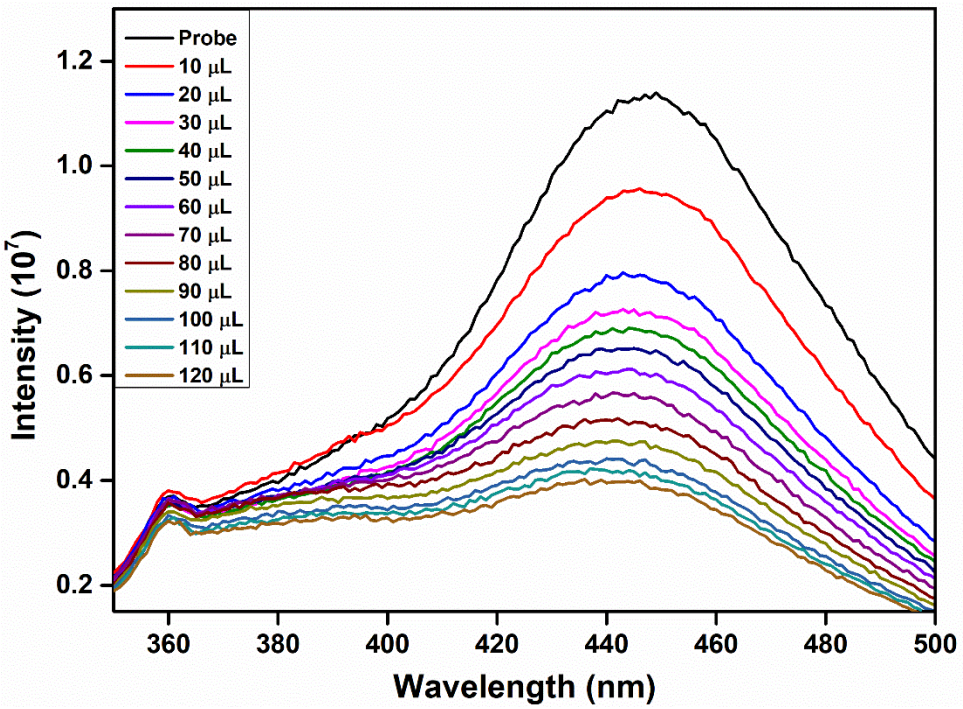

Fig. S49 Emission spectra of activated **1** dispersed in water upon incremental addition of AN solution (1 mM).

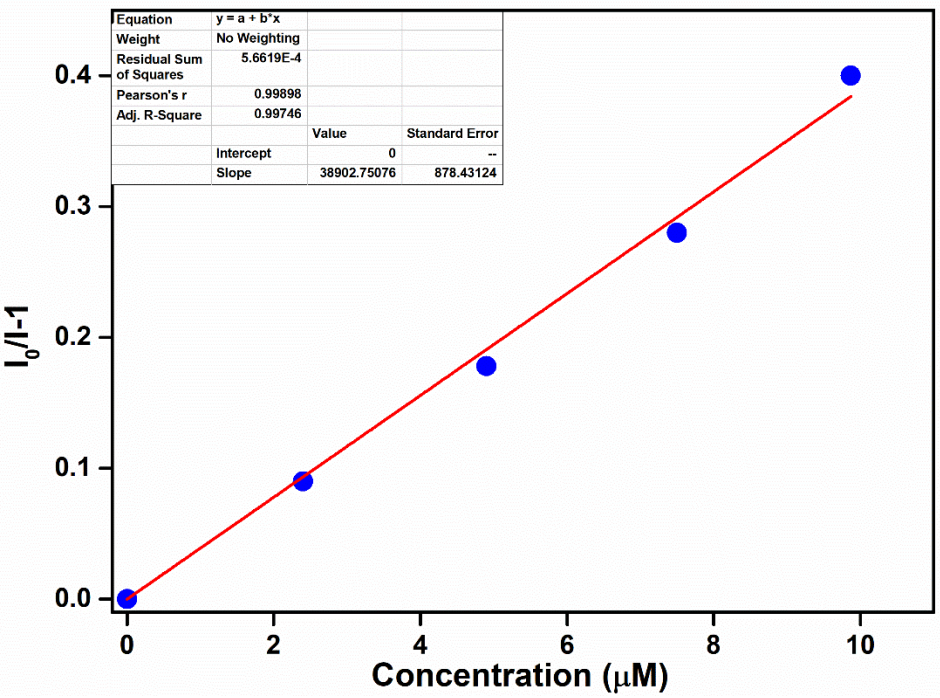

Fig. S50 The relative fluorescence intensity is linear with AN in the lower concentration range, $I_0/I = 1 + 3.89 \times 10^4$ [AN] ($R^2 = 0.997$).

Section 11: Dunnite sensing in EtOH and DMF

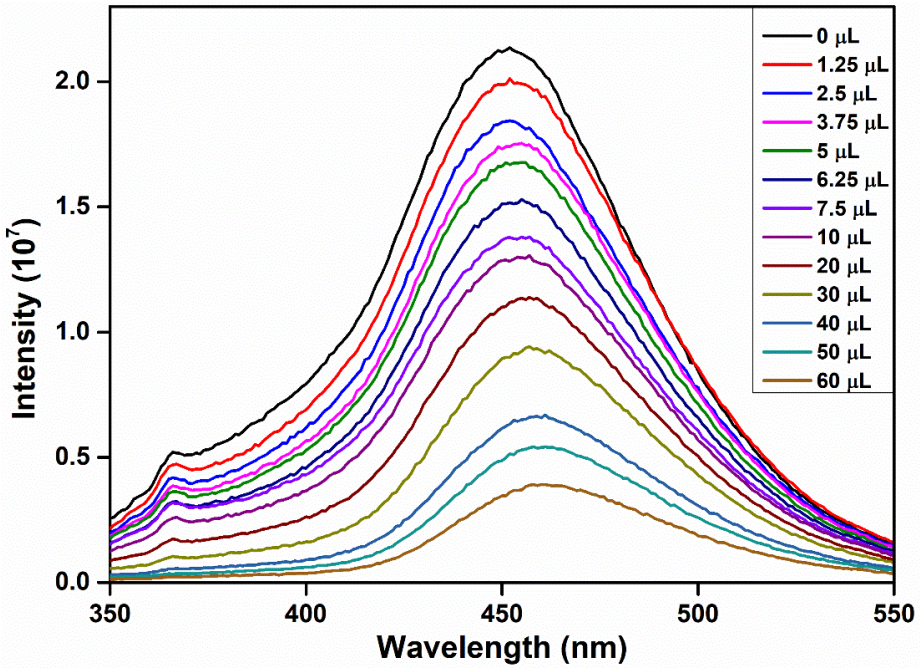

Fig. S51 Emission spectra of activated **1** dispersed in EtOH upon incremental addition of Dunnite solution (1 mM).

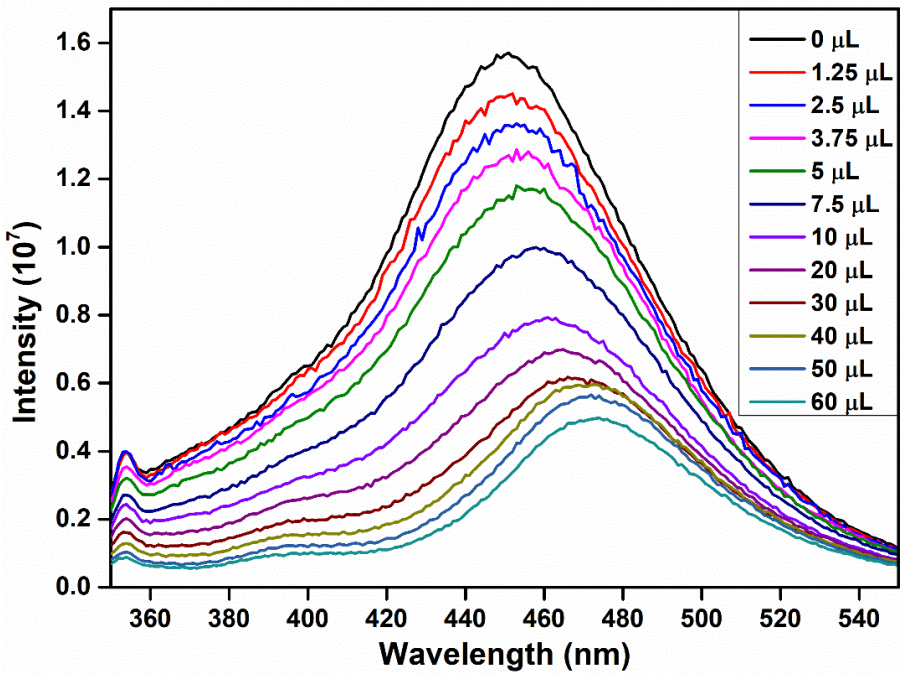

Fig. S52 Emission spectra of activated **1** dispersed in DMF upon incremental addition of Dunnite solution (1 mM).

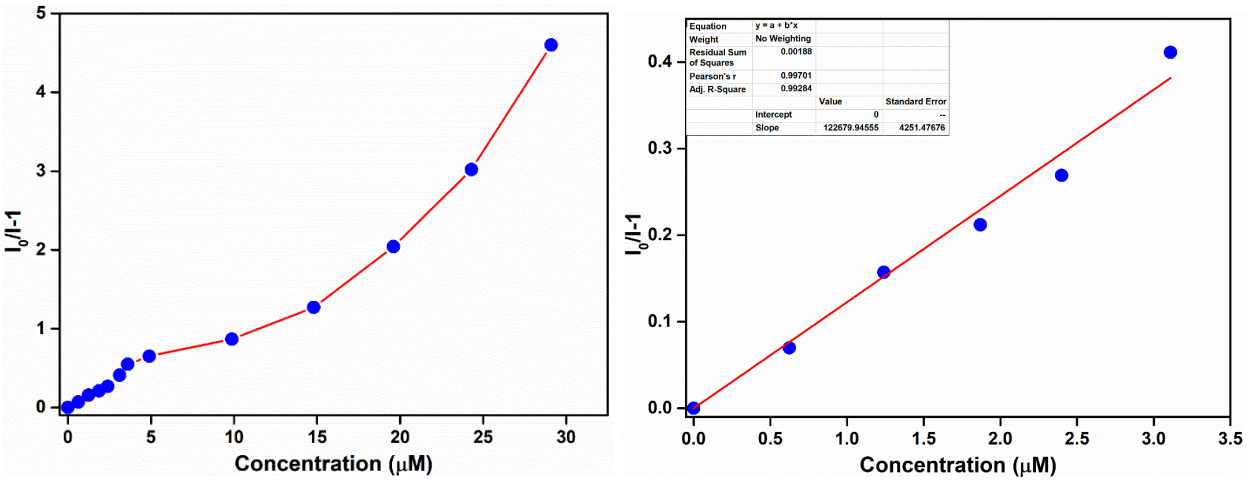

Fig. S53 Stern-Volmer plot for Dunnite in EtOH. The relative fluorescence intensity is linear with Dunnite in the lower concentration range, $I_0/I = 1 + 1.226 \times 10^5$ [Dunnite] ($R^2 = 0.992$).

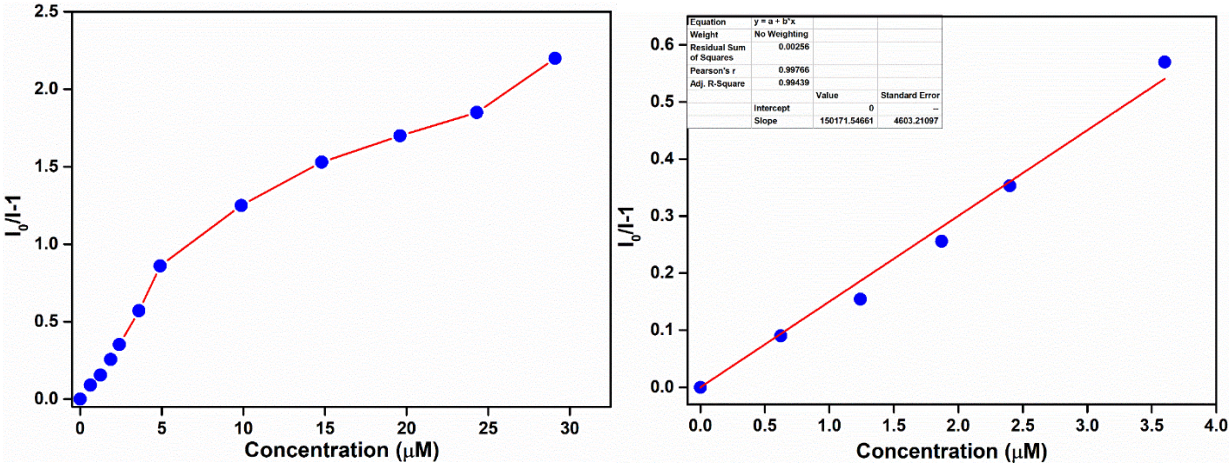

Fig. S54 Stern-Volmer plot for Dunnite in DMF. The relative fluorescence intensity is linear with Dunnite in the lower concentration range, $I_0/I = 1 + 1.5 \times 10^5$ [Dunnite] ($R^2 = 0.994$).

Section 12: Calculation of detection limit for Dunnite in water

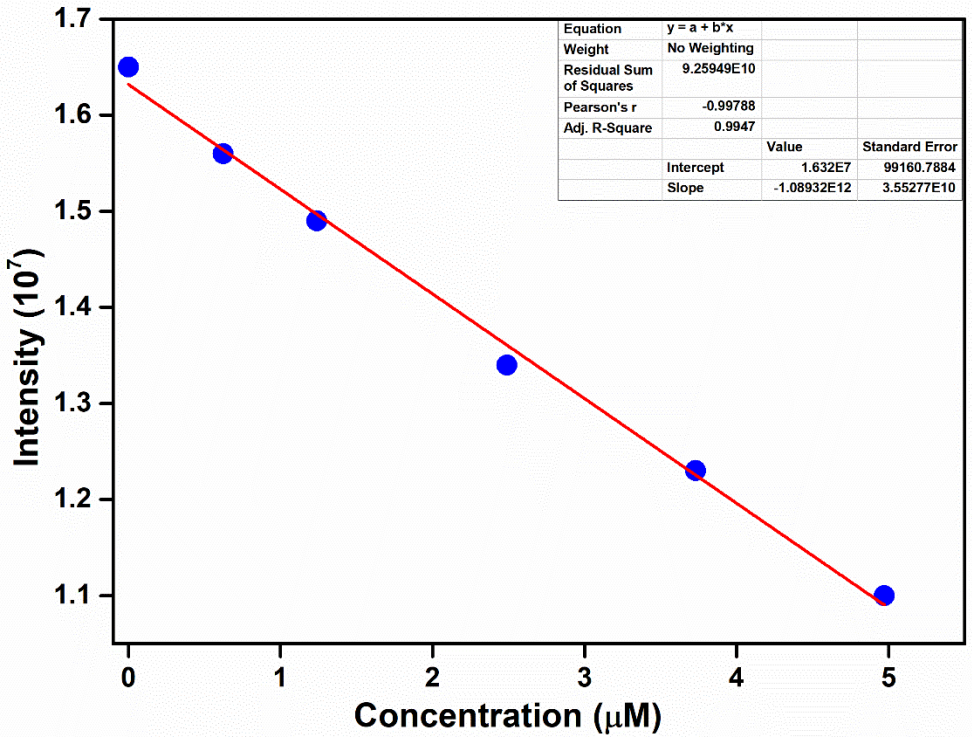

Fig. S55 Linear region of fluorescence intensity of activated **1** upon incremental addition of Dunnite (0 – 10 µL, 1 mM stock solution) at λ_{em} = 443 nm (upon λ_{ex} = 320 nm) (R^2 = 0.994).

Blank Readings	FL Intensity
Reading 1	2.20E+07
Reading 2	2.21E+07
Reading 3	2.24E+07
Reading 4	2.25E+07
Reading 5	2.27E+07
Standard Deviation (σ)	2.88E+05

Slope from Graph (m)	1.089E+12 M^{-1}
Detection limit (3σ/m)	7.93 E-7 M (170 ppb)

Calculation of detection limit for TNP in water

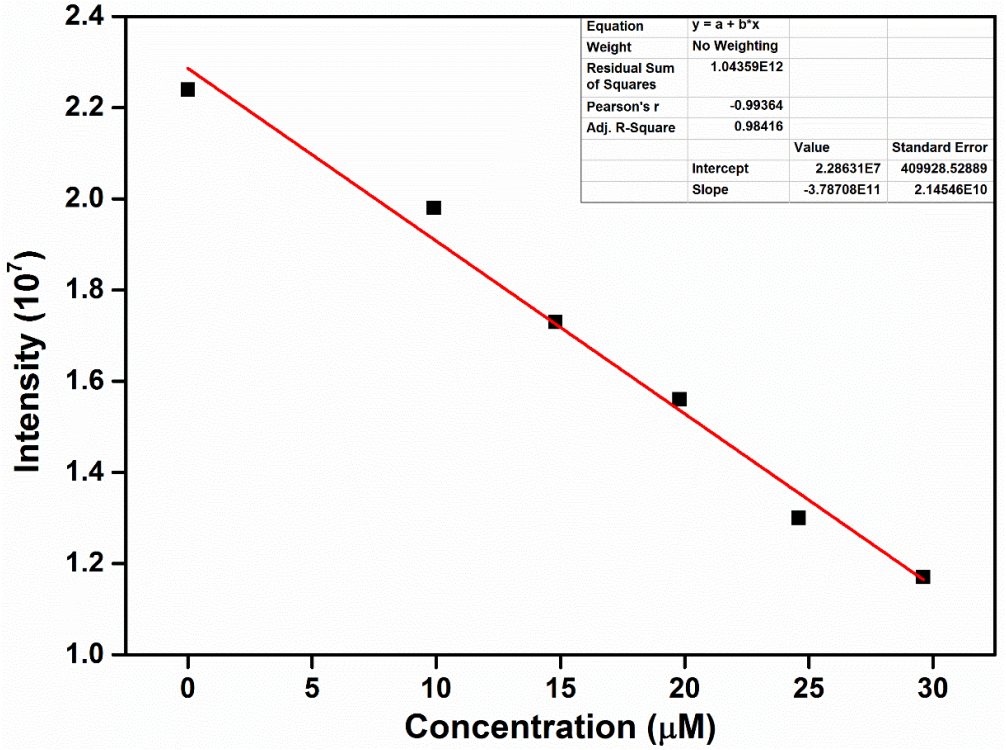

Fig. S56 Linear region of fluorescence intensity of activated **1** upon incremental addition of TNP (0 – 10 µL, 1 mM stock solution) at λ_{em} = 443 nm (upon λ_{ex} = 320 nm) (R^2 = 0.984).

Blank Readings	FL Intensity
Reading 1	2.20E+07
Reading 2	2.21E+07
Reading 3	2.24E+07
Reading 4	2.25E+07
Reading 5	2.27E+07
Standard Deviation (σ)	2.88E+05

Slope from Graph (m)	3.799E+11 M^{-1}
Detection limit (3σ/m)	2.279E-6 M (500 ppb)

Calculation of detection limit for AN in water

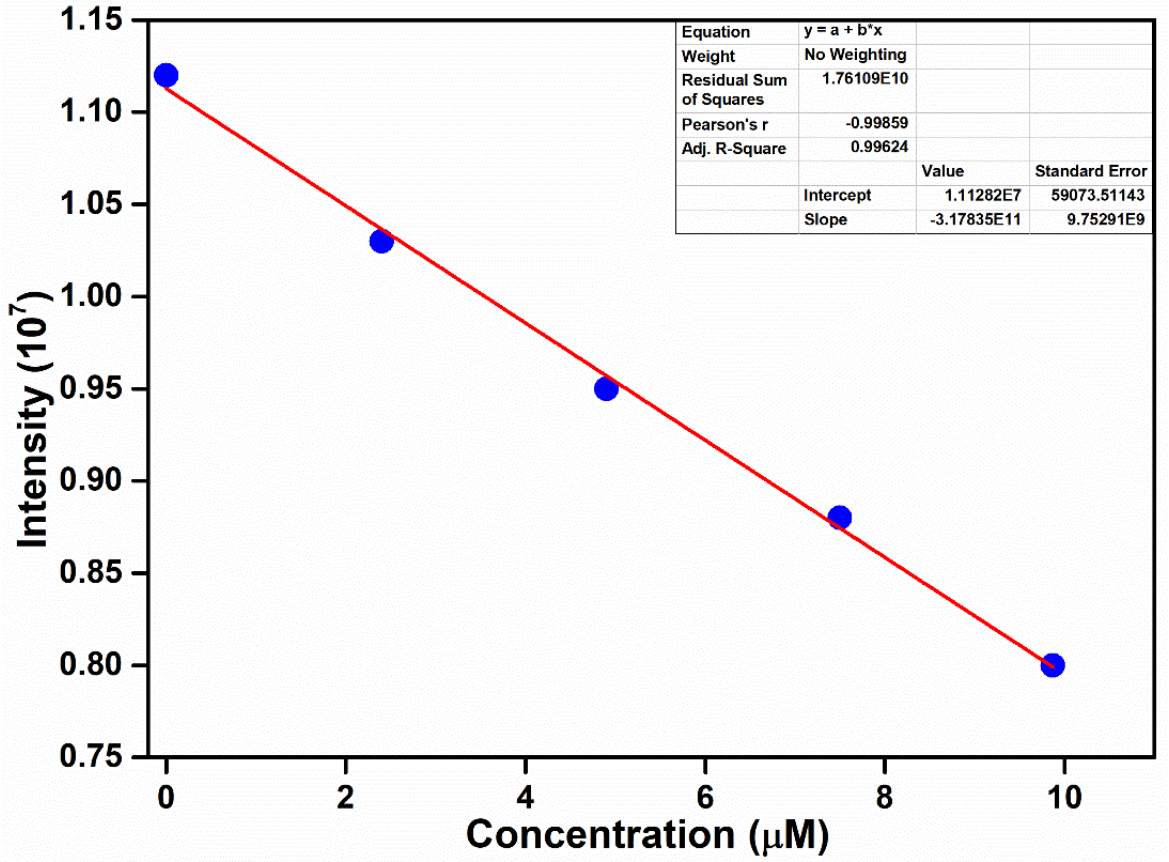

Fig. S57 Linear region of fluorescence intensity of activated **1** upon incremental addition of AN in water (R^2 = 0.991).

Detection limit: 2.18 ppm

Calculation of detection limit for Dunnite in EtOH

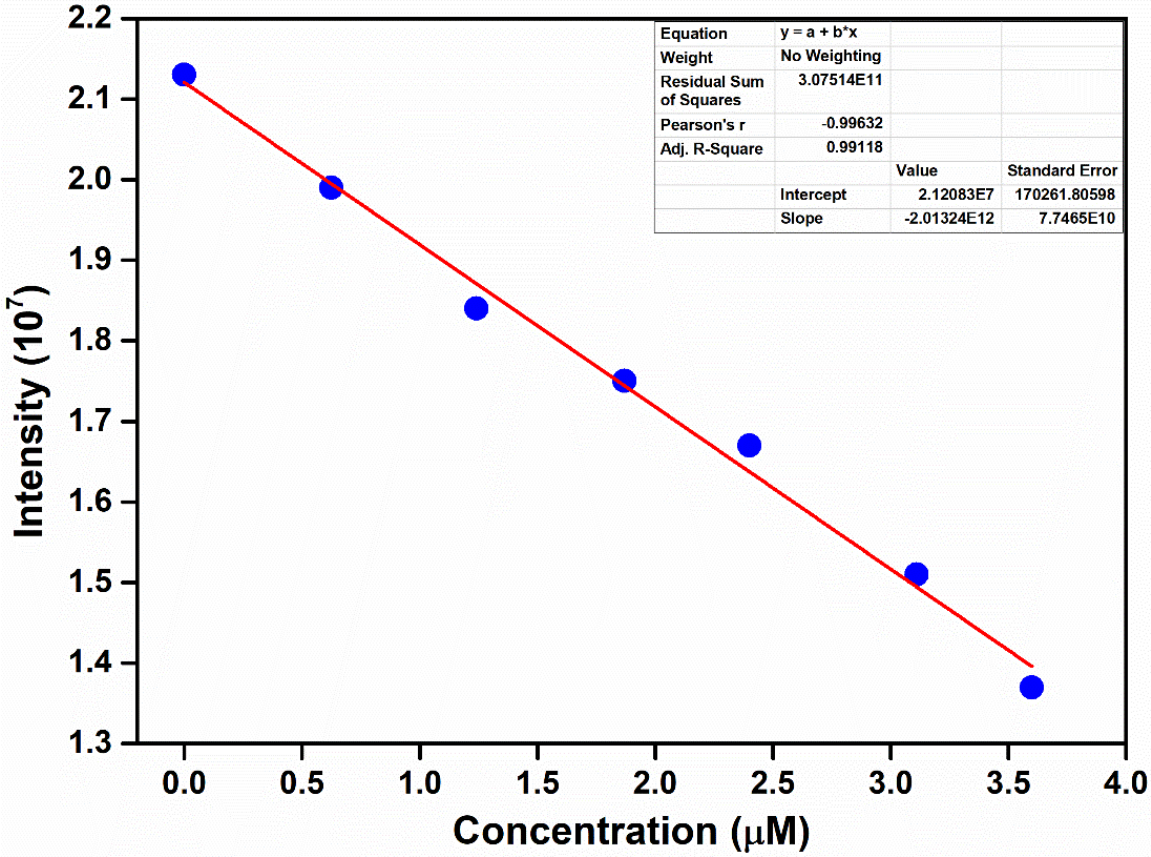

Fig. S58 Linear region of fluorescence intensity of activated **1** upon incremental addition of Dunnite in EtOH ($R^2 = 0.991$).

Detection limit: 103 ppb

Calculation of detection limit for Dunnite in DMF

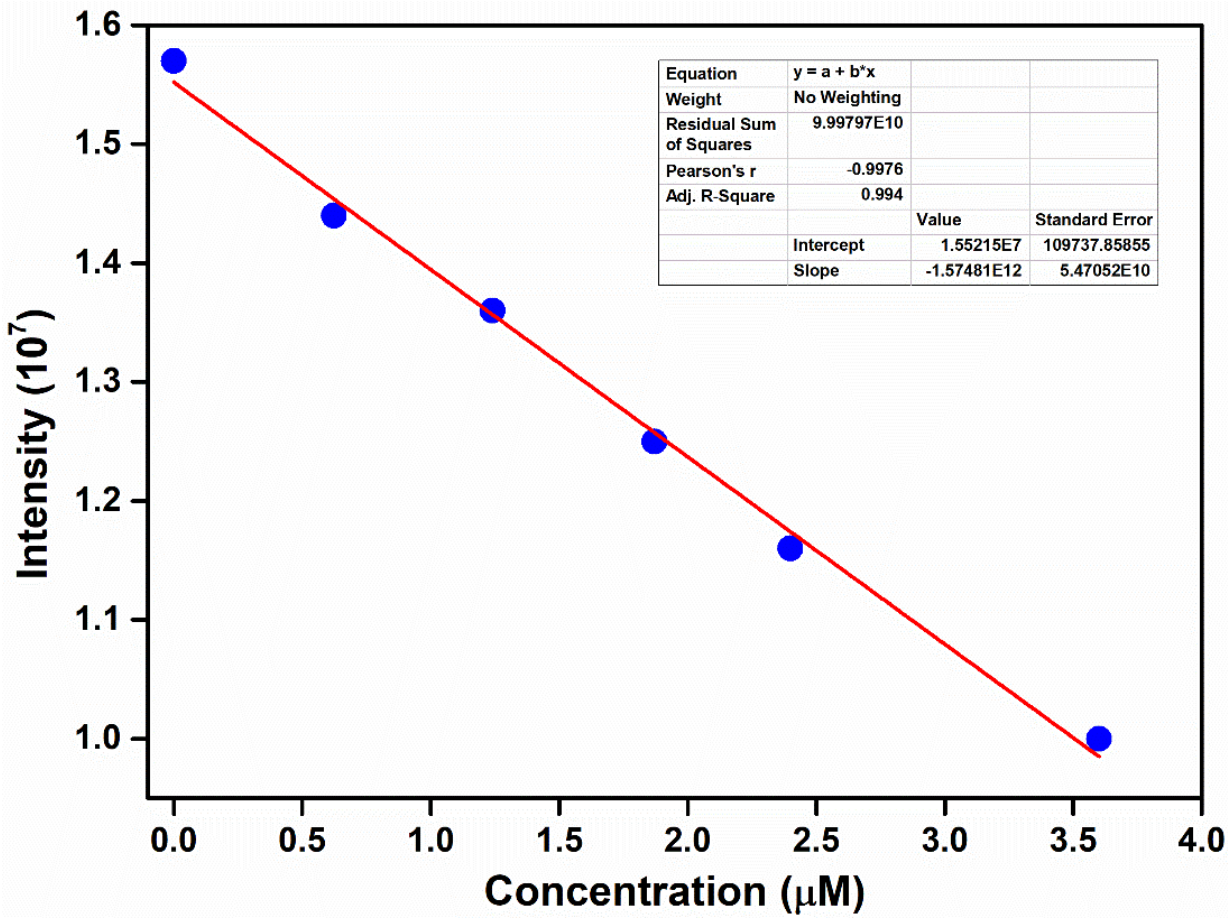

Fig. S59 Linear region of fluorescence intensity of activated **1** upon incremental addition of Dunnite in DMF (R^2 = 0.991).

Detection Limit: 132 ppb

Section 13: Spectral overlap and lifetime measurement of activated 1 in presence of NEs

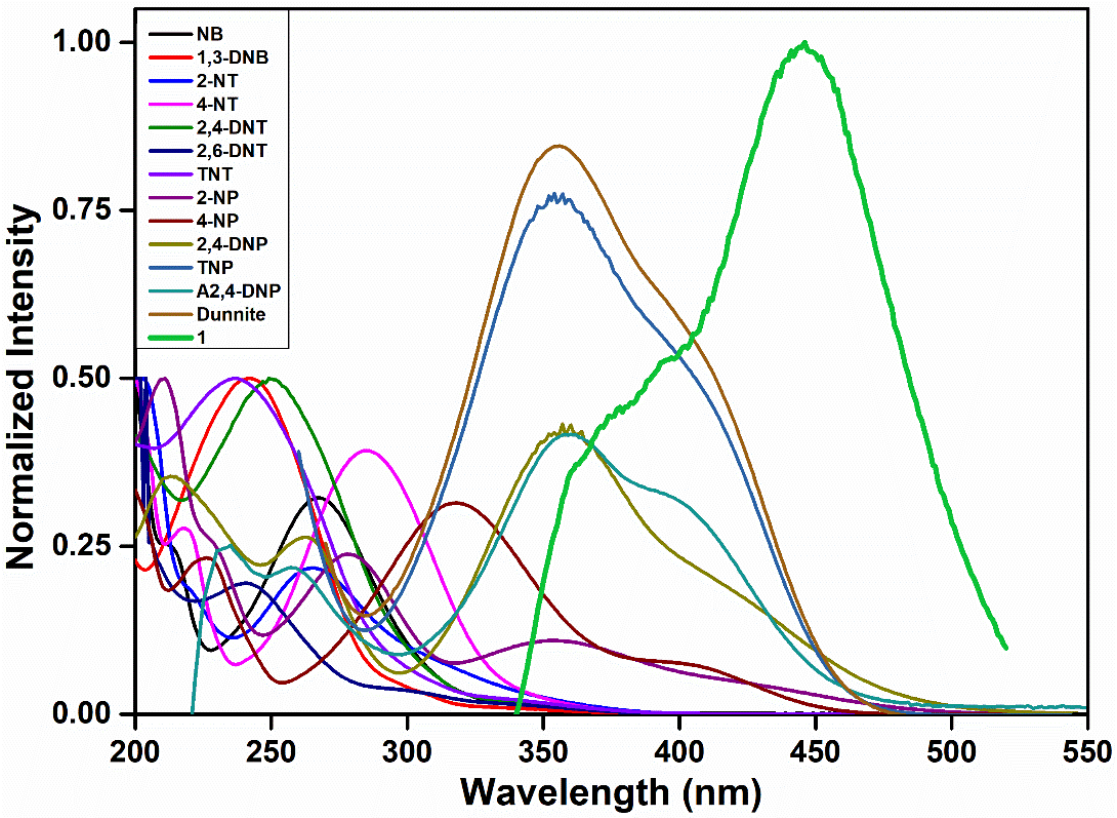

Fig. S60 Spectral overlap of absorption spectra of different nitro-analytes and emission spectrum of activated **1**.

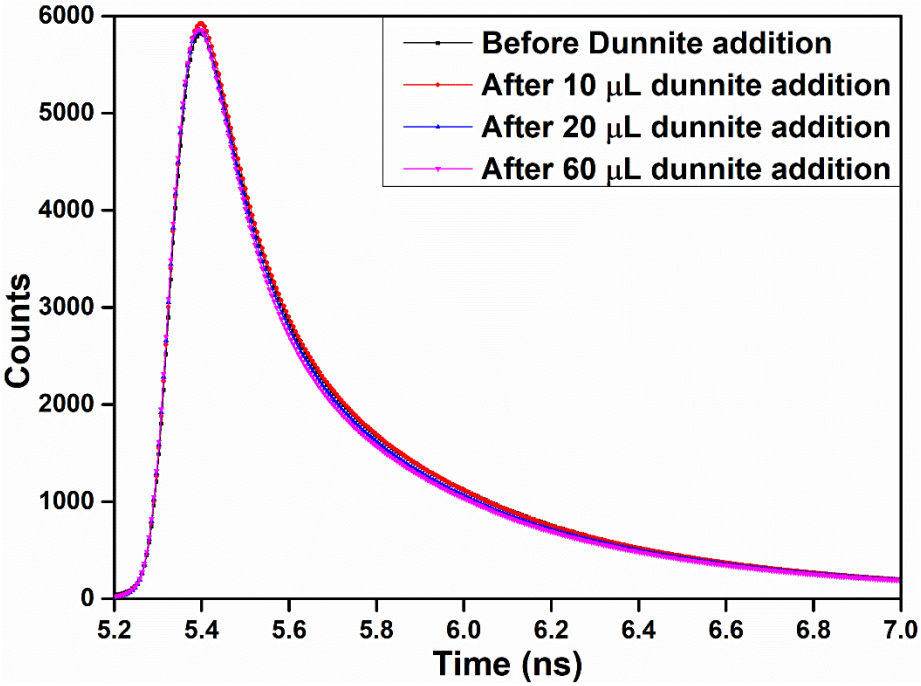

Fig. S61 Lifetime decay profiles of activated **1** before and after addition of Dunnite.

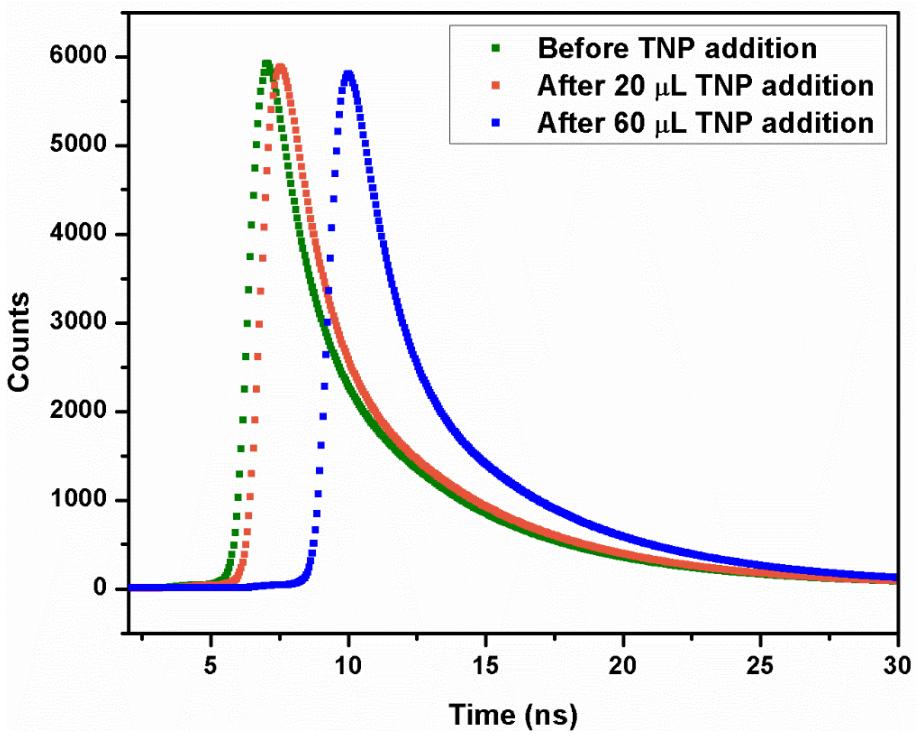

Fig. S62 Lifetime decay profiles of activated **1** before and after addition of TNP.

Section 14: DFT calculation

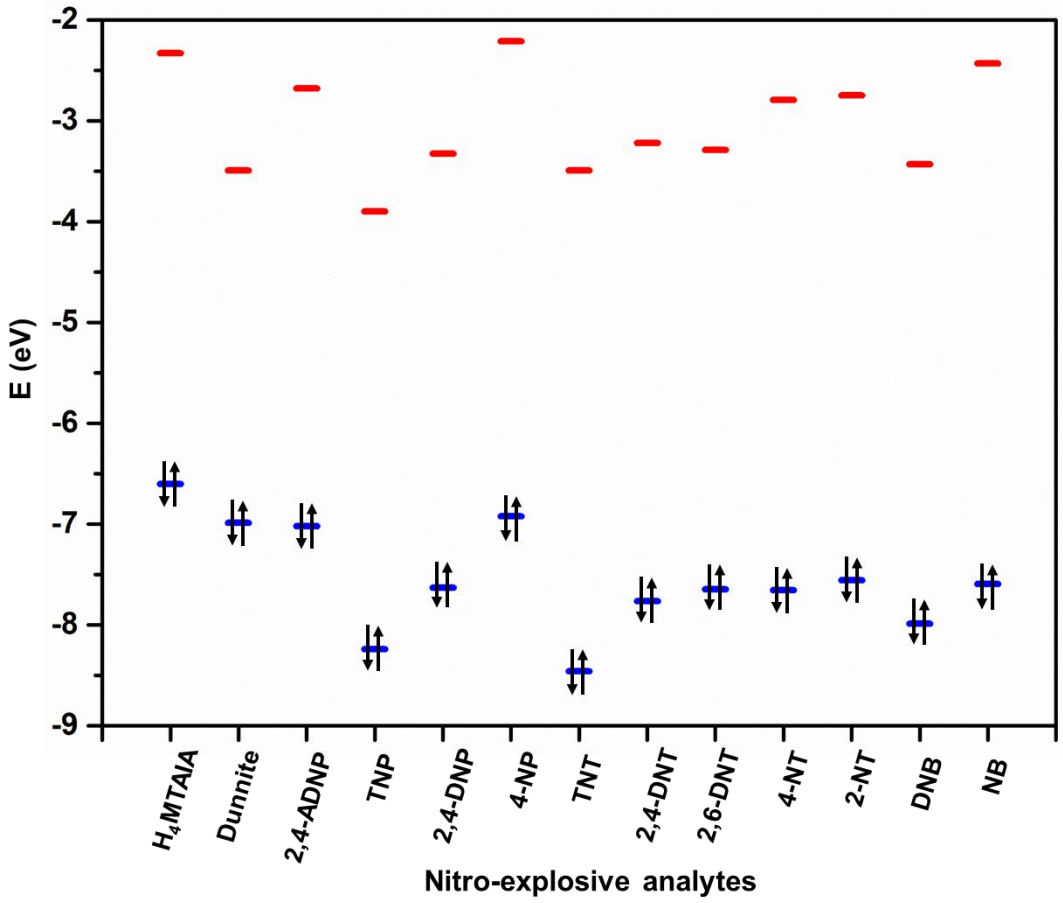

Fig. S63 HOMO-LUMO energy gaps of H_4MTAIA and different nitro-explosives.

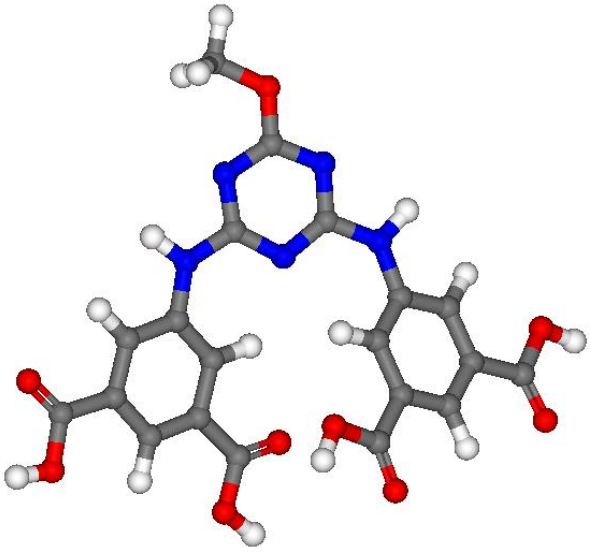

Fig. S64 Optimized structure of H_4MTAIA.

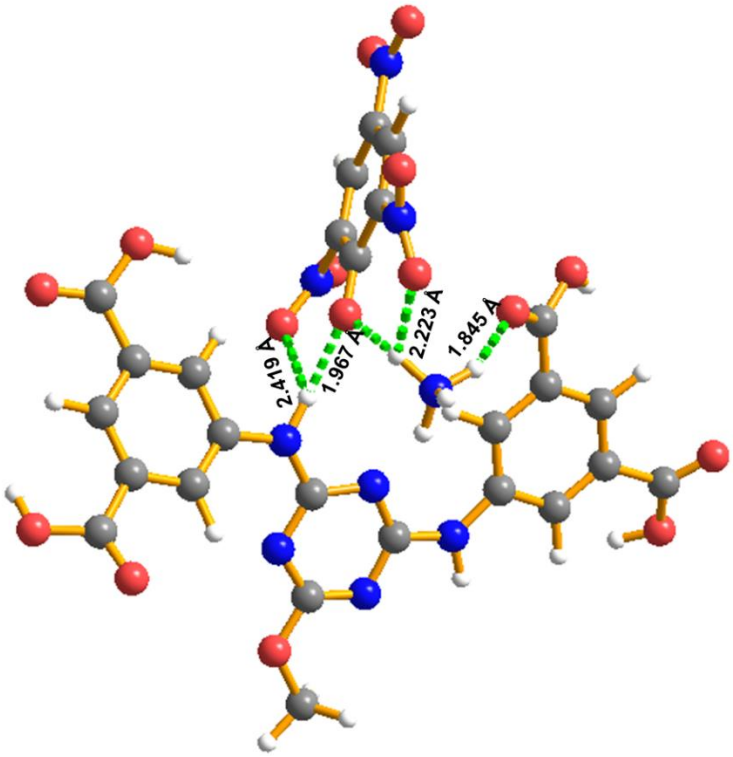

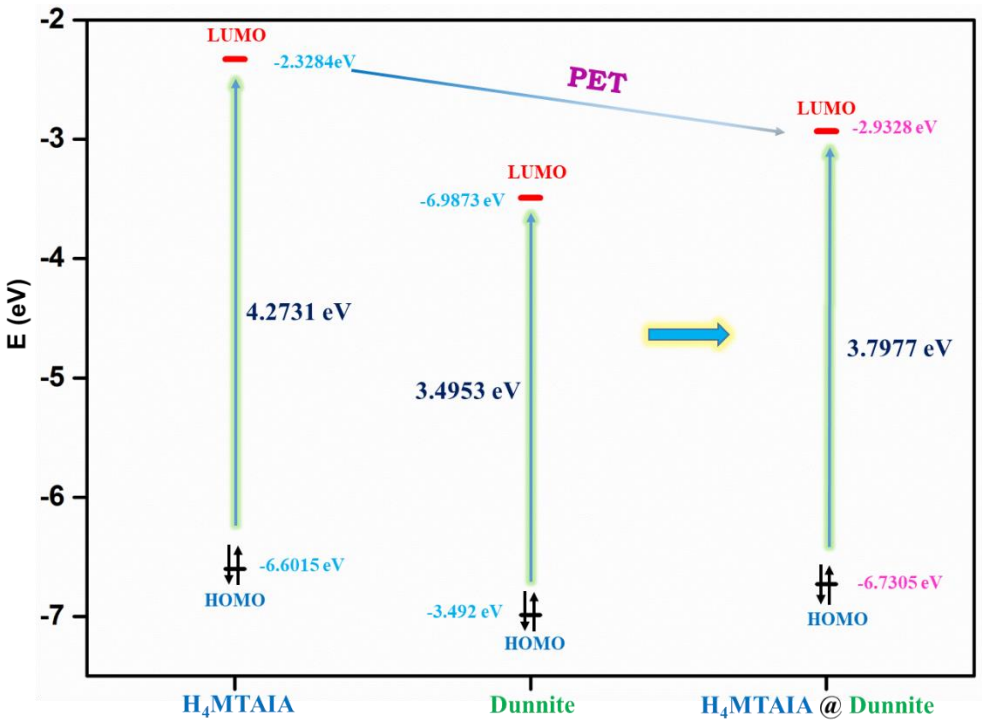

Fig. S65 Optimized structure of H_4MTAIA@Dunnite (top). HOMO-LUMO energy gaps of H_4MTAIA, Dunnite and H_4MATAIA@Dunnite (bottom).

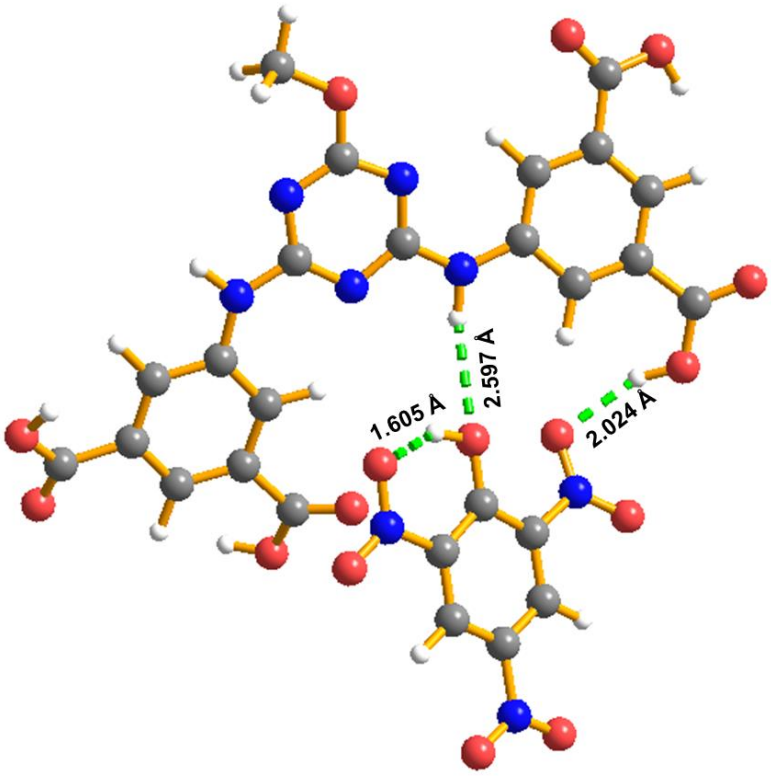

Fig. S66 Optimized structure of H_4MTAIA@TNP.

Section 15: CNA test by activated 1

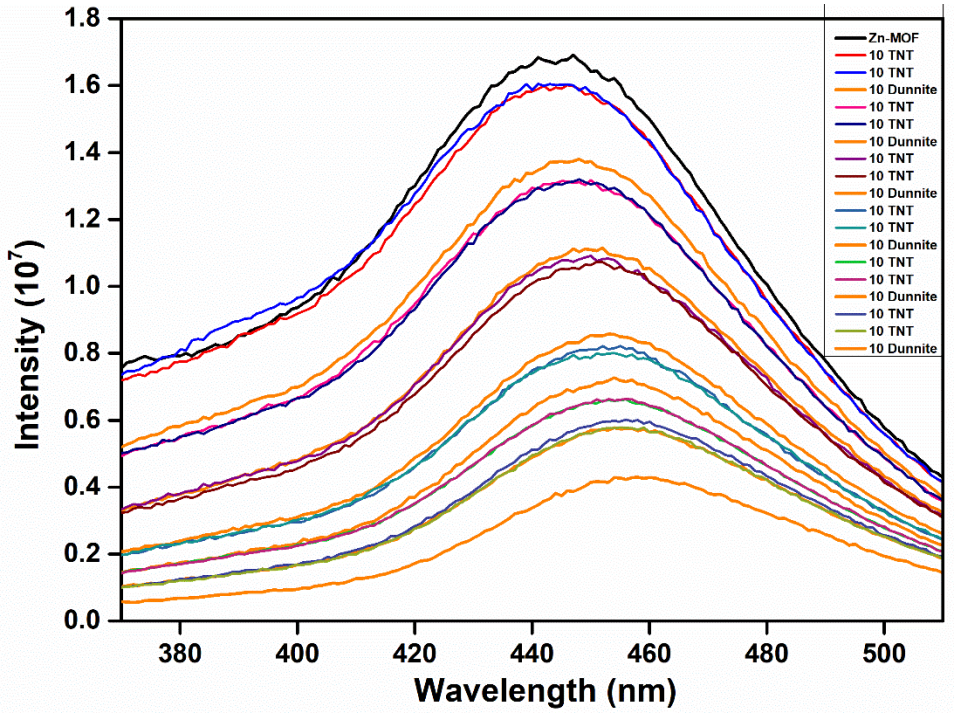

Fig. S67 Emission spectra of activated **1** upon addition of aqueous solution of TNT followed by Dunnite.

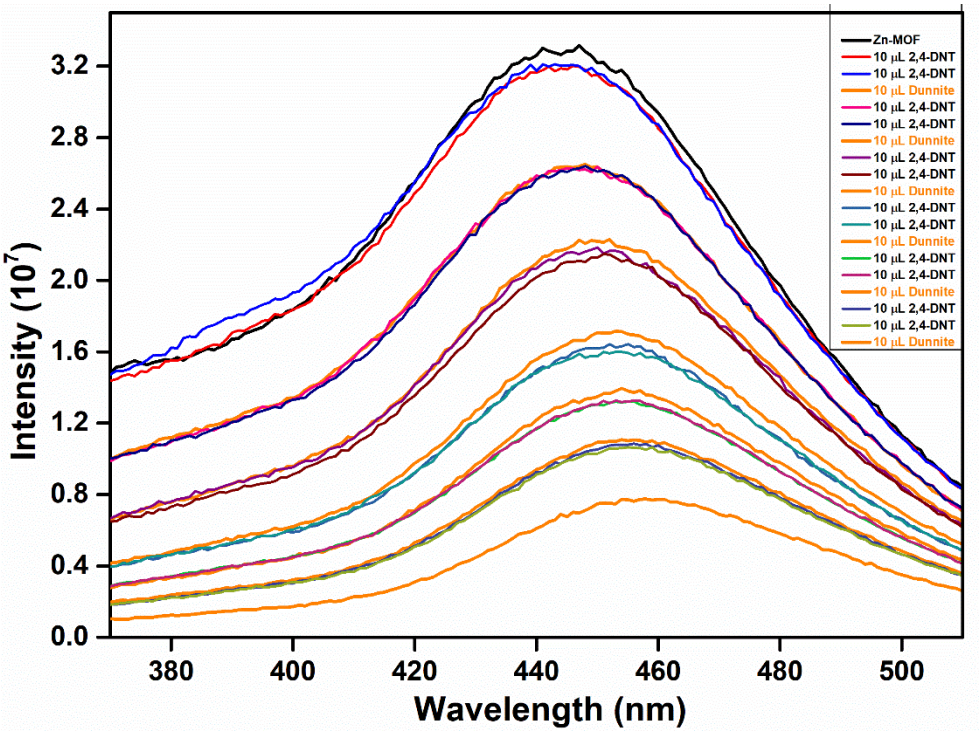

Fig. S68 Emission spectra of activated **1** upon addition of aqueous solution of 2,4-DNT followed by Dunnite.

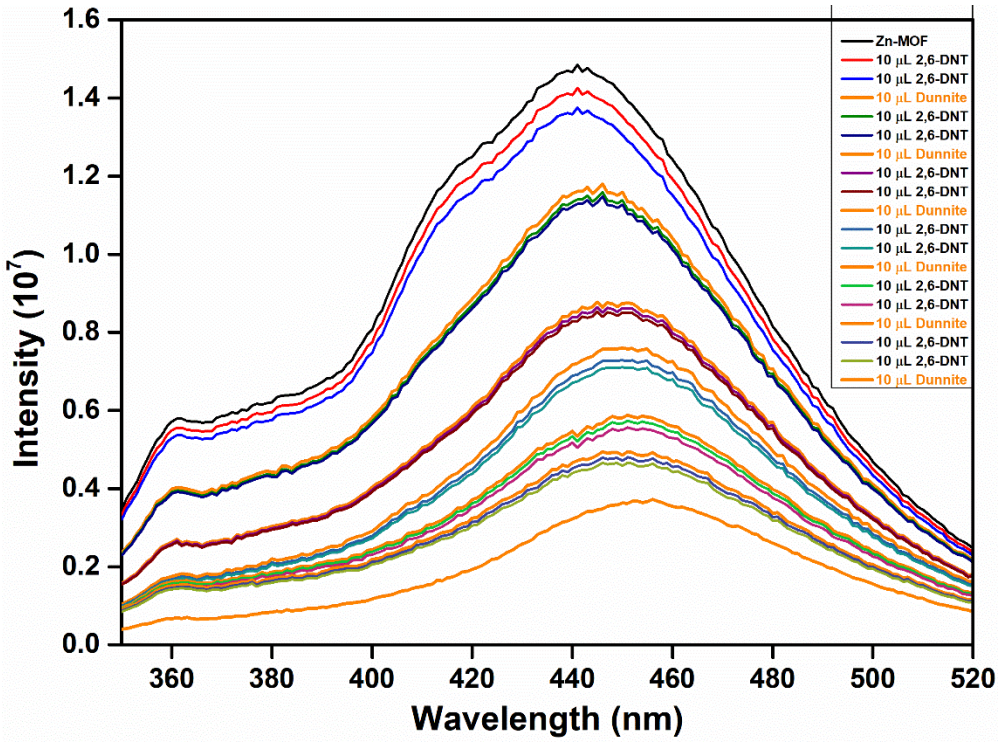

Fig. S69 Emission spectra of activated **1** upon addition of aqueous solution of 2,6-DNT followed by Dunnite.

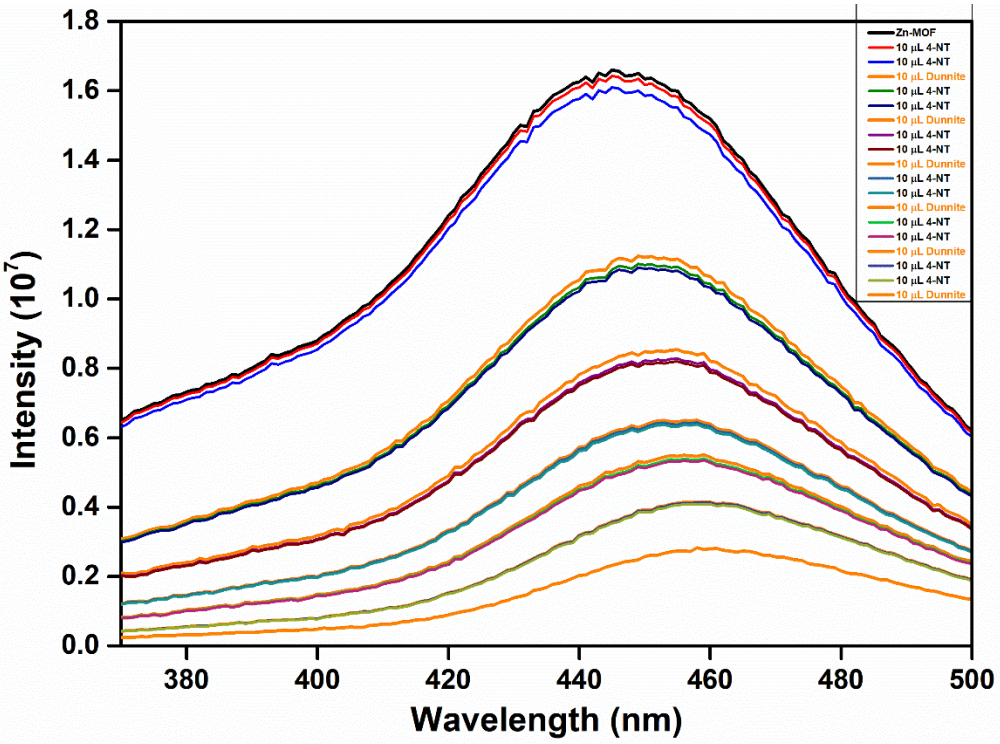

Fig. S70 Emission spectra of activated **1** upon addition of aqueous solution of 4-NT followed by Dunnite.

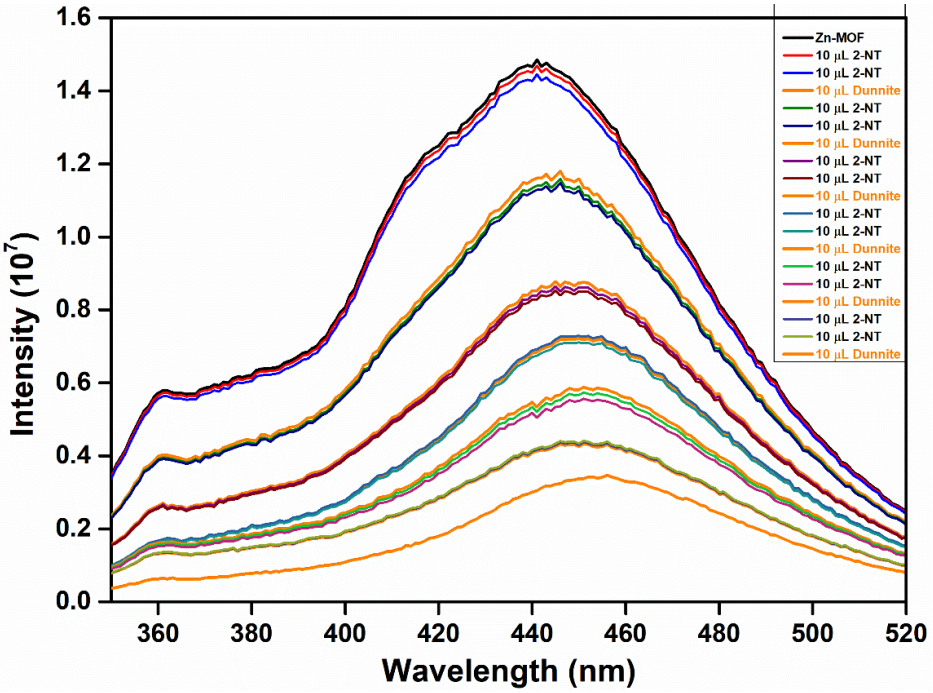

Fig. S71 Emission spectra of activated **1** upon addition of aqueous solution of 2-NT followed by Dunnite.

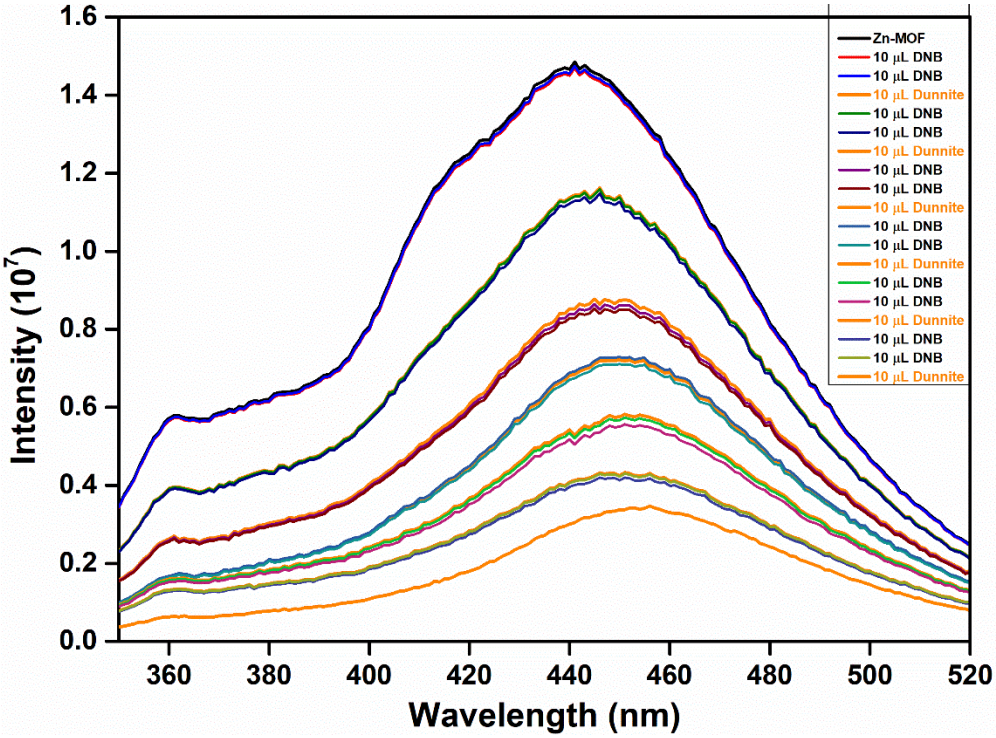

Fig. S72 Emission spectra of activated **1** upon addition of aqueous solution of DNB followed by Dunnite.

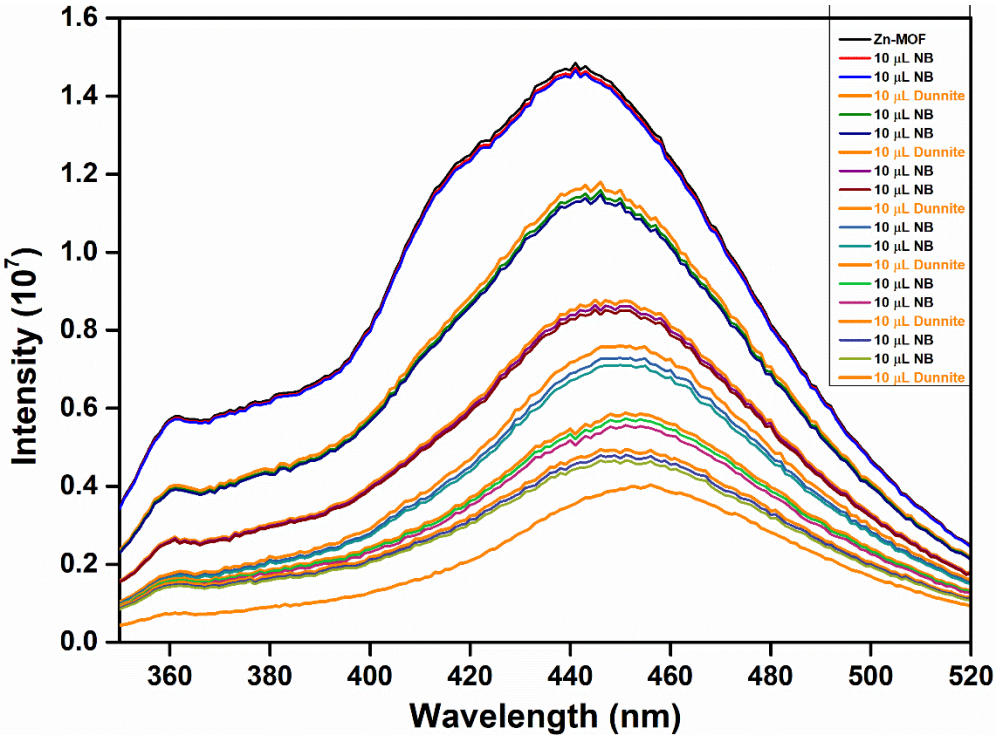

Fig. S73 Emission spectrum of activated **1** upon addition of aqueous solution of NB followed by Dunnite.

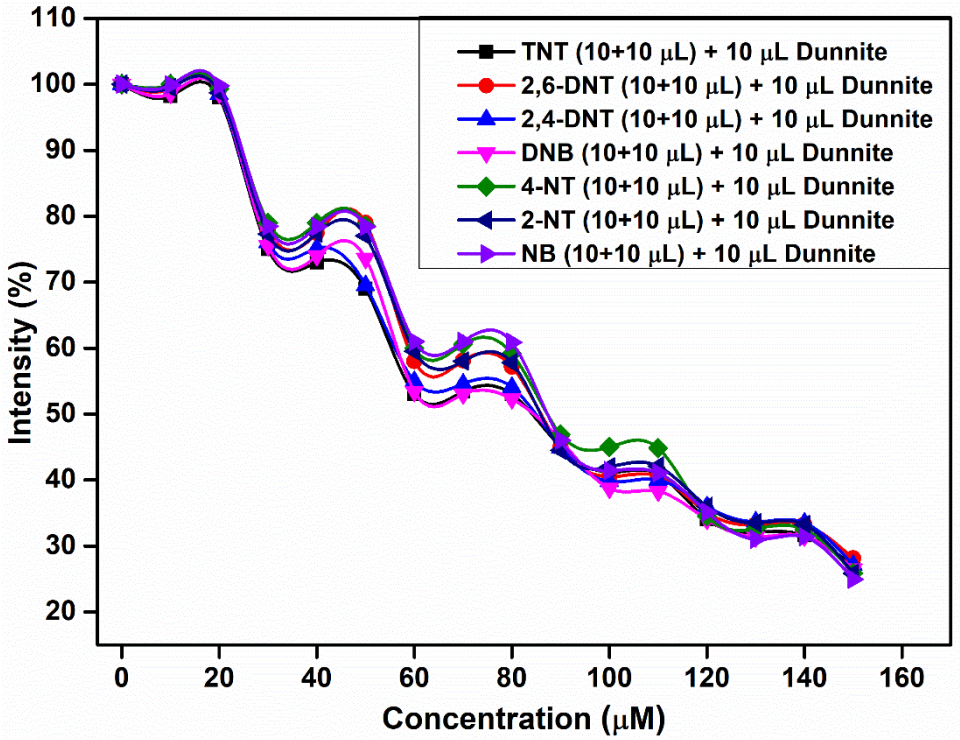

Fig. S74 Decrease in percentage of fluorescence intensity upon the addition of aqueous solutions of different nitro-analytes followed by Dunnite.

Section 16: Recyclability and retention of crystallinity of activated 1.

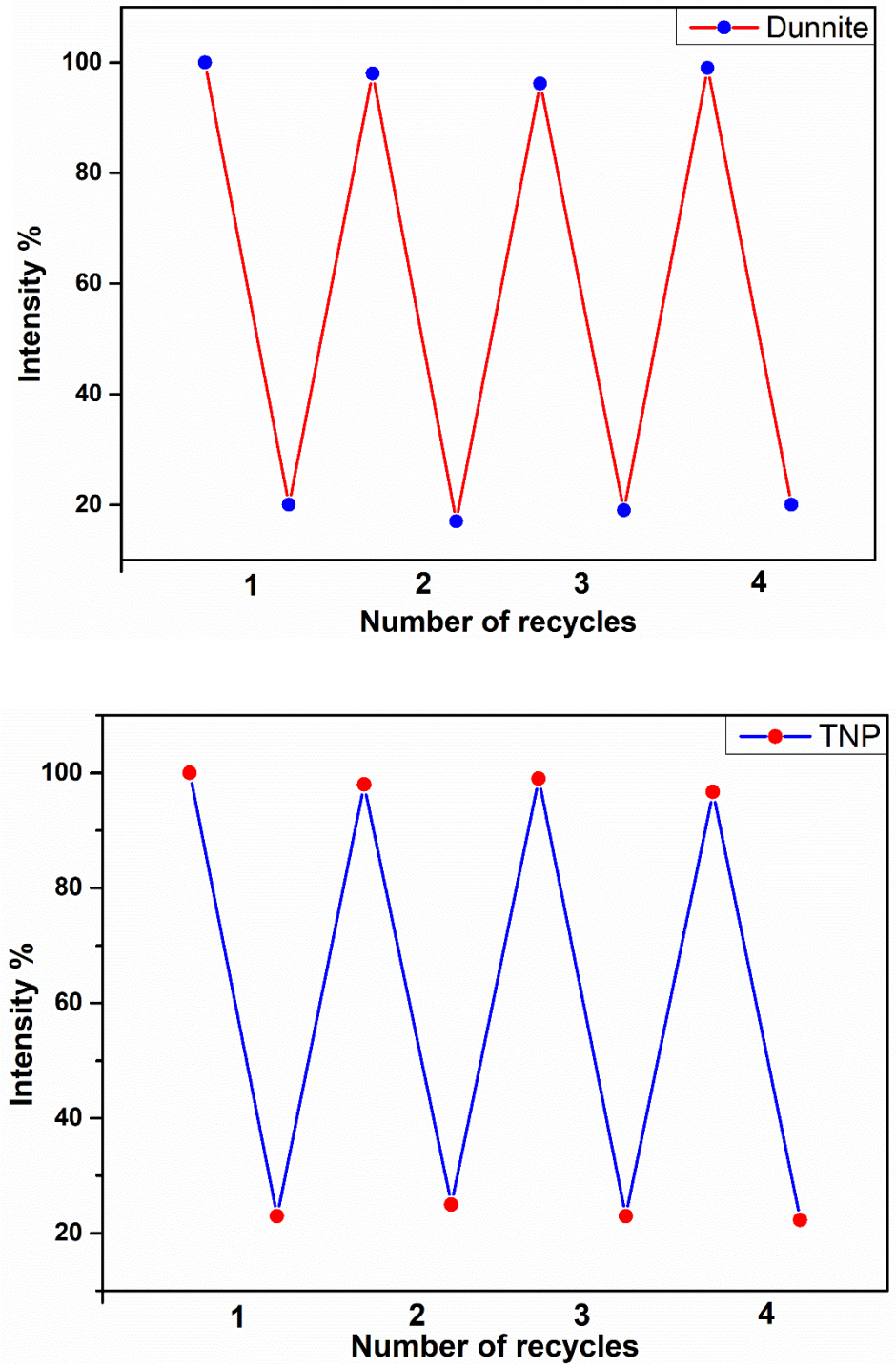

Fig. S75 Quenching and recyclability test for activated **1** after Dunnite (top) and TNP (bottom) addition for four cycles.

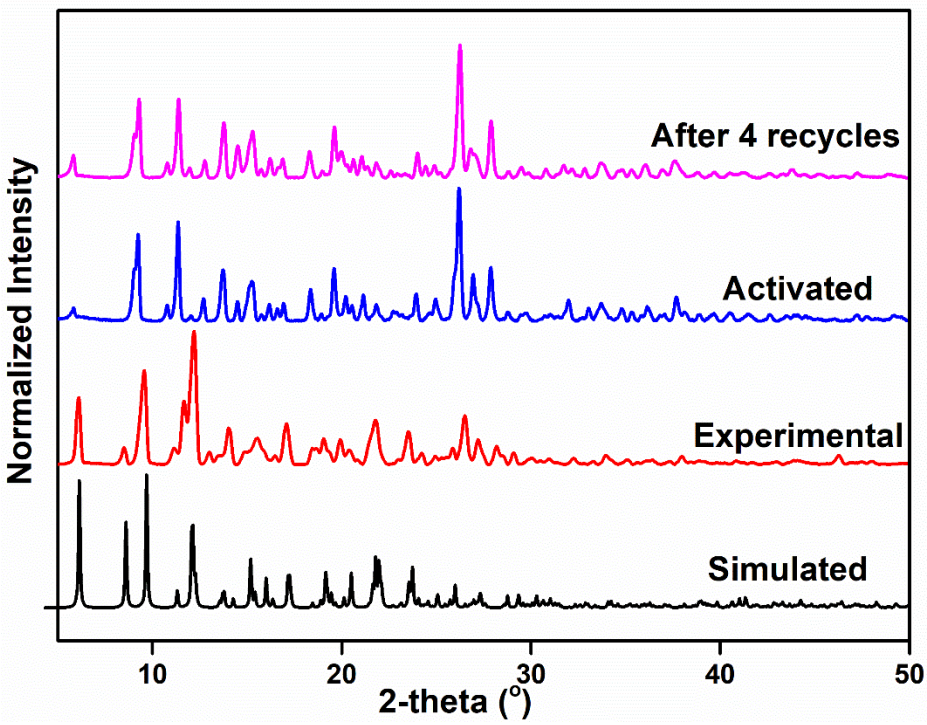

Fig. S76 PXRD profiles of activated **1** before and after sensing for four recycles.

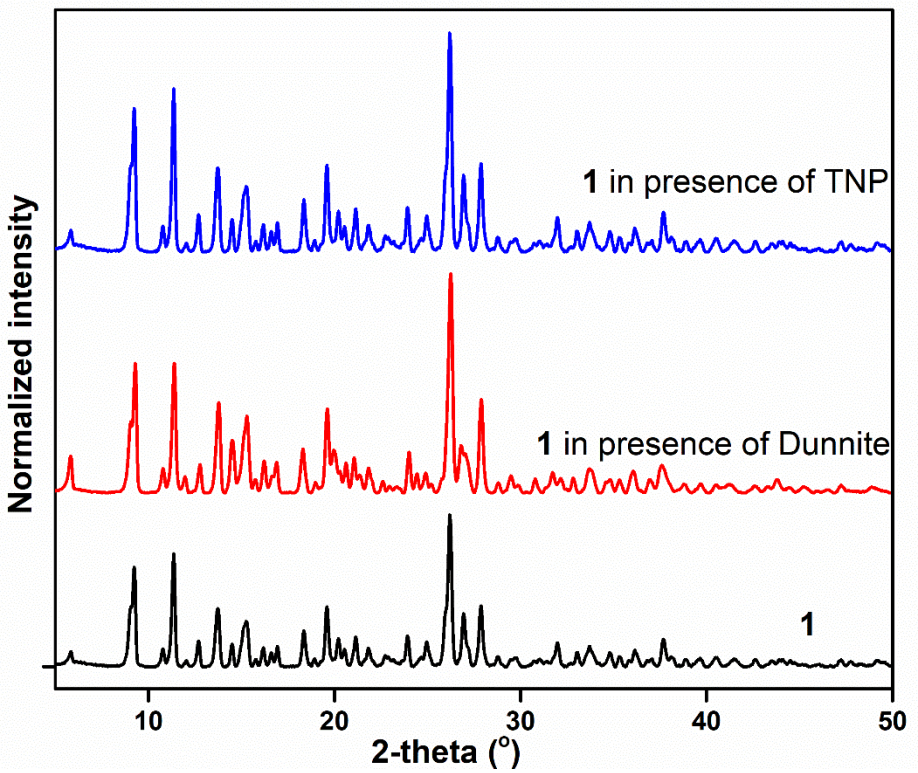

Fig. S77 PXRD patterns in presence of Dunnite and TNP.

Sensing of Dunnite and TNP in solid phase (contact mode)

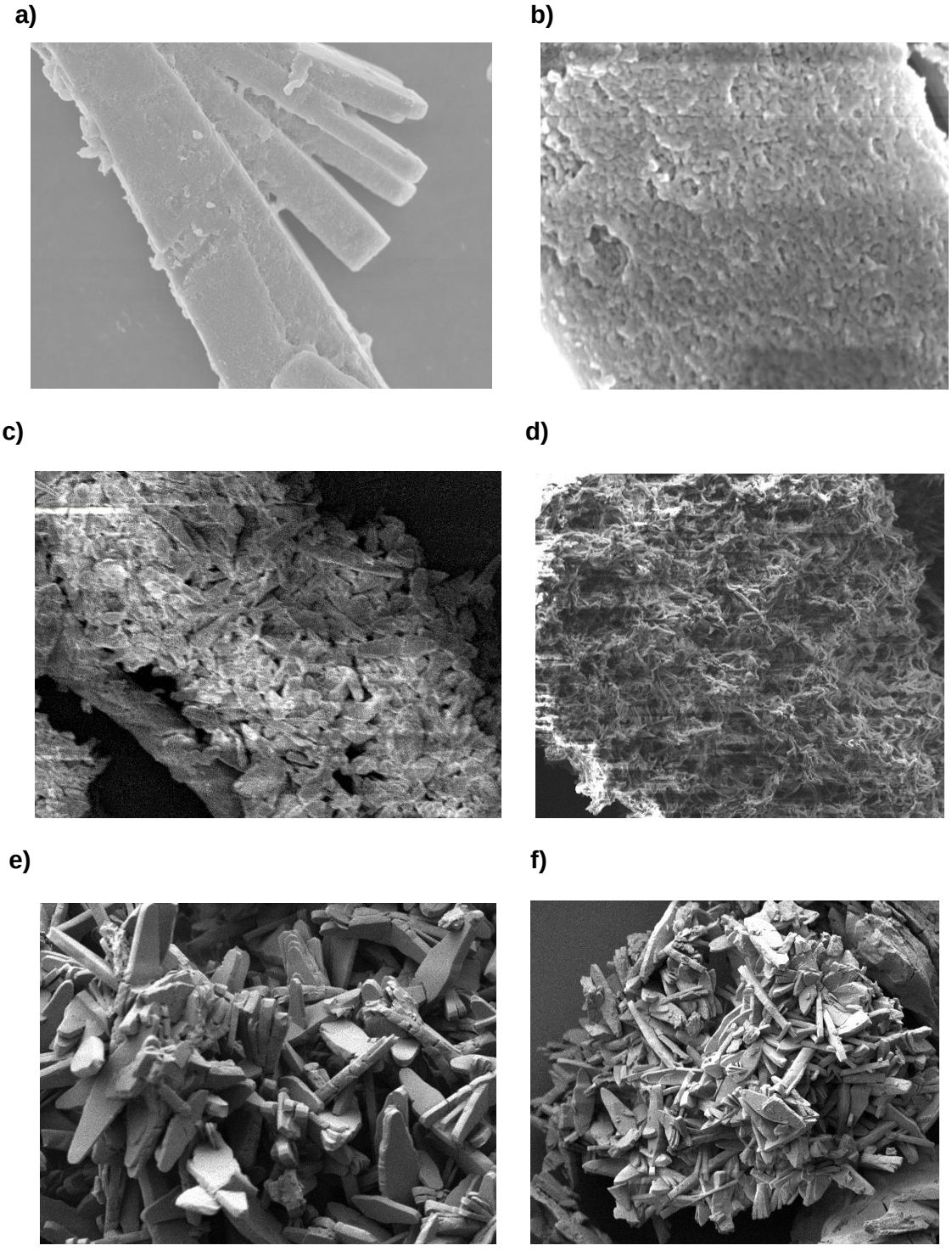

Fig. 78 FESEM images: (a, b) Morphology of **1**. (c, d) in presence of Dunnite and TNP and (e, f) after 4 recycles of Dunnite and TNP, respectively.

Table S1. HOMO and LUMO energies for H_4MTAIA and different solvents using B3LYP/(6-31G)+d,p level.

Compound	HOMO (eV)	LUMO (eV)	Band Gap (eV)
H_4MTAIA	-7.184	-2.898	-4.286
MeOH	-7.6839	-3.4920	-7.69451
EtOH	-7.5805	-3.8978	-7.57234
H_2O	-8.735	-3.4926	-9.4207
IPA	-11.8383	-3.2174	-9.6957
DMF	-6.8436	-2.7924	-6.71353
DMA	-6.6924	-2.7467	-6.59118
DMSO	-8.1923	-3.2877	-7.8024
CHCl3	-8.7435	-3.4311	-7.1185
CH3CN	-9.176	-2.4283	-8.8999
Acetone	-7.015	-3.326	-6.1361
THF	-6.7636	-2.210	-6.9742
Dioxane	-6.759	-2.6759	-7.0684

Table S2. Summary of Stern-Volmer and quenching rate constants (K_{sv} and K_q) of **1** for different nitro-explosives at room temperature.

Nitro-Explosives	S-V Constant (K_{SV}, M^{-1})	Quenching Rate Constant (K_q, $M^{-1}s^{-1}$)
Dunnite	9.44×10^4	1.35×10^{13}
TNP	7.77×10^4	1.10×10^{13}
TNT	1.47×10^4	2.10×10^{12}
2,4-DNT	1.29×10^4	1.84×10^{12}
2,6-DNT	6.11×10^3	8.72×10^{11}
4-NT	1.06×10^4	1.51×10^{12}
2-NT	3.67×10^3	5.24×10^{11}
DNB	9.98×10^3	1.42×10^{12}
NB	7.79×10^3	1.11×10^{12}
2,4-DNP	1.65×10^4	2.35×10^{12}
4-NP	1.03×10^4	1.46×10^{12}
2-NP	7.049×10^3	1.00×10^{12}
2,4-ADNP	1.96×10^4	2.80×10^{12}

Table S3. Detection of TNP by metal-organic frameworks.

MOF	K_{sv}	LOD	Medium	Reference
Zn-MOF (1)	**$7.77 \times 10^4\ M^{-1}$**	**9.4×10^{-10} M (0.5 ppm)**	**Water**	**This work**
$[Zn_2(L)_2(dpyb)]_n$ (MOF-1) and $\{[Zn(L)(dipb)]\cdot 2H_2O\}_n$ (MOF-2)	2.40×10^4 and $2.46 \times 10^4\ M^{-1}$	NA	DMA	*Chem. Commun.*, 2015, **51**, 8300.
$\{[La(TPT)(DMSO)_2]\cdot H_2O\}_n$ (La-MOF (1))	$9.89 \times 10^4\ M^{-1}$	NA	EtOH	*Dalton Trans*., 2015, **44**, 13340–13346.
$\{[Cd_3(TPT)_2(DMF)_2]\cdot 0.5H_2O\}_n$	$6.56 \times 10^4\ M^{-1}$	NA	EtOH	*Dalton Trans*., 2015, **44**, 230–236.
$[Tb(1,3,5\text{-}BTC)]_n$	$3.4 \times 10^4\ M^{-1}$	8.1×10^{-8} M	EtOH	*J. Mater. Chem. A*, 2013, **1**, 8745–8752
$\{Zr_6O_4(OH)_4(L)_6\}_n$	$2.9 \times 10^4\ M^{-1}$	2.6 μM	Water	*Chem. Commun.*, 2014, **50**, 8915-8918.
$[Zn_4(DMF)(Ur)_2(2,6\text{-}NDC)_4]_n$	$10.83 \times 10^4\ M^{-1}$	NA 1.63 ppm	Water	*Cryst. Growth Des*. **2015**, *15*, 4627−4634.
$[Zr_6O_4(OH)_6(L)_6]_n$	$5.8 \times 10^4\ M^{-1}$	NA 0.4 ppm	Water	*Dalton Trans*., 2015, **44**, 15175–15180.
$[Cd(NDC)_{0.5}(PCA)]_n$	$3.5 \times 10^4\ M^{-1}$	NA	MeCN	*Angew. Chem. Int. Ed*., 2013, **52**, 2881 – 2885.
$[Zn(NDC)H_2O)]_n$ and $[Cd(NDC)(H_2O)]_n$	$6 \times 10^4\ M^{-1}$ and $2.385 \times 10^4\ M^{-1}$	1×10^{-6} M (0.23 ppm) and 4×10^{-6} M (0.92 ppm)	Water	*Eur. J. Inorg. Chem.*, 2015, 2851–2857.
$\{[Zn_8(ad)_4(BPDC)_6 0.2Me_2NH_2]\cdot G\}_n$	$4.6 \times 10^4\ M^{-1}$	12.9μM	Water	*Chem. Eur. J.* **2015**, *21*, 965.
$\{[Zn_2(NDC)_2(bpy)]\cdot Gx\}_n$	$0.4 \times 10^4\ M^{-1}$	NA	EtOH	*J. Mater. Chem. C*, 2014, **2**, 10073.
$\{[Cd_4(L)_2(L_2)_3(H_2O)_2]\cdot 8DMF\cdot 8H_2O\}_n$	$3.84 \times 10^4\ M^{-1}$	NA 1.98 ppm	EtOH	*Inorg. Chem*., 2016, **55**, 1741−1747.
$\{[Zn(C_{34}H_{18}O_8)_{0.5}(C_{20}N_2H_{16})_{0.5}]\cdot 0.5(C_{20}N_2H_{16})\}_n$	$8.1 \times 10^4\ M^{-1}$	NA	DMF	*Chem. Commun.*, 2015, **51**, 6576-6579.
$\{[Cd_5Cl_6(L)(HL)_2]\cdot 7H_2O\}_n$	$4.05 \times 10^4\ M^{-1}$	1.87×10^{-7} M (42.84 ppb)	EtOH	*Cryst. Growth Des.*, 2016, **16**, 842−851.
BUT-12 and BUT-13	$3.1 \times 10^5\ M^{-1}$ and $5.1 \times 10^5\ M^{-1}$	23 ppb and 10 ppb	Water	*J. Am. Chem. Soc.*, 2016, **138**, 6204−6216.

Table S4. Average lifetime calculated for **1** before and after incremental addition of Dunnite and χ^2 value.

	1	**1** + 10 μL TNP	**1** + 20 μL TNP	**1** + 60 μL TNP
α_1	0.67	0.68	0.68	0.67
τ_1	4.9	4.95	4.97	4.97
α_2	0.11	0.22	0.22	0.12
τ_2	12.8	0.9	0.9	13.5
α_3	0.22	0.12	0.12	0.21
τ_3	0.9	12.75	12.8	1.1
Average Lifetime (τ_{avg}) (ns)	7.01	7.04	7.09	7.2
χ^2 value	1.06	1.06	1.1	1.12

Table S5. Average lifetime calculated for **1** before and after incremental addition of TNP and χ^2 value.

	1	**1** + 20 μL TNP	**1** + 60 μL TNP
α_1	0.67	0.25	0.27
τ_1	4.9	1.08	1.18
α_2	0.11	0.71	0.68
τ_2	12.8	5.6	5.8
α_3	0.22	0.04	0.04
τ_3	0.9	12.3	63.8
Average Lifetime (τ_{avg}) (ns)	7.01	7.51	10.01
χ^2 value	1.06	1.1	1.02

Table S6. HOMO and LUMO energies calculation for H_4MTAIA and NEs using B3LYP/(6-31G)d,p level.

Compound	HOMO (eV)	LUMO (eV)	Band Gap (eV)
H_4MTAIA	-6.6015	-2.3284	4.2731
Dunnite	-6.9873	-3.4920	3.4953
TNP	-8.2374	-3.8978	4.3396
TNT	-8.4592	-3.4926	4.9666
2,4-DNT	-7.7645	-3.2174	4.5471
4-NT	-7.6542	-2.7924	4.8619
2-NT	-7.5546	-2.7467	4.8079
2,6-DNT	-7.6448	-3.2877	4.3571
DNB	-7.9855	-3.4311	4.5544
NB	-7.5912	-2.4283	5.1629
2,4-DNP	-7.628	-3.326	4.302
4-NP	-6.921	-2.210	4.711
2,4-ADNP	-7.0213	-2.6759	4.345